Monthly Notices of the ROYAL ASTRONOMICAL SOCIETY

MNRAS **547,** 1–40 (2026) https://doi.org/10.1093/mnras/stag411
Advance Access publication 2026 February 27

Spectroscopic confirmation of dual and offset quasars from the *Subaru* HSC-SSP program

Shenli Tang [1]★ John Silverman [2,3,4,5] Xavier Prochaska [2,6] Manda Banerji [1] Xuheng Ding [7] Masafusa Onoue [8] and Knud Jahnke [9]

[1]*School of Physics & Astronomy, University of Southampton, Highfield Campus, Southampton SO17 1BJ, UK*
[2]*Kavli Institute for the Physics and Mathematics of the Universe (WPI), The University of Tokyo, Kashiwa, Chiba 277-8583, Japan*
[3]*Department of Astronomy, School of Science, The University of Tokyo, 7-3-1 Hongo, Bunkyo, Tokyo 113-0033, Japan*
[4]*Center for Data-Driven Discovery, Kavli IPMU (WPI), UTIAS, The University of Tokyo, Kashiwa, Chiba 277-8583, Japan*
[5]*Center for Astrophysical Sciences, Department of Physics & Astronomy, Johns Hopkins University, Baltimore, MD 21218, USA*
[6]*Department of Astronomy and Astrophysics, University of California, Santa Cruz, 1156 High Street, Santa Cruz, CA 95064, USA*
[7]*School of Physics and Technology, Wuhan University, Wuhan 430072, China*
[8]*Waseda Institute for Advanced Study (WIAS), Waseda University, 1-21-1, Nishi-Waseda, Shinjuku, Tokyo 169-0051, Japan*
[9]*Max-Planck-Institut für Astronomie, Königstuhl 17, D-69117 Heidelberg, Germany*

Accepted 2026 February 20. Received 2026 February 2; in original form 2025 December 8

ABSTRACT

We present a spectroscopic follow-up program targeting closely separated dual quasar candidates selected from imaging of Sloan Digital Sky Survey (SDSS) quasars with the *Subaru* Hyper Suprime-Cam Subaru Strategic Program (HSC-SSP). Using 2D image decomposition, our selection identifies point spread function-like companions within 0.6–4 arcsec separation ($\lesssim$ 30 kpc) around the SDSS quasar. We newly confirm 6 broad-line dual quasars and 11 offset quasars (quasar–galaxy pairs), spanning $1.5 < z < 3.3$ for the duals and predominantly $z < 0.6$ for the offset systems. No obvious lensed quasars were discovered from this program. We obtained 99 spectra of these candidates from NTT/EFOSC2 (New Technology Telescope ESO Faint Object Spectrograph and Camera version 2), Gemini/GMOS-N (Gemini Multi-Object Spectrograph on Gemini North), Keck/NIRES (Near-Infrared Echellette Spectrometer), and *Subaru*/FOCAS (Faint Object Camera and Spectrograph). From the spectra, we measure the emission-line properties of these dual black holes (BHs). At $z > 1.5$, the confirmed duals exhibit high BH mass ($M_{\rm BH} = 10^{8.5}$–$10^{10}{\rm M}_{\odot}$) with high bolometric luminosities ($L_{\rm bol} = 10^{45.5}$–$10^{47.5}$ erg s^{-1}), yet accrete at moderate Eddington ratios ($\lambda_{\rm Edd}$ =0.01–0.4). From the spectroscopically confirmed samples, we estimate the dual fraction of SDSS quasars with separations of 0.6–4 arcsec to be 0.2 per cent–1.2 per cent at $z < 0.8$, 0.08 per cent–0.24 per cent at $0.8 < z < 1.5$, and 0.06 per cent at $1.5 < z < 3.3$. These values are broadly consistent with other recent optical studies, but lower than theoretical expectations of a rising dual fraction at cosmic noon. However, we note that these fractions, especially at high z, still need a more accurate assessment of selection and observation effects.

Key words: methods: observational – quasars: individual: HSC-SSP – quasars: supermassive black holes.

1 INTRODUCTION

Dual supermassive black holes (SMBHs; $M_{\rm BH} \gtrsim 10^6\ M_{\odot}$) are an inevitable outcome of galaxy mergers in the hierarchical growth of structure (M. C. Begelman, R. D. Blandford & M. J. Rees 1980). Gas inflows triggered by mergers can fuel the SMBHs, igniting them as quasars (T. Di Matteo, V. Springel & L. Hernquist 2005; P. F. Hopkins et al. 2006; P. F. Hopkins & E. Quataert 2010). When both SMBHs are simultaneously accreting, they appear as a dual quasar system on kiloparsec scales. The frequency and properties of such systems are therefore the key to understanding the statistical importance and physical mechanisms of mergers in triggering quasars, which is still under debate (e.g. S. L. Ellison et al. 2011; J. Silverman et al. 2011; E. Treister et al. 2012; C. Villforth et al. 2014; B. Villarroel et al. 2017; V. Marian et al. 2019, 2020; Y. Zhao et al. 2022; S. Tang et al. 2023). Dual quasars also trace the small-scale clustering of quasars (J. F. Hennawi et al. 2006; S. Eftekharzadeh et al. 2017) and represent progenitors of parsec-scale SMBH binaries, which are expected to generate the nanohertz gravitational-wave background now reported by multiple pulsar timing array collaborations (G. Agazie et al. 2023) and of future space-based detections with the Laser Interferometer Space Antenna (LISA; P. Amaro-Seoane et al. 2017; M. Colpi & A. Sesana 2017).

Of particular interest are duals with physical separations $\lesssim$30 kpc, corresponding to the later stages of mergers prior to coa-

★ E-mail: st1c23@soton.ac.uk

lescence. Simulations show that tidal torques and shocks reduce gas angular momentum, boosting both star formation and SMBH accretion and increase the likelihood that both SMBHs are active (P. F. Hopkins & E. Quataert 2010; S. Van Wassenhove et al. 2012; P. R. Capelo et al. 2015, 2017). Cosmological simulations broadly indicate that the dual-AGN (active galactic nucleus) fraction increases toward $z \sim 2$–3, with comoving number densities of order 10^{-4}–10^{-3} Mpc^{-3} for $L_{\rm bol} > 10^{43}$ erg s^{-1} and separations $\lesssim 30$ kpc, although predictions vary with model assumptions and selection criteria (L. K. Steinborn et al. 2016; Y. M. Rosas-Guevara et al. 2019; M. Volonteri et al. 2022; V. Saeedzadeh et al. 2024). Wide-field surveys are therefore essential to identify such systems in statistically meaningful numbers.

Early systematic searches were driven by Sloan Digital Sky Survey (SDSS) imaging and spectroscopy (e.g. J. F. Hennawi et al. 2006; N. Inada et al. 2008, 2012; J. F. Hennawi et al. 2010; I. Kayo & M. Oguri 2012; A. More et al. 2016), demonstrating an excess of quasar pairs on $\lesssim$100 kpc scales (S. Eftekharzadeh et al. 2017). However, SDSS's fibre collision issue, seeing-limited imaging, and spectroscopic depth bias such samples toward relatively wide separations (typically a few arcseconds) and bright quasars ($i \lesssim 20$). More recently, *Gaia* has enabled all-sky searches at sub-arcsecond scales. 'Varstrometry' exploits small-scale astrometric jitter from unresolved pairs with independently varying light curves (H.-C. Hwang et al. 2020; Y. Shen et al. 2021; Y.-C. Chen et al. 2022), while the Gaia Multi-Peak method identifies multiple peaks in the along-scan light profile (F. Mannucci et al. 2022, 2023; A. Ciurlo et al. 2023; M. Scialpi et al. 2024). While powerful, these approaches are limited to bright quasars ($G \lesssim 20.5$) and are prone to contamination from host galaxies, making them most effective at $z \gtrsim 1$.

Building on the method of J. D. Silverman et al. (2020) as described in Section 2.1, we initiated an image-based dual-quasar search within the *Subaru* Hyper Suprime-Cam Subaru Strategic Program (HSC-SSP) footprint. The HSC Wide layer reaches $i \simeq 26$ (5σ) with median seeing $\sim$0.6 arcsec (H. Aihara et al. 2022), enabling discovery of pairs several magnitudes fainter than the *Gaia* selections. Our candidates are typically detected as one quasar with SDSS but two separate sources with HSC, with angular separations $\gtrsim$0.6 arcsec (seeing limited), placing our parameter space squarely between SDSS-resolved pairs and *Gaia* sub-arcsecond candidates (see S. Tang et al. 2025 for a literature summary and our HSC-selected sample). In a companion work, we have also tuned the pipeline to select out more closely separated pairs with $<$0.6 arcsec in HSC (Q. Wang et al. 2026). Importantly, this image-based approach can be scaled to next-generation wide-field surveys such as the Rubin Observatory Legacy Survey of Space and Time (LSST).

In J. D. Silverman et al. (2020) and S. Tang et al. (2021), we reported spectroscopic follow-up of 32 HSC-selected candidates and confirmed six dual quasars. Here, we present additional spectroscopy for 90 HSC-selected candidates, confirming six dual quasars and eleven quasar–galaxy pairs – 17 physical pairs in total.

The paper is organized as follows. Section 2 describes sample selection, observing setups, data reduction, and analysis. Section 3 summarizes our classification using spectroscopy and HSC imaging, and presents emission-line and BH property measurements for the duals. Section 5 discusses success rates, selection biases, and caveats. We adopt a flat Lambda-cold dark matter cosmology with $\Omega_\Lambda = 0.7$, $\Omega_{\rm m} = 0.3$, and $H_0 = 70$ km s^{-1} Mpc^{-1}.

2 METHODS

2.1 Candidate selection

The parent sample of this work was constructed following the procedure in J. D. Silverman et al. (2020). Briefly, we matched the SDSS DR14 quasar catalogue (DR14Q; I. Pâris et al. 2018) against the *Subaru* HSC-SSP footprint. The DR14Q contains 526 265 spectroscopically confirmed quasars selected by colour and magnitude criteria up to $z \sim 5$ (G. T. Richards et al. 2001, 2002; A. D. Myers et al. 2015). For HSC imaging, we used the s20a_wide release, included in Public Data Release 3 (PDR3; H. Aihara et al. 2022), which covers 1264 deg^2 in the i band, of which 881 deg^2 reaches the full 5σ depth of $i \simeq 26.2$ mag. This overlap yielded 59 482 SDSS quasars imaged in HSC and with i-band CModel photometry.

We then applied the 2D image decomposition tool GALIGHT (X. Ding et al. 2022) to the HSC i-band data to identify dual-quasar candidates. A candidate is defined as an SDSS quasar with an additional unresolved source detected [i-band point spread function (PSF) magnitude brighter than 24.5] within a projected radius of 0.6–4 arcsec. The lower bound is set by the typical HSC seeing ($\sim$ 0.6 arcsec), while the upper bound complements SDSS-based searches, which were largely limited to pairs with wider separations. This procedure yielded 1007 candidates, of which 30 were located at survey edges and lacked full multiband coverage. Removing these leaves 977 candidate pairs. We then visually inspected and rejected 89 sources contaminated by artefacts, saturated stars, and extended foreground galaxies. We further rejected five confirmed lens systems from literature (N. Inada et al. 2008, 2012; N. Jackson et al. 2012). Our final s20a_wide parent sample list consists of 883 dual quasar candidates. We did not reject the objects that have galaxy-like photometry to identify potential type 1–type 2 pairs and offset quasars (more discussions about such pairs will be presented in Araujo et al., in preparation). Here, we report spectroscopic follow-up observations of 90 candidates drawn from the s20a_wide sample.

Fig. 1 presents *gri*-composite HSC cutouts (10 arcsec per side) of the 90 observed systems. The SDSS J2000 designation of the known quasar is shown at the top of each panel, with its spectroscopic redshift noted at the bottom left, and the angular separation plotted as a scale bar at bottom right. The confirmed dual quasars and offset quasars are marked with red and blue frames, respectively. For these physical pairs, we note their projected separation ($R_\perp$ in kpc) in the panel.

Table 1 lists basic information for the observed candidates. Column (2) gives the spectroscopic redshift of the known SDSS quasar from DR14Q. For close pairs, the standard HSC pipeline forced photometry (S. Huang et al. 2017) can suffer from deblending failures. Therefore, refined photometric measurements from GALIGHT are adopted. Columns (3)–(6) provide the PSF-fitted coordinates of the quasar (qso_RA and qso_DEC) and its companion (com_RA and com_DEC), measured using GALIGHT. Each system was modelled as two PSFs plus, where required, additional Sérsic profiles for extended components. The PSFs were generated from the HSC pipeline using PSFEX (E. Bertin 2013; J. Bosch et al. 2018). We assume consistent source positions across all five bands, with reported coordinates measured from the i-band images. Based on these positions, we compute angular separations (Sep, arcsec) and projected physical separations ($R_\perp$, kpc). Columns (9) and (10) list the PSF magnitudes of the quasar and companion in the g

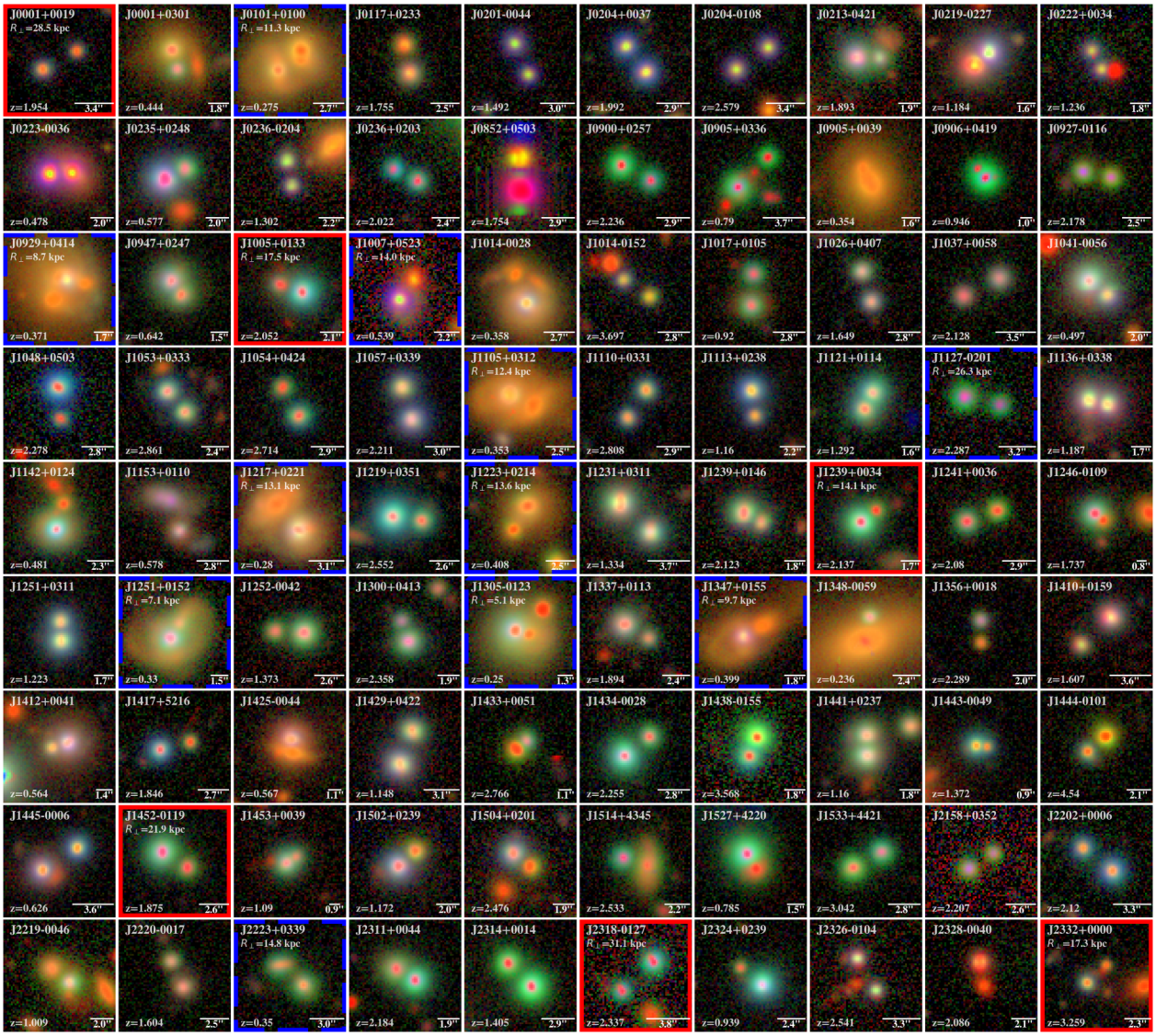

Figure 1. HSC coloured images of all 90 candidates that are observed in this work. The side length of each cutout stamp is 10 arcsec. North is to the up, and east to the left side. The spectroscopic redshifts of the SDSS quasars are labelled at the bottom left. The angular separations between the two sources of each pair are plotted as a scale bar at the bottom right. The confirmed 6 dual quasars and 11 offset quasars are marked with solid and dashed frames, respectively. For these physical pairs, their projected physical separations ($R_\perp$) are noted at the top left.

band. The full table, including photometry in all five bands for all 90 candidates, is available in the online version.

2.2 Observations

Long-slit spectroscopy was carried out with four ground-based facilities. For each target, we determined the relative positions of the two sources from the HSC *i*-band images and rotated the slit position angle (PA) to simultaneously cover both.

2.2.1 NTT/EFOSC2

We observed 60 targets using the ESO Faint Object Spectrograph and Camera version 2 (EFOSC2, B. Buzzoni et al. 1984) on the 3.58-m NTT at La Silla. Observations were conducted during three programs in 2021–2022: 105.20MF (P107, PI: K. Jahnke), 108.22F0 (PI: M. Onoue), and 109.23BF (PI: M. Onoue). In total, six nights of data were successfully obtained. The instrumental setups and weather conditions are summarized in Table 2. We used a fixed 1 arcsec slit with either grism no. 5 (5200–9350 Å) or no. 6 (3860–8070 Å), both offering 2.06 Å pixel^{-1} and ∼15.5 Å FWHM (full width at half-maximum) resolution. The CG375 order-blocking filter was applied in runs using grism no. 6 (P108 and P109). Seeing varied between 1 arcsec and occasionally 2 arcsec. The wavelengths are calibrated with the Ar/He lamps, and fluxes are calibrated with standard stars EG 21, EG 274, and LTT 1788 (J. Oke 1990).

In Table 2, the rows of the companions that are found at the same redshift of the known SDSS quasar (velocity offset < 500 km s^{-1}) are highlighted with bold fonts. Otherwise, the companion is a projected source. The superscripts 'G', 'K', and 'S' on top of the source names indicate additional observations with Gemini (Table 3), Keck (Table 4), and *Subaru* (Table 5) on the same source. They are noted with superscript 'N' (refer to NTT) in those tables

Table 1. Basic information of the observed dual quasar candidates.

	Name (J2000) (1)	Specz (2)	qso_RA (deg) (3)	qso_DEC (deg) (4)	com_RA (deg) (5)	com_DEC (deg) (6)	Sep (arcsec) (7)	$R_\perp$ (kpc) (8)	qso_g (AB) (9)	com_g (AB) (10)	... ...
1	000129.98 + 001911.3	1.9599	0.37492	0.31985	0.37409	0.32030	3.4	28.52	21.80	22.74	...
2	000157.44 + 030147.6	0.4440	0.48934	3.02992	0.48921	3.02945	1.8	10.29	20.67	21.07	...
3	010123.64 + 010045.3	0.2749	15.34851	1.01260	15.34795	1.01309	2.7	11.31	20.75	21.34	...
4	011728.83 + 023309.9	1.7552	19.37019	2.55275	19.37032	2.55344	2.5	21.14	21.02	22.20	...
5	020130.46–004448.9	1.4915	30.37693	−0.74691	30.37660	−0.74768	3.0	25.38	21.29	21.78	...
6	020425.44 + 003741.6	1.9921	31.10602	0.62821	31.10553	0.62757	2.9	24.28	20.72	20.35	...
7	020452.73–010822.4	2.5790	31.21977	−1.13957	31.21899	−1.13903	3.4	27.25	21.37	21.43	...
8	021322.99–042134.3	1.9053	33.34584	−4.35956	33.34530	−4.35956	1.9	15.98	19.21	21.16	...
9	021907.35–022715.2	1.1836	34.78065	−2.45426	34.78098	−2.45456	1.6	13.24	18.61	19.25	...
10	022225.92 + 003401.7	1.2360	35.60796	0.56717	35.60772	0.56672	1.8	14.99	21.74	21.61	...
...	...	...	...	...	...	...	...	...	...	...	...

Notes. Column (2): spectroscopic redshift of the known SDSS quasar in each pair. Columns (3)–(6): PSF positions of the known SDSS quasar (qso_RA and qso_DEC) and the companion source (com_RA and com_DEC) in each pair. Columns (7) and (8): the separation between the two nuclei in arcsec and projected physical distance (kpc), assuming them to be at the same redshift. Columns (9) and (10): *g*-band PSF magnitudes (after decomposing the host galaxy if detected) of the known SDSS quasar (qso_g) and the companion (com_g) source. The full table, including 90 sources and photometry of the other four bands, is available via the online version.

correspondingly. The classification of these sources is based on the combined spectrum. The above mentioned three tables also follow the same format as this table.

2.2.2 Gemini/GMOS-N

We observed 30 candidates with the Gemini Multi-Object Spectrograph on Gemini North (GMOS-N; I. Hook et al. 2004) in queue mode during three programs: GN-2020A-Q-108, GN-2020B-Q-116, and GN-2021A-Q-121 (PI: J. Silverman). Observational details are listed in Table 3. A slit width of 0.75 arcsec was used in 2020A, while 1 arcsec slits were used in 2020B and 2021A.

We employed the *B*600 grating with the CG455 filter and the *R*831 grating with the OG515 filter. The central wavelength setting (in μm) is reported in Table 3. The *B*600 grating provides a dispersion of 0.45 Å pixel^{-1} and spectral resolution $R = \lambda/\Delta\lambda \approx 1688$, while *R*831 offers 0.34 Å pixel^{-1} and $R \approx 4396$. Under queue scheduling, observations were executed in median conditions, corresponding to a typical seeing of ~ 0.5 arcsec at Maunakea (R. Lyman, T. Cherubini & S. Businger 2020). CuAr lamps were used for wavelength calibration, and the spectrophotometric standards HZ 44 and Feige 66 (J. Oke 1990) were observed for flux calibration.

2.2.3 Keck II/NIRES

We observed four targets with the Near-Infrared Echellette Spectrometer (NIRES; J. C. Wilson et al. 2004) on the 10-meter Keck II telescope. The observations were conducted during half a night on 2022 February 22 (Program ID: U197, PI: X. Prochaska). The observing setups and weather conditions are summarized in Table 4. These targets were selected for follow-up after the NTT and Gemini runs to obtain complementary near-infrared spectroscopy. Adaptive optics was not employed because the natural seeing was sufficient to resolve the two sources. The slit width of NIRES is fixed at 0.55 arcsec. NIRES provides simultaneous coverage of 0.94–2.45 μm across five echelle orders, with a mean spectral resolution of $R \approx 2700$. We used an ABBA dithering sequence to enable accurate subtraction of the near-infrared sky background. Wavelength calibration was performed using night-sky OH lines, and the standard star Feige 110 was observed for flux calibration.

2.2.4 Subaru/FOCAS

We observed four targets with the Faint Object Camera and Spectrograph (FOCAS; N. Kashikawa et al. 2002) on the 8.2-m *Subaru* telescope. The observations were conducted during half a night on 2023 September 5 as filler time in Program S23B-116 (PI: S. Tang). The observing setups and weather conditions are summarized in Table 5. These targets were selected as follow-ups to the NTT sample to achieve higher SNR ratios and to detect additional diagnostic emission lines. We used the VPH850 grating in combination with the SO58 order-sorting filter, which provides a wavelength coverage of 5800–10350 Å at a spectral resolution of $R \approx 1500$. A slit of type `SCFCSLLC08` with 0.5 arcsec width was used for all targets. Wavelength calibration was performed using ThAr arc lamps, and the standard star BD + 28D4211 was observed for flux calibration.

2.3 Data analysis

2.3.1 Spectrum reduction

All spectroscopic data in this work were reduced using the Python Spectroscopic Data Reduction Pipeline (PypeIt, J. X. Prochaska et al. 2023), a semi-automated package for astronomical spectroscopy. The general procedures follow the documentation of PypeIt (https://pypeit.readthedocs.io/en/latest/ J. X. Prochaska et al. 2020).

In brief, the pipeline first trims the overscan region and applies a bad-pixel mask appropriate for each instrument. For Gemini/GMOS data, which are read out in three CCDs with four amplifiers each, PypeIt mosaics the 12 amplifier outputs into a single frame, an essential step for optimizing the wavelength solution. Flat frames are then used to trace the slit edges (and the echelle orders for Keck/NIRES), while arc frames provide a 2D wavelength solution across the detector. In the case of NIRES, which lacks arc lamps, the sky emission lines in the science expo-

Table 2. Observation setups, weather conditions, and classifications of the candidates observed with NTT/EFOSC2. The slit width is fixed to 1 arcsec.

Name (J2000) (1)	Grism + Filter (2)	PA (deg) (3)	Date (dd.mm.yy) (4)	Seeing (arcsec) (5)	Airmass (6)	Exposure (s) (7)	Type (8)	Note (9)
000129.98 + 001911.3	**Gr no. 6 + CG375**	**118**	**04.09.22**	**1.9**	**1.2**	**1000 × 3**	**quasar ($z = 1.946$)**	**(i-b), (ii-a), (iii-a), (iv-a2, b3)**
000157.44 + 030147.6	Gr no. 6 + CG375	118	05.09.22	0.9	1.5	1000 × 3	A star	(v-a)
010123.64 + 010045.3	**Gr no. 5**	**131**	**05.09.22**	**0.8**	**1.5**	**800 × 3**	**LRG ($z = 0.275$)**	**(v-cd)**
011728.83 + 023309.9	Gr no. 6 + CG375	11	04.09.22	1.7	1.2	1000 × 3	G star	–
020130.46–004448.9	Gr no. 6 + CG375	23	05.09.22	0.8	1.5	1000 × 4	O star	(v-a)
020425.44 + 003741.6	Gr no. 6 + CG375	38	04.09.22	1.3	1.2	800 × 3	O star	(v-a)
020452.73–010822.4	Gr no. 6 + CG375	125	05.09.22	1.0	1.3	1200 × 3	O star	(v-a)
022225.92 + 003401.7	Gr no. 6 + CG375	29	05.09.22	1.7	1.2	1000 × 3	O star	(v-a)
022325.00–003612.6	Gr no. 6 + CG375	92	05.09.22	1.8	1.1	600 × 3	LRG ($z = 0$)	(v-bcd)
023546.83 + 024814.3	Gr no. 6 + CG375	118	05.09.22	1.8	1.2	1000 × 3	F star	(v-ad)
023606.55–020410.3	Gr no. 6 + CG375	11	04.09.22	1.4	1.1	1000 × 3	A star	(v-a)
023629.70 + 020327.5	Gr no. 6 + CG375	64	04.09.22	1.7	1.2	1000 × 3	A star	(v-d)
085244.38 + 050325.6	Gr no. 5 and Gr no. 6	2	14.04.21	0.9	1.2	600 × 6	K star	(v-bc)
090033.55 + 025727.9	Gr no. 6 + CG375	63	07.02.22	0.7	1.4	1000 × 3	K star	–
090500.09 + 033609.1	Gr no. 6 + CG375	135	07.02.22	0.75	1.3	1200 × 3	K star	–
090550.30 + 003948.1	Gr no. 5	31	09.04.22	0.8	1.2	600 × 3	Unclassified	Spatially unresolved
092725.37–011652.9	Gr no. 6 + CG375	79	07.02.22	0.5	1.1	1000 × 3	F/A star	(v-a)
094713.15 + 024743.6	Gr no. 6 + CG375	35	07.02.22	0.55	1.2	1000 × 3	F/A star	–
100547.80 + 013348.4	**Gr no. 6 + CG375**	**71**	**07.02.22**	**0.6**	**1.2**	**1200 × 3**	**quasar ($z = 2.055$)**	**(i-b), (ii-a), (iii-a), (iv-a2, b3)**
101419.40–002834.2	Gr no. 6	57	15.04.21	0.9	1.2	800 × 1	QG ($z = 0.34$?)	(v-a), slit misaligned, promising
101444.48–015244.2	Gr no. 6	20	14.04.21	0.95	1.1	1200 × 3	A star	(v-f)
102614.83 + 040730.6	Gr no. 6 + CG375	17	09.04.22	0.7	1.3	800 × 3	Quasar ($z = 1.18$?)	(i-b), (ii-b), (iii-a)
103737.45 + 005836.6	Gr no. 6 + CG375	116	09.04.22	0.7	1.2	1000 × 3	Quasar ($z = 1.708$)	(i-b), (ii-b), (iii-a)
104122.84–005618.4	Gr no. 6	53	13.04.21	0.8	1.1	600 × 4	F/A star	(v-ad)
104802.22 + 050301.0	Gr no. 6 + CG375	5	07.02.22	0.65	1.3	800 × 3	Quasar ($z = 2.019$)	(i-a), (ii-b), (iii-a)
105302.94 + 033355.8	Gr no. 6	40	13.04.21	0.85	1.2	1000 × 3	A star	(v-ad)
105409.83 + 042435.6	Gr no. 6 + CG375	116	09.04.22	0.8	1.2	800 × 3	F star	–
105716.18 + 033930.0	Gr no. 6	17	14.04.21	0.95	1.2	600 × 3	F star	–
110556.18 + 031243.1	**Gr no. 5**	**59**	**09.04.22**	**0.8**	**1.4**	**300 × 3**	**SFG/QG ($z = 0.356$)**	**(i-b), (ii-a), (iii-c), (v-a)**
111006.87 + 033107.1	Gr no. 6	146	14.04.21	0.9	1.2	800 × 3	F star	–
112144.76 + 011421.9	Gr no. 6	154	13.04.21	0.9	1.2	600 × 3	F star	(v-a)
112753.39–020142.7^K	**Gr no. 6**	**78**	**14.04.21**	**0.9**	**1.2**	**1200 × 3**	**SFG ($z = 2.292$)**	**(i-b), (ii-a), (iii-a), (iv-a2, b3)**
113613.37 + 033840.9	Gr no. 6	77	13.04.21	1.0	1.3	600 × 3	K star	–
114222.52 + 012443.8	Gr no. 6	164	15.04.21	0.9	1.2	800 × 3	unclassified	Faint but likely LRG
121745.76 + 022109.5	**Gr no. 5**	**40**	**15.04.21**	**0.9**	**1.2**	**800 × 3**	**SFG ($z = 0.281$)**	**(i-b), (ii-a), (iii-c), (v-bc)**
121912.94 + 035142.2^K	Gr no. 6 + CG375	82	07.02.22	0.7	1.2	800 × 3	F star	(v-a)
123101.66 + 031118.2^G	Gr no. 6	47	14.04.21	0.9	1.3	400 × 3	F/A star	(v-abcd)
123916.97 + 014654.2	Gr no. 6	62	13.04.21	0.9	1.3	1000 × 3	G star	–
124153.74 + 003648.0	Gr no. 6	110	14.04.21	0.9	1.3	1200 × 3	G star	–
125141.90 + 031140.9	Gr no. 6	1	13.04.21	1.2	1.2	800 × 3	F star	(v-a)
125258.75–004236.1	Gr no. 5	87	09.04.22	0.7	1.2	1000 × 3	G star	(v-a)
133709.29 + 011351.1	Gr no. 6 + CG375	60	09.04.22	1.0	1.2	1200 × 3	G star	–
134722.75 + 015504.9	**Gr no. 5**	**114**	**09.04.22**	**1.2**	**1.3**	**600 × 3**	**LRG ($z = 0.399$)**	**(v-ab)**
134826.86–005943.9	Gr no. 5	169	15.04.21	0.9	1.2	800 × 3	F star	(v-d)
135619.16 + 001813.3	Gr no. 6	1	15.04.21	0.9	1.3	800 × 3	Unclassified	Too faint
141235.36 + 004104.1	Gr no. 6	108	15.04.21	0.9	1.5	800 × 3	Unclassified	Too faint and blended
142944.25 + 042202.6	Gr no. 6 + CG375	160	09.04.22	1.3	1.4	1000 × 2	K star	(v-ad)
143452.74–002828.0	Gr no. 6 + CG375	128	09.04.22	1.1	1.4	1000 × 2	K star	(v-c)
143822.97–015557.9	Gr no. 6	158	13.04.21	0.75	1.2	1000 × 3	F/A star	–
144145.09 + 023743.0	Gr no. 6	1	13.04.21	0.8	1.3	600 × 3	F star	(v-a)
144407.63–010152.7	Gr no. 5	130	09.04.22	1.1	1.6	1000 × 2	Unclassified	Too faint and blended
144551.13–000650.3	Gr no. 6	122	14.04.21	0.9	1.4	800 × 3	F star	(v-d)
150257.02 + 023917.7	Gr no. 6	131	14.04.21	0.9	1.5	800 × 3	LRG ($z = 0.085$)	(v-a)
150414.02 + 020112.0	Gr no. 6	52	14.04.21	0.9	1.5	800 × 3	LRG ($z = 0.325$)	(v-b)
215824.40 + 035217.5^S	Gr no. 6 + CG375	122	04.09.22	2.0	1.4	1000 × 4	A star	(v-a)
220239.30 + 000650.0	Gr no. 6 + CG375	52	05.09.22	1.0	1.4	1000 × 3	A star	(v-d)
222050.95–001744.5^S	Gr no. 6 + CG375	25	04.09.22	1.7	1.2	1000 × 3	F star	(v-d)
231402.87 + 001430.2^S	Gr no. 6 + CG375	45	04.09.22	1.7	1.2	400 × 3	F star	(v-ad)
231854.69–012725.9^S	**Gr no. 6 + CG375**	**133**	**05.09.22**	**1.5**	**1.5**	**1000 × 3**	**quasar ($z = 2.346$)**	**(i-a), (ii-a), (iii-a), (iv-a2, b2)**
232610.23–010427.8	Gr no. 6 + CG375	29	04.09.22	1.9	1.2	800 × 3	O star	–

Notes. The classified type of the companion source of the pair is listed in column (8). The basis of classification is noted in column (9), as detailed in Section 3.1. The superscripts 'G', 'K', and 'S' on top of the source names indicate additional observations with Gemini, Keck, and *Subaru* on the same source. The bold lines highlight the confirmed physical pairs.

Table 3. Observation setups, weather conditions, and classifications for the candidates observed with Gemini/GMOS-N. The slit width is 0.75 arcsec in 2020A and 1 arcsec thereafter. Observations were carried out in queue mode; when multiple nights contributed to a source, only the principal date are listed.

Name (J2000) (1)	Grism + Filter (2)	PA (deg) (3)	Date (dd.mm.yy) (4)	Airmass (5)	Exposure (s) (6)	Type (spec) (7)	Note (8)
021907.35–022715.2	B600:0.580 + CG455	131.7	16.08.20	1.4	120 × 2	K star	(v-bc)
021322.99–042134.3	B600:0.580 + CG455	89.5	16.08.20	1.3	847 × 3	Quasar ($z = 0.97$)	(i-b), (ii-b), (iii-a)
090613.75 + 041923.1	R831:0.860 + OG515	40.7	22.12.20	1.1	847 × 7	unclassified	Too faint
092919.16 + 041414.2	**B600:0.680 + CG455**	**143.2**	**16.02.21**	**1.1**	**300 × 3**	**QG ($z = 0.369$)**	**(v-bcf)**
092919.16 + 041414.2	**B600:0.680 + CG455**	**74.7**	**16.02.21**	**1.1**	**300 × 3**	**QG ($z = 0.369$)**	**(v-bf)**
100701.56 + 052315.4	**B600:0.680 + CG455**	**144.8**	**16.02.21**	**1.1**	**600 × 3**	**QG ($z = 0.539$)**	**(v-bf)**
101719.42 + 010534.6	B600:0.630 + CG455	176.1	22.02.21	1.1	600 × 3	Unclassified	Featureless but promising
111347.70 + 023830.3	B600:0.630 + CG455	8	20.04.21	1.5	600 × 3	Quasar ($z = 1.596$)	(i-a), (ii-b), (iii-a)
115302.69 + 011027.8	R831:0.800 + OG515	73	14.04.21	1.1	600 × 3	SFG ($z = 0.075$)	(i-a), (ii-b), (iii-c)
122349.29 + 021449.1	**B600:0.680 + CG455**	**153.8**	**22.03.21**	**1.1**	**600 × 3**	**QG ($z = 0.408$)**	(v-ab)
123101.66 + 031118.2^{N}	B600:0.630 + CG455	46.6	21.03.21	1.1	300 × 2	F/A star	(v-abcd)
123939.06 + 003439.8^{K}	**R831:0.860 + OG515**	**127.4**	15.01.21	1.1	847 × 3	**Quasar ($z = 2.134$)**	**(i-a), (ii-a), (iii-a), (iv-a2, b3)**
124604.03–010954.6	B600:0.660 + CG455	51.9	20.05.20	1.2	847 × 3	LRG ($z = 0.31$?)	(v-a)
125156.49 + 015249.7	**B600:0.630 + CG455**	**149.2**	**30.04.21**	**1.1**	**600 × 3**	**SFG/QG ($z = 0.33$)**	**(i-a), (ii-a), (iii-c), (v-bef)**
130550.51–012331.5	**B600:0.630 + CG455**	**75.9**	**15.04.21**	**1.1**	**600 × 3**	**SFG (z = 0.251)**	(i-a), (ii-a), (iii-c)
141003.70 + 015901.8	B600:0.630 + CG455	132.8	24.03.21	1.1	600 × 3	G star	(v-c)
141712.26 + 521655.8	R831:0.800 + OG515	103.8	15.04.21	1.2	600 × 6	Unclassified	Common absorptions, promising
142526.50–004421.5	R831:0.860 + OG515	5.4	23.05.20	1.1	847 × 1	QG ($z = 0.52$)	–
143316.38 + 005145.5	B600:0.660 + CG455	131.6	20.05.20	1.2	847 × 3	M1 star	(v-e)
144308.16–004913.4	B600:0.660 + CG455	84.2	20.05.20	1.2	847 × 4	Unclassified	Featureless but promising
145201.59–011945.3	**R831:0.800 + OG515**	**58.5**	**17.04.21**	**1.3**	**600 × 3**	**Quasar ($z = 1.876$)**	**(i-b), (ii-a), (iii-a), (iv-a1, b3)**
145347.46 + 003927.0	B600:0.660 + CG455	131.8	21.05.20	1.2	847 × 3	Unclassified	Featureless but promising
151434.38 + 434507.1	B600:0.630 + CG455	73.5	24.03.21	1.1	300 × 3	SFG ($z = 0.33$)	(i-a), (ii-b), (iii-c)
152750.12 + 422035.5	R831:0.800 + OG515	30.5	30.04.21	1.1	180 × 3	M1 star	(v-e)
153342.05 + 442106.5	B600:0.630 + CG455	118.4	24.03.21	1.1	500 × 3	Quasar ($z = 1.325$)	(i-b), (ii-b), (iii-a)
221926.32–004612.9	B600:0.580 + CG455	55.1	13.08.20	1.3	847 × 4	SFG ($z = 0.333$)	(i-a), (ii-b), (iii-c)
222327.52 + 033902.0	**B600:0.630 + CG455**	**49.2**	**14.05.21**	**1.6**	**600 × 3**	**SFG ($z = 0.35$)**	(i-a), (ii-a), (iii-c)
231148.54 + 004426.0	B600:0.580 + CG455	59.9	13.08.20	1.1	847 × 2	SFG ($z = 0.194$)	(i-a), (ii-b), (iii-c)
232443.06 + 023922.7	B600:0.630 + CG455	50.2	14.06.21	1.3	600 × 6	F star	–
232821.40–004045.2	R831:0.800 + OG515	9.5	02.08.21	1.1	600 × 6	M1 star	(v-e)
233225.33 + 000042.5	**B600:0.630 + CG455**	**135.4**	**04.07.21**	**1.3**	**600 × 12**	**Quasar ($z = 3.271$)**	(i-b), (ii-a), (iii-a), (iv-a2, b3)

Table 4. Observation setups, weather conditions, and classifications for the candidates observed with Keck/NIRES, the width of the slit is fixed to 0.55 arcsec.

Name (J2000) (1)	PA (deg) (2)	Date (dd.mm.yy) (3)	Seeing (arcsec) (4)	Airmass (5)	Exposure (s) (6)	Type (spec) (7)	Note (8)
112753.39–020142.7^{N}	**77.6**	**10.02.22**	**1.0**	**1.2**	**300 × 4**	**SFG ($z = 2.292$)**	**(i-b), (ii-a), (iii-a), (iv-a2, b3)**
121912.94 + 035142.2^{N}	81.9	10.02.22	0.8	1.4	300 × 4	F star	(v-a)
123939.06 + 003439.8^{G}	**127.4**	**10.02.22**	**1.4**	**1.1**	**300 × 4**	**Quasar ($z = 2.134$)**	**(i-a), (ii-a), (iii-a), (iv-a2, b3)**
130047.68 + 041320.4	18.7	10.02.22	1.0	1.2	300 × 8	Unclassified	Too faint, unable to extract spectrum

Table 5. Observation setups, weather conditions, and classifications for the candidates observed with *Subaru*/FOCAS, the width of the slit is fixed to 0.55 arcsec. All of the sources are also observed with NTT.

Name (J2000) (1)	PA (deg) (2)	Date (dd.mm.yy) (3)	Seeing (arcsec) (4)	Airmass (5)	Exposure (s) (6)	Type (spec) (7)	Note (8)
215824.40 + 035217.5^{N}	122	05.09.24	0.4	1.1	1200 × 3	F star	–
222050.95–001744.5^{N}	25	05.09.24	0.3	1.1	1000 × 2	F star	(v-d)
231402.87 + 001430.2^{N}	45	05.09.24	0.3	1.1	600 × 2	F star	(v-ad)
231854.69–012725.9^{N}	**133**	**05.09.24**	**0.4**	**1.1**	**1200 × 2**	**Quasar ($z = 2.346$)**	**(i-a), (ii-a), (iii-a), (iv-a2, b2)**

sures are used directly for wavelength calibration. Subsequently, the sky background is modelled and subtracted with an improved algorithm from D. D. Kelson (2003), yielding reduced 2D spectra.

We then extracted 1D spectra for each component of every pair. Because PYPEIT's automated extraction is not optimized for blended sources with separations of $\lesssim$1 arcsec, we implemented a custom three-step method: (1) from the reduced 2D spectrum, we binned the image along the wavelength axis to enhance Signal to Noise ratio (S/N) and fit a double-Gaussian profile at each row; (2) the Gaussian centres were then fit with a second-order polynomial to trace the spatial positions of the two spectra; and (3) using these traces, we refit double Gaussians at each wavelength position on the original 2D frame, and extracted the Gaussian areas as the photon counts. The resulting spectra were flux-calibrated using the sensitivity functions derived from standard stars within PYPEIT, and rescaled to match HSC photometry to correct for slit losses (see Appendix A for a comparison between our measurements of the PSF magnitudes and the HSC pipeline-generated CModel magnitudes).

2.3.2 *Spectrum fitting*

For the confirmed quasar–quasar and quasar–galaxy pairs, we fit the 1D spectra with the PYQSOFIT package (H. Guo, Y. Shen & S. Wang 2018; H. Guo et al. 2019; Y. Shen et al. 2019). When a source was observed with multiple telescopes, we first combined the spectra by resampling to a common wavelength array and weighted averaging in the overlapping wavelengths before fitting. All fitting was performed in the rest frame. For quasars at $z < 0.5$, we applied the prior-informed PCA method in PYQSOFIT to subtract host-galaxy emission (W. Ren et al. 2024).

For pure quasar spectra, the code first fits a pseudo-continuum consisting of a power-law plus a third-order polynomial plus an Fe II template in line-free windows: 6000–6250 and 6800–7000 Å around Hα, 4435–4630 and 5100–5535 Å around Hβ, and 2200–2700 and 2900–3090 Å around Mg II. Regarding the Fe II emission, the T. A. Boroson & R. F. Green (1992) model is applied to the UV part between 1200 and 3500 Å, and the M. Vestergaard & B. J. Wilkes (2001) model is applied to the optical part between 3686 and 7484 Å. More details about the compilation of the continuum and iron emission were discussed in Y. Shen et al. (2019). After subtracting the pseudo-continuum, the emission-line-only spectra were modelled with single or multiple Gaussian components, including the Hα composite (Hα broad and narrow, [N II] $\lambda\lambda$6549,6585, [S II] $\lambda\lambda$6718,6732), Hβ composite (Hβ broad and narrow, core and wing components of [O III] $\lambda\lambda$4959,5007), Hγ composite (Hγ broad and narrow, [O III] λ4364), Mg II, C III], C IV, Lyα, and N V λ1240.

The fitting returns the emission-line properties, including central wavelength, velocity dispersion, FWHM, equivalent width (EW), peak position, integrated flux, signal-to-noise ratio (SNR), and continuum parameters. The parameter uncertainties are estimated with the Markov chain Monte Carlo (MCMC) method. These fitting results are then employed to classify the types of sources and measure the BH property.

2.3.3 *BH property measurements*

For the broad-line AGNs with FWHM $>$ 2000 km s^{-1}, we derived their black hole (BH) masses using the single-epoch virial method, which is calibrated against reverberation mapping (S. Kaspi et al. 2000):

$$M_{\rm BH} = 10^{\alpha} L^{\beta} \left(\frac{\rm FWHM}{1000\ {\rm km\ s^{-1}}} \right)^{\gamma} {\rm M}_{\odot}, \quad (1)$$

where L is the relevant continuum or line luminosity. In this work, we adopt the calibrations of Y. Shen et al. (2011) for Hα, M. Vestergaard & B. M. Peterson (2006) for Hβ and C IV, and A. Schulze et al. (2017) for Mg II. The corresponding parameters are listed in Table 6. The total uncertainties include both measurement errors (from the PYQSOFIT MCMC fits) and the intrinsic systematic uncertainty of the virial method, $\sim$0.4 dex (Y. Shen et al. 2011; A. Schulze et al. 2018). We note that the C IV BH estimator is known to be systematically biased compared to the Balmer estimators due to its outflow-related origin (H. Netzer 2015; L. Coatman et al. 2016). The blueshift of the C IV line might be used to mitigate this bias (L. Coatman et al. 2017), which, however, requires a robust measurement of the systematic redshift of the quasar. For our newly confirmed dual quasars with C IV detections (Table 7), the spectrum coverages are all limited to rest wavelengths $<$3000 Å, and thus lack a robust redshift estimator. We therefore did not apply any correction to the C IV-based BH masses.

Table 6. Parameters of the virial BH mass calibration (equation 1). Luminosities are defined as follows: $L_{1350,44}$ is the monochromatic luminosity at 1350 Å in units of 10^{44} erg s^{-1}, and similarly for $L_{3000,44}$, $L_{5100,44}$, and $L_{{\rm H}\alpha,42}$ (in units of 10^{42} erg s^{-1}).

Line	L	α	β	γ
C IV	$L_{1350,44}$	6.66	0.5	2
Mg II	$L_{3000,44}$	6.74	0.62	2
Hβ	$L_{5100,44}$	6.91	0.5	2
Hα	$L_{{\rm H}\alpha,42}$	6.71	0.48	2.12

Bolometric luminosities were estimated from the monochromatic continuum luminosities as $L_{\rm bol} = 3.81 \times L_{1350}$, $5.15 \times L_{3000}$, and $9.26 \times L_{5100}$, respectively (G. T. Richards et al. 2006). The Eddington luminosity and Eddington ratio are then:

$$\begin{aligned} L_{\rm Edd} &= 1.26 \times 10^{38} M_{\rm BH} \\ \lambda_{\rm Edd} &= L_{\rm bol}/L_{\rm Edd} \end{aligned} \quad (2)$$

3 RESULTS

3.1 Source type classification

We classified the spectral types of the companion sources in each pair primarily by cross-correlation with the SDSS spectral templates.[1] The abbreviations and the corresponding SDSS templates are as follows: (1) quasar (SDSS templates nos 30 and 33); (2) LRG (template 29): luminous red galaxy (LRG); (3) QG (template 24): quiescent ('early-type') galaxy; (4) SFG (templates 25–28): star-forming ('late-type') galaxy; and (5) stars: classified by the corresponding stellar templates (templates 1–23). We note that these templates are sufficient for the classification purpose of this paper, and that more objective and complete galaxy templates can be found in, e.g. D. Fraix-Burnet, C. Bouveyron & J. Moultaka (2021). The final classifications of our sources are listed in the 'Type' columns of Tables 2–5. Rows corresponding to physical pairs (dual quasars and quasar–galaxy pairs at the same redshift)

[1] https://classic.sdss.org/dr5/algorithms/spectemplates/

Table 7. Broad emission-line measurements of the newly confirmed dual quasars. For each source, the broad component of the listed lines is reported with SNR ratio (in σ), FWHM (in km s^{-1}), and EW (in Å). Lines not covered by our spectra are indicated as '–', and lines covered but undetected (SNR < 1σ) are shown as '...'. Newly confirmed companion sources in each pair are highlighted in bold fonts.

Name	Redshift		C IVλ1549			C III]λ1909			Mg IIλ2799			Hβ			Hα		
		SNR (σ)	FWHM (km s^{-1})	EW (Å)	SNR (σ)	FWHM (km s^{-1})	EW (Å)	SNR (σ)	FWHM (km s^{-1})	EW (Å)	SNR (σ)	FWHM (km s^{-1})	EW (Å)	SNR (σ)	FWHM (km s^{-1})	EW (Å)	SNR (σ)	FWHM (km s^{-1})	EW (Å)
0001 + 0019_N	1.9457	6.0 ± 1.0	2874 ± 670	53 ± 10	2.1 ± 0.6	5639 ± 5643	36 ± 14	–	–	–	–	–	–	–	–	–	–	–	–
0001 + 0019_S	1.9474	5.7 ± 0.6	10568 ± 1059	128 ± 11	2.6 ± 0.5	6457 ± 1200	22 ± 4	–	–	–	–	–	–	–	–	–	–	–	–
1005 + 0133_N	2.0551	5.3 ± 1.0	5124 ± 2257	21 ± 4	...	...	...	–	–	–	–	–	–	–	–	–	–	–	–
1005 + 0133_S	2.0525	13.2 ± 0.2	4256 ± 89	30 ± 0	4.9 ± 0.1	8105 ± 409	30 ± 1	–	–	–	–	–	–	–	–	–	–	–	–
1239 + 0034_N	2.1338	–	–	–	–	–	–	2.3 ± 0.0	6712 ± 199	29 ± 1	2.6 ± 0.1	16950 ± 875	821 ± 35	5.0 ± 0.3	8093 ± 350	599 ± 22			
1239 + 0034_S	2.1371	–	–	–	–	–	–	6.7 ± 0.0	4095 ± 11	24 ± 0	6.7 ± 0.2	10383 ± 90	65 ± 1	16.5 ± 2.3	5734 ± 443	251 ± 15			
1452–0119_N	1.8753	–	–	–	–	–	–	14.3 ± 0.1	3857 ± 51	44 ± 1	–	–	–	–	–	–			
1452–0119_S	1.8755	–	–	–	–	–	–	6.9 ± 0.4	3339 ± 218	33 ± 2	–	–	–	–	–	–			
2318–0127_N	2.3369	5.6 ± 0.2	8312 ± 494	82 ± 4	9.4 ± 0.2	8389 ± 128	35 ± 0	7.8 ± 0.1	7684 ± 115	41 ± 1	–	–	–	–	–	–			
2318–0127_S	2.3461	4.0 ± 0.5	10796 ± 1369	68 ± 7	6.5 ± 0.2	10141 ± 270	31 ± 1	4.5 ± 0.1	10118 ± 260	41 ± 1	–	–	–	–	–	–			
2332 + 0000_N	3.2706	2.0 ± 0.1	11944 ± 961	38 ± 2	–	–	–	–	–	–	–	–	–	–	–	–			
2332 + 0000_S	3.2649	6.4 ± 0.1	10926 ± 147	58 ± 0	–	–	–	–	–	–	–	–	–	–	–	–			

are highlighted in bold fonts. The basis of classification is noted in the final columns of the tables. In particular, we considered the following conditions:

(i) *Emission-line detection.*

(a) More than two emission lines detected above 3σ.
(b) Only one emission line detected above 3σ.
(c) Only tentative emission-line detections below 3σ.

(ii) *Emission-line position.*

(a) Velocity offset from the known SDSS quasar < 500 km s^{-1}.
(b) Velocity offset > 500 km s^{-1}.

(iii) *Emission-line width.*

(a) FWHM > 2000 km s^{-1}.
(b) 1200 < FWHM < 2000 km s^{-1}.
(c) FWHM < 1200 km s^{-1}.

(iv) *Lensing.*

(a) Comparison of the two spectra:

(1) Nearly identical (standard deviation of the flux ratios <50 per cent of their median).
(2) Non-identical (standard deviation >50 per cent of the median).

(b) HSC imaging:

(1) A third source detected between the two objects.
(2) A third source detected within 3 arcsec of the system.
(3) No third source detected within 3 arcsec.

(v) *Absorption-line detection.*

(a) Ca II H&K $\lambda\lambda$3934.8, 3969.6.
(b) Mg I λ5176.7.
(c) Na I λ5895.6 ('D' line).
(d) Balmer absorption lines.
(e) TiO molecular bands.

Our classification strategy is as follows. If at least one emission line is detected above 3σ (condition i), we measure the velocity offset relative to the SDSS quasar (Condition ii). Previous works (e.g. J. F. Hennawi et al. 2006, 2010) used 2000 km s^{-1} as the threshold, accounting for both the expected peculiar velocities of bound quasar pairs ($\lesssim$ 500 km s^{-1}) and SDSS redshift uncertainties ($\sim$1500 km s^{-1}). Since none of our observed systems have velocity offsets between 500–2000 km s^{-1}, the choice of this threshold within this range will not affect our results. Here, we adopt 500 km s^{-1} as the criterion. If the offset exceeds this threshold (condition ii-b), we classify the system as a projected pair.

Meanwhile, we use the emission-line width to distinguish between quasars and galaxies. Sources with FWHM >2000 km s^{-1} are classified as quasars; those with FWHM <1200 km s^{-1} as star-forming galaxies (SFGs); and those in between as composites (L. Hao et al. 2005; Y. Shen et al. 2011). The 1200 km s^{-1} threshold is a very conservative assumption as the typical FWHM of SFGs is 200–300 km s^{-1}. Nevertheless, none of our sources has FWHM in between 1200–2000 km s^{-1}. There are two offset quasars with their companions having FWHM >500 km s^{-1}:

Table 8. BH properties of the confirmed dual quasars in this work.

Name	$\log L_{\rm bol}^{1350\text{Å}}$ (erg s^{-1})	$\log L_{\rm bol}^{3000\text{Å}}$ (erg s^{-1})	$\log L_{\rm bol}^{5100\text{Å}}$ (erg s^{-1})	$\log M_{\rm BH}^{\rm C\,IV}$ ($M_\odot$)	$\log M_{\rm BH}^{\rm Mg\,II}$ ($M_\odot$)	$\log M_{\rm BH}^{\rm H\beta}$ ($M_\odot$)	$\log M_{\rm BH}^{\rm H\alpha}$ ($M_\odot$)	$\log \lambda_{\rm Edd}$
(1)	(2)	(3)	(4)	(5)	(6)	(7)	(8)	(9)
0001 + 0019_N	45.84	–	–	8.44 ± 0.45	–	–	–	−0.71
0001 + 0019_S	45.69	–	–	9.48 ± 0.41	–	–	–	−1.90
1005 + 0133_N	46.37	–	–	9.27 ± 0.55	–	–	–	−1.01
1005 + 0133_S	47.50	–	–	9.81 ± 0.40	–	–	–	−0.42
1239 + 0034_N	–	45.77	45.87	–	9.05 ± 0.40	9.82 ± 0.40	9.49 ± 0.40	−1.78
1239 + 0034_S	–	46.82	46.94	–	9.27 ± 0.40	9.93 ± 0.40	9.51 ± 0.41	−0.75
1452−0119_N	–	46.65	–	–	9.12 ± 0.40	–	–	−0.58
1452−0119_S	–	45.98	–	–	8.57 ± 0.40	–	–	−0.70
2318−0127_N	46.50	–	–	9.77 ± 0.40	–	–	–	−1.38
2318−0127_S	46.25	–	–	9.84 ± 0.41	–	–	–	−1.71
2332 + 0000_N	45.65	–	–	9.56 ± 0.41	–	–	–	−2.02
2332 + 0000_S	46.44	–	–	9.97 ± 0.40	–	–	–	−1.64

Notes. Columns (2)–(4) list bolometric luminosities ($L_{\rm bol}$) estimated from monochromatic luminosities at 1350, 3000, and 5100 Å. Columns (5)–(8) give BH masses ($M_{\rm BH}$) derived from the virial method using broad emission lines. Column (9) reports the Eddington ratio ($\lambda_{\rm Edd}$). Where multiple measurements exist, averages are adopted for $\lambda_{\rm Edd}$.

J112753.39−020142.7 and J121745.76 + 022109.5, which we will discuss in detail in Section 4.2. We do not adopt the BPT diagrams in our main classification procedure, as the spectra of most of our offset pairs do not cover both axes. It will be discussed in detail if available for specific cases.

If the companion satisfies conditions (i), (ii-a), and (iii-a/b),[2] we further assess whether the system could be a lensed quasar. In the most straightforward case, if the spectral ratio is non-identical across the wavelength range (condition iv-a2) and no third source is detected in the HSC image (condition iv-b3), we can confidently reject lensing and classify the system as a dual quasar. For more ambiguous cases, we provide object-specific discussions in Section 4.

If no emission lines are detected, the source is most likely a quiescent galaxy (QG) or a star (but can also be quasars merely covered with weak emission lines). In such cases, we attempt to match the continuum shape to SDSS templates and identify redshifts from strong absorption features, including the Fraunhofer lines (Ca II H&K, Mg I λ5176.7, Na I λ5895.6), Balmer absorption, and TiO bands.[3] If the spectrum is featureless but has sufficient S/N, we match the continuum slope to SDSS templates to assign a classification. Unclassified cases are generally due to blending or insufficient S/N, as described in the 'Note' column of the tables.

In total, we have classified 6 systems as broad-line quasar pairs and 11 systems as offset quasars (quasar–galaxy pairs). The redshifts of these pairs are between 0.2 and 3.3, the angular separations are between 1.3 and 3.8 arcsec, corresponding to projected separations between 5 and 31 kpc. The maximum flux ratio between the two sources of each pair is ∼15, as estimated from the spectrum. The faintest case has *i*-band magnitude of 22.6.

3.2 Physical properties of the dual quasars

We present the broad emission-line properties of the confirmed dual quasars in Table 7, measured with PyQSOFit (Section 2.3.2). Within each pair, the newly confirmed companion source is highlighted in bold. For the broad component of each line, we report the SNR ratio (in σ), FWHM (in km s^{-1}), and EW (in Å). Lines not covered by our observations are denoted with '–', while covered but undetected lines (SNR $< 1\sigma$) are marked with '···'.

From the continuum and emission-line fitting results, we estimate the BH properties of the dual quasars as described in Section 2.3. Table 8 lists the bolometric luminosity ($L_{\rm bol}$), BH mass ($M_{\rm BH}$), and Eddington ratio ($\lambda_{\rm Edd}$) for our six newly confirmed dual quasars. For the pair of J1239 + 0034, multiple estimators of $L_{\rm bol}$ and $M_{\rm BH}$ are available, we adopt $L_{\rm bol}^{5100\text{Å}}$ and $M_{\rm BH}^{\rm H\alpha}$ when computing $\lambda_{\rm Edd}$. For the pair of J2318−0127, although Mg II is detected in the spectrum, L_{3000} falls at the edge of the coverage, thus $L_{\rm bol}^{3000}$ and $M_{\rm BH}^{\rm Mg\,II}$ were not measured for this case.

Fig. 2 compares the bolometric luminosities and BH masses of our confirmed dual quasars (including six pairs from J. D. Silverman et al. 2020; S. Tang et al. 2021) with the general SDSS quasar population (S. Rakshit, C. Stalin & J. Kotilainen 2020, shown as coloured contours). The left panel shows the $z < 1$ systems, while the right panel presents the $z > 1.5$ systems. In each panel, the two quasars within a given pair are plotted with the same coloured star symbols. Representative uncertainties for $M_{\rm BH}$ and $L_{\rm bol}$ are shown as error bars in the upper left. These uncertainties are dominated by systematics: ∼0.4 dex for $M_{\rm BH}$ from the virial method (Y. Shen et al. 2011), and ∼0.13 dex for $L_{\rm bol}$ from optical/UV bolometric corrections (J. C. Runnoe, M. S. Brotherton & Z. Shang 2012). Statistical fitting uncertainties are negligible in most cases, as indicated by the PyQSOFit MCMC analyses.

All the dual quasars newly confirmed in this work are at $z > 1.5$. As shown in Fig. 2, they occupy the relatively high BH mass ($\log M_{\rm BH}/M_\odot \sim 8.5$–$10$) and wide range of bolometric luminosity ($\log L_{\rm bol}/{\rm erg\,s^{-1}} \sim 45.5$–$47.5$) region of the entire $z > 1.5$ SDSS quasar population. The dashed lines indicate constant Eddington ratios ($\lambda_{\rm Edd} = 1.0, 0.1, 0.01$). Most of our systems accrete at moderate to low Eddington ratios ($\lambda_{\rm Edd} \sim 0.01$–$0.4$), consistent with the broader single quasar population of similar mass (e.g. M. L. Jones et al. 2016).

All the low-redshift pairs in Fig. 2 were reported in our earlier work, from which we found that BH masses and host stellar masses of dual quasars are slightly elevated above the local $M_{\rm BH}$–M_* scaling relation (S. Tang et al. 2021). However, we cannot robustly measure host stellar masses for our new $z > 1.5$ dual

[2]Because the primary source is an SDSS quasar, if the companion is a narrow-line source (condition iii-c), it automatically rules out lensing.
[3]Line list from https://classic.sdss.org/dr6/algorithms/linestable.php

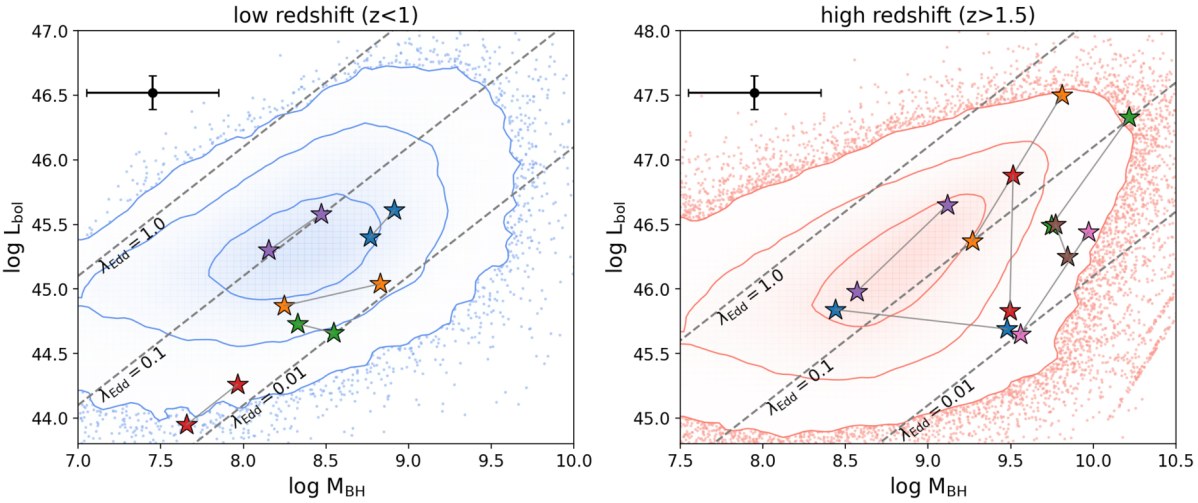

Figure 2. Bolometric luminosities versus BH masses for confirmed dual quasars by our project, including six pairs from our previous works. Each pair is labelled with two star marks of the same colour, and connected with a grey line. Left panel: $z < 1$ systems; and right panel: $z > 1.5$ systems. In each panel, the same coloured star marks indicate every two members of each pair. Representative uncertainties in $M_{\rm BH}$ and $L_{\rm bol}$ are shown in the top-left corner of each panel. Underlying contours show the 1σ, 2σ, and 3σ distributions of SDSS DR14 quasars in the corresponding redshift range. Dashed grey lines indicate constant Eddington ratios ($\lambda_{\rm Edd} = 1.0, 0.1, 0.01$).

quasars from HSC imaging and SED fitting alone. At these redshifts, space-based imaging is generally required to resolve quasar host galaxies (X. Ding et al. 2020). Alternatively, stellar masses can be approximated by subtracting the gas mass from the dynamical mass in submillimeter interferometric observations (e.g. M. Bischetti et al. 2017; S. Molyneux et al. 2025).

Crucially, neither our sample nor previous studies show compelling evidence that galaxy mergers systematically drive both BHs to near-Eddington accretion simultaneously. Instead, confirmed dual quasars exhibit $\lambda_{\rm Edd}$ distributions indistinguishable from those of single quasars, suggesting that while mergers can trigger concurrent nuclear activity, the detailed fuelling and duty cycle of each SMBH are controlled primarily by the local gas supply and feedback processes rather than by a wholesale boost in accretion efficiency (T. Kawaguchi, N. Yutani & K. Wada 2020). We also note that these dual quasars probably have not reached their peak of activity among the mergers, given that their physical separations are still above the kpc level. Numerical simulations suggested increasing AGN activities and accretion rate with decreasing separations between the BHs down to the sub-kpc scale (P. R. Capelo et al. 2015). The dual quasars provide observational constraints on the initial conditions of sub-kpc SMBH pairs. Follow-up observations probing the ISM environment of the duals will shed light on the BH growth mechanism in such systems.

4 NOTES ON INDIVIDUAL SYSTEMS

For each observed system, we present a standardized 'Discovery Panel' to summarize the imaging and spectroscopic information. Fig. 3 illustrates the format using J000129.98 + 001911.3 as an example. From top to bottom, each panel contains:

(i) *HSC imaging. gri* colour-composite cutouts with side lengths of 60, 20, and 10 arcsec. On the 60 and 20 arcsec views, the spectroscopic slit is shown as a green rectangle, with its PA labelled in the upper right corner. The 10 arcsec cutout includes both angular and physical scale bars, indicating the separation between the two sources.

(ii) *2D spectrum.* The reduced 2D spectrum from PYPEIT (Section 2.3.1), displayed with wavelength along the horizontal axis and spatial direction along the slit on the vertical axis (both in pixels). The spectrum at the centre of the cutout always corresponds to the SDSS quasar, which is also the source at the centre of the image cutouts in panel (a), circled in red. The format varies by instrument: a single row for NTT/EFOSC2 and *Subaru*/FOCAS, three rows for Gemini/GMOS-N (corresponding to its three CCD chips), and five rows for Keck/NIRES (corresponding to its five echelle orders, ordered blue to red from top to bottom). The spectra are normalized with Z-scale and linear stretch (typically $v_{\rm min}$ = median-1.5σ, $v_{\rm max}$ = median$+3\sigma$), with minor adjustments applied in a few cases to enhance line visibility.

(iii) *1D spectra.* Extracted spectra of the known SDSS quasar (red) and the companion source (blue). We label the spectra with the relative location of the sources in the image (mostly by 'N'orth or 'S'outh, rarely by 'L'eft or 'R'ight). Grey shaded regions mark wavelengths affected by strong sky emission or absorption. The PYQSOFIT-estimated redshifts[4] of both sources are shown in the legend, along with vertical dashed lines marking the expected positions of key emission or absorption features. The spectra are flux-calibrated and rescaled to HSC CModel photometry to correct for slit loss; the photometric flux points are shown as star symbols. In high-contrast cases, one spectrum may be rescaled to facilitate comparison (e.g. 'N×2' indicates the companion spectrum has been multiplied by two).

(iv) *Line-fitting results.* For the confirmed dual quasars and quasar–SFG pairs, we show the best-fitting results from PYQSOFIT for the known SDSS quasar (left) and the companion source (right). The techniques of PYQSOFIT are detailed in Section 2.3.2. The top panels show the fitting of the entire spectra, composed of the continuum (orange curve), iron template (cyan curve), and emission lines (green for narrow lines, and red for broad lines). The wavelength ranges which are used for the continuum fitting are marked with the grey bars. The bottom panels

[4]They are generally similar to the SDSS redshifts as given in Table 1.

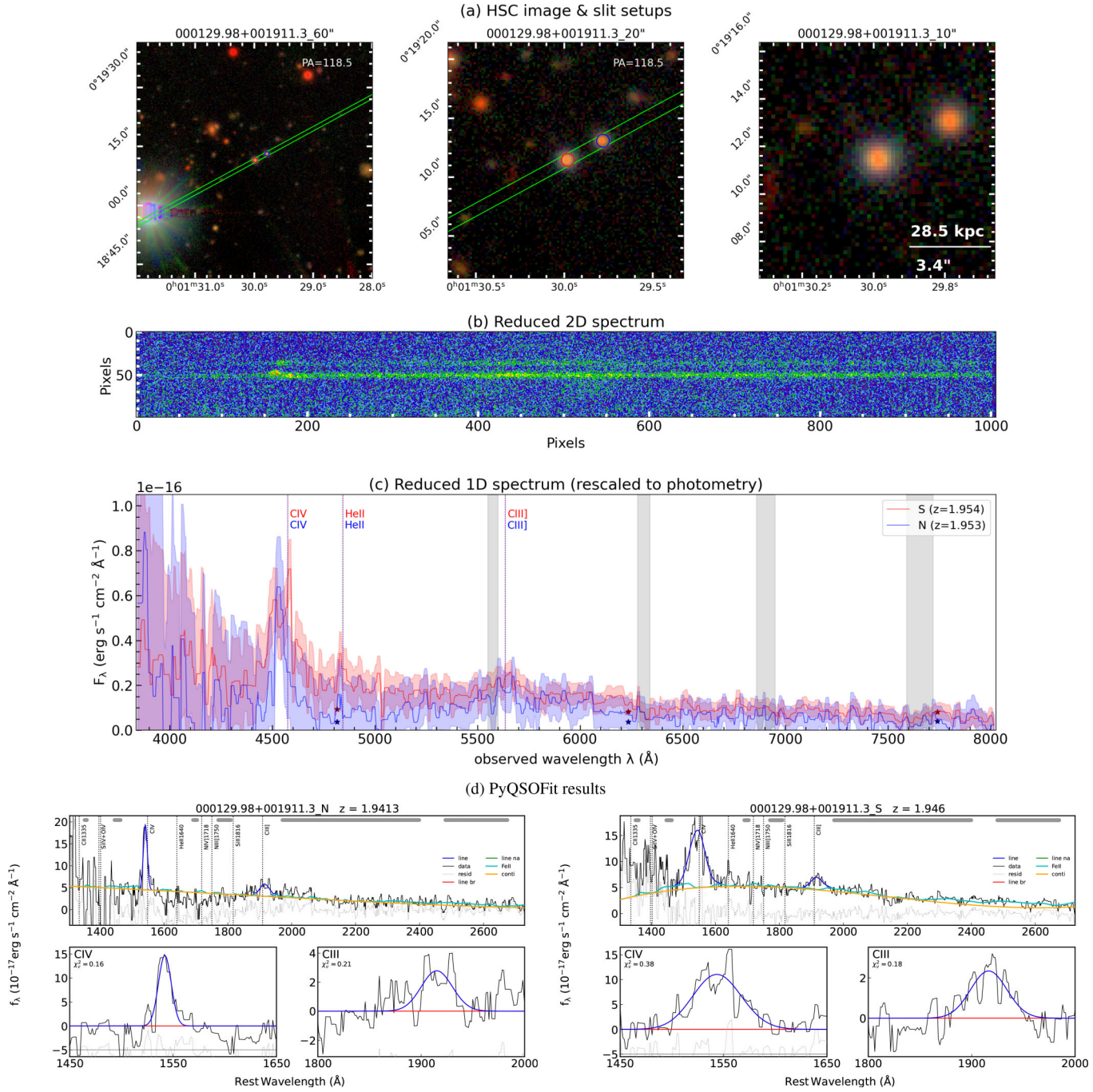

Figure 3. Example of a standardized 'Discovery Panel' for J000129.98 + 001911.3. Panel (a): HSC three-colour images with side lengths of 60, 20, and 10 arcsec, including slit orientation and source separation. Panel (b): PYPEIT-reduced 2D spectrum. The spectrum at the centre (50 pixels) corresponds to the SDSS quasar (source circled in red in panel a). Panel (c): 1D spectra of the SDSS quasar (source "S") and the companion source (source "N"), rescaled to HSC photometry. Panel (d): PYQSOFIT results for both 1D spectra. A detailed description of the Discovery Panel format is provided in Section 4. The full figure set for all systems analysed in this work is available as Supporting Information online.

show zoom-in views of the emission lines, after subtracting the continuum and iron emission. For the quasar–QG/LRG pairs, we show the fitting results of the absorption lines of the companion sources instead.

The complete set of Discovery Panels for all observed systems is available in the online Supporting Information associated with this article. The rest of those for the confirmed dual and offset quasars are presented in Appendix B. We encourage readers to use these figures as visual guides to the classifications presented below, and as resources for potential follow-up observations.

4.1 Dual quasars

In this section, we present six dual quasars with at least one broad emission line detected in both sources at the same redshift.

4.1.1 J000129.98 + 001911.3

This system was observed with NTT/EFOSC2 using the Gr no. 6 + CG375 setup with three exposures of 1000 s each (Fig. 3). The separation between the two sources is 3.4 arcsec, corresponding to a projected distance of 28.5 kpc. The southern component (J0001 + 0019S) is the known SDSS quasar. From its spectrum, we measure $z = 1.9474$.

In the spectrum of the northern source (J0001 + 0019N), we detect a 6.0σ broad emission line with FWHM = 2874 km s^{-1} at 4542 Å. Interpreting this feature as C IV λ1549 yields a redshift of $z = 1.9457$, which corresponds to a line-of-sight velocity offset of 64 km s^{-1} relative to the SDSS quasar. A tentative 2.1σ feature is also seen near the expected position of C III] λ1909, though with an unconstrained width (Table 7). An alternative interpretation of the 6.0σ line as Mg II λ2799 would imply a lower redshift of $z = 0.68$. However, in that scenario, additional strong lines ([Ne V], [O II], [Ne III], Hγ) should fall within our spectral coverage, none of which are detected. We therefore conclude that both components are most likely at the same redshift ($z \simeq 1.95$).

Next, we consider the lensing hypothesis. The flux ratio between the spectra of J0001+0019S and J0001 + 0019N is non-identical, varying between ∼1 and 3 across the observed wavelength range. Moreover, the C IV line profile of J0001+0019S is significantly broader than that of J0001 + 0019N, and shows a double-peaked feature which is unseen in the latter. Finally, no additional galaxies are detected within a 4 arcsec radius in the HSC imaging. Taken together, these factors argue against the lensing interpretation and favour the classification of this system as a dual quasar system.

4.1.2 J100547.80 + 013348.4

This system was observed with NTT/EFOSC2 using the Gr no. 6 + CG375 setup with three exposures of 1200 s each (Fig. B1). The two components are separated by 2.1 arcsec, corresponding to a projected distance of 17.5 kpc. The southern source (J1005 + 0133S) is the known SDSS quasar, for which we measure $z = 2.0551$.

In the spectrum of the northern source (J1005 + 0133N), we detect a 5.3σ broad emission line with FWHM = 5124 km s^{-1} at 4730 Å. This feature is best identified as C IV λ1549, yielding $z = 2.0525$, only 89 km s^{-1} offset from the SDSS quasar. While C III] λ1909 is not detected, we identify a $\sim 3\sigma$ emission feature at the expected wavelength of He II λ1640, consistent with the same redshift.

We also assess the lensing scenario. J1005+0133S appears slightly bluer than J1005 + 0133N, and the overall spectral flux ratio is ∼8 across the observed wavelength range. Moreover, C III] is clearly detected in J1005+0133S but absent in J1005 + 0133N, indicating intrinsic spectral differences between the two sources. Finally, the HSC imaging reveals no additional galaxies within a 10 arcsec radius. Taken together, these arguments strongly disfavor a lensing interpretation. We therefore classify J1005 + 0133 as a dual quasar system.

4.1.3 J123939.06 + 003439.8

This system was first observed with Gemini/GMOS-N using the R831 + OG515 grating centred at 860 nm, with three exposures of 847 s each (Fig. B2), and subsequently followed up with Keck/NIRES using four exposures of 300 s each (Fig. B3). The two components are separated by 1.7 arcsec, corresponding to a projected distance of 14.1 kpc. The southern source (J1239 + 0034S) is the known SDSS quasar, for which we measure $z = 2.1371$.

In the GMOS spectrum of the northern source (J1239 + 0034N), we detect a tentative 2.3σ broad emission line at 5975 Å with FWHM = 6712 km s^{-1}, most consistent with Mg II λ2799. To verify this identification, we obtained follow-up NIRES spectroscopy. The NIRES data reveal a 2.6σ broad Hβ emission line (FWHM = 16950 km s^{-1}) and a strong 5.0σ broad Hα emission line (FWHM = 8093 km s^{-1}) at the corresponding redshift. From these lines, we determine $z = 2.1338$ for J1239 + 0034N, implying a velocity offset of 106 km s^{-1} relative to the SDSS quasar.

The continua of the two sources are nearly identical in color, with a flux ratio of ∼10. However, their emission-line properties differ: Hβ is significantly stronger in J1239+0034S than in J1239 + 0034N relative to Hα, indicating intrinsic differences between the quasars. In the HSC imaging, a faint galaxy ($i \simeq 22$, $y \simeq 22$) lies 4.7 arcsec from J1239 + 0034S at PA = −138°. Given its faintness and projected separation, as well as the spectral differences between the two quasars, it is unlikely to act as a lensing galaxy. We therefore classify J1239 + 0034 as a dual quasar system.

4.1.4 J145201.59−011945.3

This system was observed with Gemini/GMOS-N using the R831 + OG515 grating centred at 800 nm, with three exposures of 600 s each (Fig. B4). The two components are separated by 2.6 arcsec, corresponding to a projected distance of 21.9 kpc. The northern source (J1452−0119N) is the known SDSS quasar, for which we measure $z = 1.8753$.

In the spectrum of the southern source (J1452−0119S), we detect a 6.9σ broad emission line at 8044 Å with FWHM = 3339 km s^{-1}. This feature is best identified as Mg II λ2799, from which we determined $z = 1.8755$, with almost no line-of-sight velocity offset from the SDSS quasar. No additional emission lines are detected between 7000–9000 Å, but the iron emission template provides a good fit under this redshift assumption.

The two sources exhibit nearly identical optical colours, with an overall flux ratio of ∼5. The HSC imaging shows no additional galaxy brighter than $i = 23$ within 5 arcsec of the pair. Given the consistent redshift interpretation and the absence of a potential lensing galaxy, we classify J1452−0119 as a dual quasar system.

4.1.5 J231854.69−012725.9

This system was observed with NTT/EFOSC2 using the Gr no. 6 + CG375 setup with 3×1000 s exposure (Fig. B5) and subsequently followed up with *Subaru*/FOCAS with 2×1200 s exposure (Fig. B6). The two components are separated by 3.8 arcsec, corresponding to a projected distance of 31.1 kpc. The northern source (J2318−0127N) is the known SDSS quasar, for which we measure $z = 2.3369$.

In the combined EFOSC2 + FOCAS spectrum of the southern source (J2318−0127S), we detect broad C IV, C III], and Mg II emission lines at the same wavelengths as in J2318−0127N, each with significance $\gtrsim 4\sigma$. From these lines, we estimate $z = 2.3461$, corresponding to a velocity offset of 239 km s^{-1} relative to the SDSS quasar.

The two quasars exhibit nearly identical optical colors with an overall flux ratio of ∼2. In the HSC imaging, a third red source lies ∼ 4 arcsec south of the primary quasar. However, this object is classified as a point source in all five HSC bands (based on the extendedness flag in the forced photometry catalogue), and is therefore most likely a foreground star rather than a lensing galaxy. Moreover, the spectrum of J2318−0127S shows narrow absorption features superimposed on the C IV and C III] emission lines that are not present in J2318−0127N. These intrinsic differences further disfavor a lensing interpretation. We therefore classify J2318−0127 as a dual quasar system.

4.1.6 J233225.33 + 000042.5

This system was observed with Gemini/GMOS-N using the B600 + CG455 setup centred at 630 nm, with 600 s × 12 exposures (Fig. B7). The two sources are separated by 2.3 arcsec, corresponding to a projected distance of 17.3 kpc. The southern source (J2332 + 0000S) is the known SDSS quasar, for which we measure $z = 3.2649$. Its spectrum shows a strong Lyα emission line. In the northern source (J2332 + 0000N), Lyα is detected at $\sim 3\sigma$ at a consistent wavelength, and a tentative C IV line is seen at $\sim 2\sigma$. From these features we estimate $z = 3.2706$ for J2332 + 0000N, corresponding to a velocity offset of 79 km s^{-1} from the SDSS quasar.

The continuum flux ratio of the two quasars is ∼5, while their Lyα flux ratio is significantly higher (∼14). In the HSC imaging, the only additional bright source in the vicinity is a red point-like object located ∼5 arcsec from J2332 + 0000S, consistent with a foreground star rather than a lensing galaxy. Combined with the spectral differences between the two sources, we therefore classify this system as a dual quasar rather than a lensed quasar.

Interestingly, both quasars in this system exhibit narrow C IV absorption lines superimposed on their C IV emission. Narrow, associated absorbers of this kind are common in quasar spectra (e.g. M. Vestergaard 2003; F. Hamann et al. 2011), and may originate from gas inflows, circumnuclear material, or the larger scale circumgalactic medium (CGM). At face value, the absorbers in J2332 + 0000 appear slightly redshifted relative to the C IV emission peaks, which could be interpreted as evidence for inflow. The close similarity of the absorption profiles in both quasars suggests that the absorber may spans at least 17 kpc and may trace shared halo gas. Coherent metal-line absorbers are reported with up to 200 kpc from the centre (e.g. M. Landoni et al. 2016), supporting an interpretation in terms of enriched CGM associated with the merging system.

In summary, J2332 + 0000 is a dual quasar system at $z \sim 3.27$, and its shared narrow absorption features make it a particularly compelling laboratory for studying the interplay between quasar activity and the CGM in merging environments.

4.2 Offset quasars

In this section, we describe the offset quasars where the companion to the SDSS quasar is identified as a paired galaxy without significant broad emission-line detection. The companion spectra are classified either as SFGs, based on the presence of narrow emission lines, or as QGs and LRG, when dominated by absorption features.

4.2.1 J010123.64 + 010045.3

This system, at $z = 0.275$, was observed with NTT/EFOSC2 using the Gr no. 5 grism for three exposures of 800 s each (Fig. B8). The angular separation between the two sources is 2.7 arcsec, corresponding to a projected physical distance of 11.3 kpc. The southern source of the pair is the known SDSS quasar.

The companion source is brighter in the continuum, with a quasar-to-companion flux ratio of ∼ 0.5. Its spectrum shows significant Mg I λ5176.7 and Na λ5895.6 absorption features at the same redshift as the quasar (bottom panels of Fig. B8). Furthermore, the continuum shape does not match any stellar template in the SDSS library, while well reproduced by the LRG template redshifted to $z = 0.275$. We therefore classify this system as a quasar–LRG pair.

4.2.2 J092919.16 + 041414.2

This system, at $z = 0.37$, was observed with Gemini/GMOS-N using the B600+CG455 grating centred at 680 nm. It is at least a triple system, consisting of a quasar flanked by two elliptical galaxies and connected by a curved optical feature. We refer to the quasar as J0929+0414A, the brighter southern galaxy as J0929+0414B, and the fainter western galaxy as J0929 + 0414C. The projected separations are 2.1 arcsec (10.8 kpc) between A and B, and 1.6 arcsec (8.2 kpc) between A and C.

We obtained two sets of spectra, each with 3 × 300 s exposures, at PAs of 143.2° (Fig. B9) and 74.7° (Fig. B10) to cover the quasar with either galaxy. Because of the complex morphology, HSC photometry rescaling is not applied. From the flux-calibrated spectra, the continuum flux ratios are ∼2 (A/B) and ∼5 (A/C). Both J0929+0414B and J0929 + 0414C show absorption features typical of old stellar populations at the same redshift as the quasar: Ca H&K λλ3934.8, 3969.6, the *G*-band λ4305.6, and Mg I λ5176.7. The *G*-band absorption is also evident in the quasar spectrum, confirming its association with the same galaxy group. The two galaxies have nearly identical spectra, but given that they share the quasar's redshift, they cannot be lens images. We therefore classify this system as a quasar–QG–QG triple system.

Intriguingly, the HSC imaging reveals an arc-like structure northeast of the quasar. The J0929 + 0414A spectrum obtained at PA = 74.7° is ∼60 per cent brighter than that at PA = 143.2°, likely due to partial slit coverage of this arc. The morphology resembles shock fronts seen in nearby interacting galaxies (e.g. M. Rodríguez-Baras et al. 2014), suggestive of tidal debris or merger-driven gas compression. Alternatively, the feature could represent a lensed background galaxy, which cannot be ruled out without deeper spectroscopy or higher resolution imaging.

Comparable systems have been recently discovered at higher redshift, such as the remarkable double-ringed merging galaxy at $z = 1.14$ identified in the COSMOS field with *James Webb Space Telescope* (*JWST*, P. Dokkum et al. 2025; M. Li et al. 2026), where the central AGN appears offset within the merger structure. J0929 + 0414 may serve as a rare low-redshift analogue to test scenarios of merger-driven AGN triggering and the role of gas inflows in shaping SMBH growth. Motivated by its appearance in HSC images, we assign this system the nickname of the 'clown' galaxy.

4.2.3 J100701.56 + 052315.4

This system, at $z = 0.539$, was observed with Gemini/GMOS-N using the B600 + CG455 grating centred at 680 nm, with

3 × 600 s exposures (Fig. B11). The two sources are separated by 2.2 arcsec, corresponding to 14.0 kpc. The southern source is the known SDSS quasar. The continuum flux ratio between the quasar and its companion decreases from ∼18 at 5300 Å to ∼3 at 8000 Å, indicating that the companion is relatively red. The spectrum of the companion shows clear Ca II H&K absorption and weak *G*-band absorption at the same redshift as the quasar, while no Balmer, [O II], or [O III] emission lines are detected. We therefore classify this system as a quasar–QG pair.

4.2.4 J110556.18 + 031243.1

This system, at $z = 0.354$, was observed with NTT/EFOSC2 using Gr no. 5 with 3 × 300 s exposures (Fig. B12). The projected separation between the two sources is 2.4 arcsec (11.9 kpc). The northern source is the known SDSS quasar. The continuum flux ratio between the quasar and its companion is ∼1.5, although the 2D spectrum of the companion appears fainter than expected, likely due to a slight slit mis-centring. The companion spectrum exhibits narrow Hα and [N II] emission lines with FWHM ≈ 15 Å (∼685 km s^{-1}) at $z = 0.356$. Ca II H&K absorption lines are also found at this redshift. Other expected features, including Hγ, Hβ, and [O III], are covered by our spectral setup but remain undetected. Therefore, this galaxy is likely made up of a mixed population of young and old stars. We classify this system as a quasar–SFG/QG pair.

4.2.5 J112753.39−020142.7

This system was observed with NTT/EFOSC2 using Gr no. 6 + CG375 with 3 × 1200 s exposures (Fig. B13) and subsequently followed up using Keck/NIRES with 4 × 300 s exposures (Fig. B14). The two sources are separated by 3.2 arcsec, corresponding to a projected distance of 26.3 kpc. The northern source is the known SDSS quasar, for which we measure $z = 2.2867$. The two objects show nearly identical colours in HSC imaging, with a continuum flux ratio of ∼3.

In the NIRES spectrum of the southern source (J1127−0201S), we detect a strong ($\sim 6\sigma$) emission line at ∼ 2.187 μm with FWHM = 13.6 Å (∼619 km s^{-1}). Interpreting this feature as Hα yields $z = 2.2924$, corresponding to a velocity offset of 161 km s^{-1} relative to the SDSS quasar. A tentative broad C III] emission feature is also present in the NTT spectrum at the same redshift. However, other key lines expected at this redshift, including C IV, Hβ, and [O III], are not detected despite being within the observed wavelength coverage.

We also considered alternative identifications of the 2.187 μm feature. If interpreted as Hβ, the implied redshift would be $z \sim 3.5$, which should place Lyα in the optical spectrum obtained with NTT. However, no Lyα emission is observed at the expected wavelength, disfavouring this scenario.

The line width of the putative Hα emission (∼ 600 km s^{-1}) is broader than typically seen in pure SFGs, where nebular recombination lines generally exhibit FWHM $\lesssim$ 200–300 km s^{-1} (e.g. N. F. Schreiber et al. 2018). Also given the tentative broad C III] detection, this suggests that the companion could host a narrow-line AGN (type 2) or a composite SFG + AGN. We therefore classify this system as a quasar–SFG pair, with the companion possibly hosting a narrow-line AGN.

4.2.6 J121745.76 + 022109.5

This system is at $z = 0.28$, observed using NTT/EFOSC2 Gr no. 5 with 3 × 800 s exposures (Fig. B15). The two sources are separated by 3.0 arcsec, corresponding to a projected distance of 12.7 kpc. The southern source is the known SDSS quasar. The continuum flux ratio between the quasar and its companion decreases from ∼20 at 5500 Å to ∼10 at 9000 Å, indicating that the companion becomes relatively redder toward longer wavelengths.

The companion spectrum shows clear narrow Hα and [N II] emission lines, with FWHM ≃ 12 Å (∼529 km s^{-1}) at $z = 0.281$. The [O III] and Hβ lines are also within the spectral coverage, but only tentatively detected with peak fluxes of $F_\lambda \simeq 2 \times 10^{-18}$ erg s^{-1} cm^{-2} Å^{-1}. Weak Mg I λ5176.7 and Na I λ5895.6 absorptions are also found at corresponding wavelengths, suggesting a mixed old and young stellar population of this galaxy.

Both the [N II]/Hα and [O III]/Hβ ratios of the companion are close to unity. This places the source in the composite region of the standard BPT diagram (J. A. Baldwin, M. M. Phillips & R. Terlevich 1981). The relatively narrow-line widths (∼500 km s^{-1}) are broader than expected for pure H II regions but consistent with ionized gas in galaxies hosting weak or obscured AGN (e.g. R. C. Fernandes et al. 2010).

We therefore classify this system as a quasar–SFG/QG pair, with the companion likely being a composite system where both star formation and AGN contribute to the ionization.

4.2.7 J122349.29 + 021449.1

This system is at $z = 0.408$, observed using Gemini/GMOS-N B600 + CG455 with 3 × 600 s exposures, centred at 680 nm (Fig. B16). The separation between the two sources is 2.4 arcsec, corresponding to a projected distance of 13.1 kpc. The northern source is the known SDSS quasar. The quasar and the companion have similar colors in HSC imaging. Because the photometry of this system is unreliable, we did not apply photometric rescaling to the spectrum. From the Gemini data, we measure a continuum flux ratio of ∼3 between the quasar and the companion, although the true ratio is likely higher given that the slit was slightly offset from the companion.

The companion spectrum shows Ca II H&K and *G*-band absorption features at the same redshift as the quasar (Fig. B16). The continuum slope matches with the SDSS galaxy template at this redshift. No additional emission features are securely detected. We therefore classify this system as a quasar–QG pair.

Interestingly, the quasar itself exhibits strong spectral variability. The original SDSS spectrum taken at MJD = 52283 shows prominent broad Balmer emission lines. In contrast, the later Gemini/GMOS-N spectrum (MJD = 59295) reveals only narrow emission lines, with the broad components having disappeared. This dramatic transition identifies the quasar as a changing-look AGN, with the accretion state changes probably driven by disc instabilities and/or variations in accretion rate (e.g. C. Ricci & B. Trakhtenbrot 2023).

4.2.8 J125156.49 + 015249.7

This system is at $z = 0.33$, observed with Gemini/GMOS-N B600 + CG455 centred at 630 nm with 600 s×3 exposures (Fig. B17).

The separation between the two sources is 1.5 arcsec, which corresponds to 7.1 kpc. The southern source of the pair is the known SDSS quasar. The continuum flux ratio between the quasar and the companion source is ∼7. The companion spectrum shows solid detections of the [O II] and [O III] lines at the same redshift as the quasar, while the position of the Hβ line rather shows a weak absorption. The blue side of the spectrum shows Ca II H&K doublet absorption and the other Fraunhofer-like absorption features. The tidal features in the HSC image indicates that this system is in a late merger stage. Considering these evidences, we consider two possible scenarios for the companion source: (1) it is under a transition stage from star formation galaxy to post-starburst galaxy. It has little or no ongoing star formation but with some residual ionized gas ([O II] and [O III]) – possibly excited by evolved stars or shocks. (2) It is a QG, and the gas is ionized by an obscured AGN. Therefore, we classify this system a bona fide physical pair, with the ionization source of the companion to be confirmed. Therefore, we suggest the companion source a quiescent or post-starburst galaxy, and the [O III] line indicates a potential obscured AGN residing in it.

4.2.9 J130550.51−012331.5

This system is at $z = 0.251$, observed with Gemini/GMOS-N B600 + CG455 centred at 630 nm with 600 s×3 exposures (Fig. B18). The separation between the two sources is 1.3 arcsec, which corresponds to 5.1 kpc. The northern source of the pair is the known SDSS quasar. The continuum ratio between the quasar and the companion source reduces from ∼27 at ∼4800 Å to ∼6 at ∼7500 Å. An intriguing feature of this system is the extremely extended [O III] emission line. As shown in the 2D spectrum, the [O III] line-emitting region spatially extends beyond the two nuclei, reaching the outskirts of the galaxies. This feature is more extended from the quasar to the companion side than to the opposite side. In addition to the [O III] doublet, the Hβ line is also extended on both sides, but less obviously. The physical mechanisms attributed to this kind of extended emission-line region (EELR) are still uncertain. Recent Intergal Field Unit (IFU) studies reported geometric connections between EELRs and radio emissions, indicating connections with the AGN feedback effect (B. Balmaverde et al. 2022). When following the reduction steps (Section 2.3.1), we extract the spectrum along the spatial axis at the position of the [O III] λ5007 line peak, which can be fit with two separate Gaussian profiles. Therefore, we suggest that the companion source also contributes to the EELR, and this system is a quasar–SFG pair.

Furthermore, the SDSS quasar in the pair is also a potential changing-look AGN. In our observation (MJD = 59319), the broad Hβ line still exists, with FWHM = 7431 Å, EW = 66 Å, and SNR = 6.5. However, the narrow Hβ becomes much weaker than in the SDSS spectrum (observed at MJD = 51692).

4.2.10 J134722.75 + 015504.9

This system lies at $z = 0.399$ and was observed with NTT/EFOSC2 using Gr no. 5 with three ×600 s exposures (Fig. B19). The projected separation between the two sources is 1.9 arcsec (10.2 kpc). The southern source is the known SDSS quasar. The continuum flux ratio between the quasar and the companion decreases from ∼15 at ∼5500 Å to ∼8 at ∼9000 Å. The companion spectrum shows tentative absorption features, including Ca II H&K and Mg I, at a redshift consistent with the quasar, but no emission lines are detected. HSC imaging reveals tidal features connecting the quasar and the companion, supporting an interacting system. We therefore classify J1347 + 0155 as a quasar–QG pair.

4.2.11 J222327.52 + 033902.0

This system lies at $z = 0.35$ and was observed with Gemini/GMOS-N using the B600 + CG455 grating centred at 630 nm, with three ×600 s exposures (Fig. B20). The projected separation is 2.7 arcsec (13.3 kpc). The southern source is the known SDSS quasar. The continuum flux ratio between the quasar and its companion is ∼3. The companion spectrum shows narrow [O II], Hγ, Hβ, and [O III] emission lines at the same redshift as the quasar. We measure FWHM values of 286 km s^{-1} for [O III] and Hβ, and 467 km s^{-1} for [O II]. The line ratio [O III]/Hβ is 2.6.

Because the spectrum does not cover Hα and [N II], we cannot apply the classical BPT diagram (J. A. Baldwin et al. 1981). Alternatively, we use the R_{23} (([O II] λ3727 + [O III] λλ4959, 5007)/Hβ, B. Pagel et al. 1979; L. J. Kewley & M. A. Dopita 2002) and O_{32} ratio ([O III] λλ4959, 5007)/[O II] λ3727, L. J. Kewley & M. A. Dopita 2002) diagnostics, which are sensitive to the ionization parameter and gas-phase metallicity. Assuming the emission originates purely from star formation, we find $\log R_{23} = 0.92$ and $\log O_{32} = -0.13$. These values correspond to an intermediate metallicity ($12 + \log(\mathrm{O/H}) \sim 8.4$) typical of SDSS SFGs (K. Nakajima & M. Ouchi 2014; M. Curti et al. 2016). Using the diagnostic diagrams of L. J. Kewley & M. A. Dopita (2002), we estimate an ionization parameter of $\log(q_{\rm ion}/\mathrm{cm\,s^{-1}}) \sim 7.4$, intermediate between local ($z < 0.3$) SDSS galaxies and $z \sim 1$ galaxies (K. Nakajima & M. Ouchi 2014). The ionization state of the companion is thus consistent with star formation activity. We therefore classify J2223 + 0339 as a quasar–SFG pair.

5 DISCUSSION

Combining the 90 newly observed candidates in this work with 32 followed up by J. D. Silverman et al. (2020) and S. Tang et al. (2021), we have now obtained spectroscopic data for 122 dual candidates. Among them, we confirm 12 broad-line dual quasars and 14 quasar–galaxy pairs. The overall classification status of our program is summarized in Fig. 4. From left to right, the panels show the redshift distribution, angular separation between the two point sources in each candidate pair, the *i*-band PSF magnitude of the companion source, and the *i*-band magnitude difference between the SDSS quasar and its companion. The grey histograms represent 96 projected systems where the two components lie at different redshifts. The pink histograms denote 14 unclassified cases, mostly due to blending or insufficient S/N. The green and yellow bars correspond to the 12 confirmed quasar pairs and 14 quasar–galaxy pairs, respectively. The remainder of the sample, totaling 761 systems, remains unobserved. We further divide these by companion colour into 212 'blue' candidates ($g - r < 1$) and 548 'red' candidates ($g - r > 1$), shown as the blue and red histograms in Fig. 4.

Based on these statistics, in this section we first attempt to estimate the dual fraction at different redshifts, and then discuss the caveats of our selection.

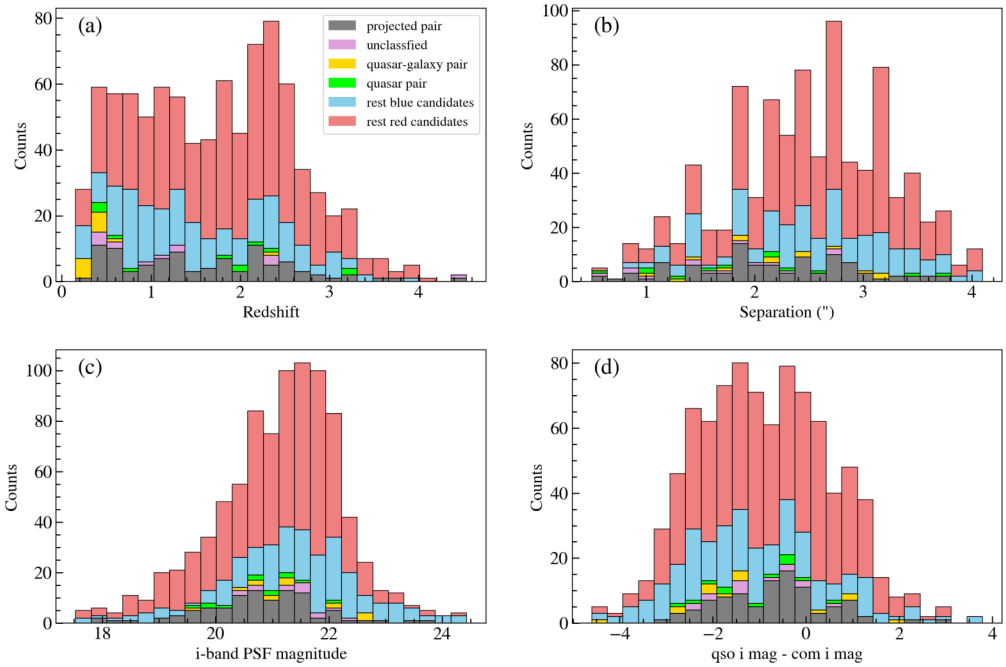

Figure 4. Classification outcomes of our dual quasar survey as a function of (a) redshift, (b) angular separation, (c) *i*-band PSF magnitude of the companion, and (d) *i*-band magnitude difference between the SDSS quasar and the companion. A total number of 122 systems have been observed among 883 dual candidates. Grey histograms denote projected pairs (96 systems where the two components are at different redshifts), pink histograms show unclassified cases (14 systems, mostly due to blending or low S/N), green and yellow histograms correspond to confirmed broad-line dual quasars (12) and quasar–galaxy pairs (14), respectively. The blue and red histograms represent unobserved candidates with companion colour $g - r < 1$ (212 systems) and $g - r > 1$ (548 systems).

5.1 Dual fraction

The redshift distribution of our candidate list (Fig. 4 panel a) closely follows that of the SDSS DR14 quasar catalogue (I. Pâris et al. 2018). Our confirmed dual quasars span $0.4 < z < 3.3$, while the majority (13/14) of quasar–galaxy pairs are found at $z < 0.6$. This is consistent with the well-established cosmic downsizing trend in AGN evolution: luminous quasars peak at $z \sim 2$–3 and decline toward lower redshift, while Seyfert-like, moderate-luminosity AGN dominate below $z \lesssim 1$ (e.g. N. Fanidakis et al. 2012). These quasar–galaxy systems likely represent mergers hosting two SMBHs in different accretion states, where the companion galaxy shows a point-source morphology but lacks broad emission lines. Such cases may still harbor obscured or low-luminosity AGN, detectable through multi-wavelength diagnostics (e.g. radio jets, hard X-rays, or mid-IR dust emission; R. C. Hickox & D. M. Alexander 2018). A key caveat is that our selection requires one known SDSS quasar in each pair, inherently biasing the sample toward luminous broad-line AGN and making us incomplete for the low-z population where most AGN are not SDSS quasars (T. M. Heckman & P. N. Best 2014).

Bearing that caveat in mind, we estimate the dual fraction specifically for SDSS quasars in three redshift ranges. At $z < 0.6$, the observed ratio between dual quasars and quasar–galaxy pairs (3:13) indicates that only ∼20 per cent of (major) merging systems hosting an SDSS quasar also harbour a companion with detectable broad emission lines. According to our cross-match (Section 2.1), there are 59 482 SDSS DR14 quasars imaged in the HSC-SSP s20a_wide release, of which 2672 lie at $z < 0.6$. Among these, 113 are selected as dual candidates, comprising 47 'blue' companions ($g - r < 1$) and 65 'red' companions ($g - r > 1$). Our three confirmed dual quasars at $z < 0.6$ (indeed, all confirmed duals in this work) fall into the blue category. They were discovered from 20 observed blue candidates, corresponding to a blue-candidate success rate of ∼15 per cent. If we conservatively assume that all 51 red candidates are not broad-line quasars and that the unobserved 27 blue candidates share the same success rate, the expected total number of dual quasars at $z < 0.6$ is ∼7, yielding a dual fraction of 0.3 per cent (7/2672) for SDSS quasars with separations of 0.6–4 arcsec. A more inclusive estimate comes from considering the quasar–galaxy pairs, which may host obscured or moderate-luminosity AGN. Among the observed sample, 6 such systems are identified from 20 blue candidates (30 per cent) and 7 from 14 red candidates (50 per cent). Extrapolating these rates to the unobserved candidates implies a total of ∼53.7 dual systems (quasar pairs + quasar–galaxy pairs), corresponding to an upper limit of ∼2.0 per cent (53.7/2672). We therefore report a dual fraction of 0.3 per cent–2.0 per cent for SDSS quasars at $z < 0.6$ with separations of 0.6–4 arcsec. Extending the redshift range to $z < 0.8$ adds two confirmed dual quasars and increases the parent SDSS×HSC sample to 6351 objects; following the same procedure yields a dual fraction of 0.2 per cent–1.2 per cent at $z < 0.8$. These low-redshift results are consistent with previous work (J. D. Silverman et al. 2020) and with simulations predicting that only a small fraction of merging SMBHs are simultaneously luminous broad-line AGN at low z (L. K. Steinborn et al. 2016; Y. M. Rosas-Guevara et al. 2019; M. Volonteri et al. 2022).

In the intermediate bin, $0.8 < z < 1.5$, we have not yet confirmed any dual quasars or quasar–galaxy pairs among 14 594 SDSS×HSC quasars. Adopting the $z < 0.8$ blue-candidate success rate (5/28) as a conservative proxy and rejecting red candidates, the implied dual fraction is 0.08 per cent. If we additionally assume that the fraction of quasar–galaxy pairs among blue and

red candidates (6/28 and 7/84, respectively) persists in this bin and that such companions host moderate-luminosity AGN, the corresponding upper limit fraction is 0.24 per cent. We therefore report a dual fraction of 0.08 per cent–0.24 per cent for SDSS quasars at $0.8 < z < 1.5$.

At cosmic noon ($1.5 < z < 3.3$), we confirm 7 dual quasars and 1 quasar–galaxy pair among 52 observed candidates. Of the 52 candidates, 46 are blue, and all confirmed systems are blue, giving a blue-candidate success rate of ∼15 per cent (7/46). Rejecting red candidates and extending this rate to the unobserved blue candidates yields an expected total of 21.3 dual quasars (or 24.3 systems including the quasar–galaxy pair), corresponding to a dual fraction of 0.06 per cent (21.3/36 527–24.3/36 527) for SDSS quasars at $1.5 < z < 3.3$. Recently, Y. Shen et al. (2023) reported an integrated dual fraction of 0.062 ± 0.005 per cent for SDSS DR16 quasars selected with *Gaia*, at 0.3–3 arcsec separation and $1.5 < z < 3.5$. Although their methodology (astrometric selection with proper-motion filtering) differs from ours, our estimates are consistent with their results at cosmic noon.

Theoretical models and simulations generally predict that the dual AGN fraction increases with redshift, reaching values of a few per cent at cosmic noon, driven by the higher galaxy merger rate, elevated gas fractions, and longer quasar duty cycles at earlier cosmic times (e.g. L. K. Steinborn et al. 2016; P. R. Capelo et al. 2017; Y. M. Rosas-Guevara et al. 2019; M. Volonteri et al. 2022; N. Chen et al. 2023). In contrast, our observational results indicate an apparent decline in the dual fraction, from 0.3–2 per cent at $z < 0.6$ to only 0.06 per cent at $1.5 < z < 3.3$.

M. Volonteri et al. (2022) explored the impact of observational selection effects on the redshift evolution of the simulated dual fraction. Applying selection criteria of $\log L_{\rm bol} > 44$, $d < 30$ kpc, $\log(M_{\rm BH,1}/{\rm M}_\odot) > 7$, and $\log(M_{\rm BH,2}/{\rm M}_\odot) > 7$ – which best match the properties of our confirmed dual quasars (Fig. 2) – their simulations predict a dual fraction of 1.4 per cent at $z < 0.6$, rising to 2.5 per cent by $z \approx 2$ and remaining approximately constant at higher redshift (see their fig. 16).

The discrepancy between our observations and M. Volonteri et al. (2022) emerges at $z \gtrsim 0.6$, and likely has multiple contributing causes. First, our observed dual systems are required to include at least one SDSS-selected quasar, biasing the sample toward luminous, unobscured broad-line AGN. As demonstrated by our low-redshift results, a significant population of offset or dual systems may host companions without detectable broad emission lines. Consequently, a potentially large population of obscured–unobscured and obscured–obscured dual quasars is likely missed at high redshift. Second, a substantial fraction of the $1.5 < z < 3.3$ interval falls within the so-called redshift desert, where the lack of strong emission lines in the wavelength coverage of ground-based optical and near-infrared spectroscopy substantially hampers spectroscopic identification. Third, our selection does not distinguish dual AGN systems from triple or more AGN systems, which were treated separately in M. Volonteri et al. (2022). We expect this effect to be minor, however, since the number density of multiple-AGN systems in the simulation is approximately one order of magnitude lower than that of dual AGNs. Fourth, the rarity of luminous quasars in current cosmological simulations, owing to their limited volumes, leads to small-number statistics in the simulated dual-quasar population, further contributing to the apparent tension.

5.2 Selection effects and observational limitations

In addition to the redshift dependence and the bias to the unobscured bright sources discussed above, the candidate selection of our program is also shaped by observational constraints tied to angular separation, *i*-band PSF magnitude of the companion, and the *i*-band magnitude contrast between the pair, as shown by the remaining three panels of Fig. 4.

By construction, our candidate selection requires two distinct point sources in HSC imaging, with separations between 0.6 and 4 arcsec (Section 2.1). This lower limit is set by the seeing, below which reliable deblending becomes challenging in ground-based data. As shown in Fig. 4, the number of selected candidates rises toward larger separations. This is partly a geometric effect: the probability of finding a projected neighbour scales with the surface density of background sources and the area of the search annulus, πr^2, so wider search radii naturally yield more chance associations. At the smallest separations (< 2 arcsec), the available area is small, and the number of random alignments is correspondingly reduced. In addition, PSF blending at < 1 arcsec further suppresses completeness by making it difficult to reliably deblend companions from the bright SDSS quasar. These combined effects explain the relative paucity of selected candidates at close separations, despite theoretical expectations that the intrinsic dual fraction should increase at small physical scales during the final stages of SMBH inspiral (e.g. P. R. Capelo et al. 2017). Yet our spectroscopic follow-ups are still fairly effective in confirming the pairs both at separations above 2 arcsec (14/70=20 per cent), and below (12/52 = 23 per cent). In Q. Wang et al. (2026), we have tuned the selection method to push the separations of the candidates to < 0.6 arcsec (sub-5 kpc) with HSC, which are then followed up with *Hubble Space Telescope* (*HST*) grism spectroscopy.

Our selection also required a reliable HSC *i*-band PSF measurement for the companion source. As shown in Fig. 4 panel (c), the confirmed dual quasars predominantly occupy the bright regime ($i < 22.5$), while fainter companions are more often classified as quasar–galaxy pairs or remain unclassified due to insufficient S/N in the spectroscopy. The total number of selected dual candidates also decreases at the faint end. This also reflects the limitations of our source selection method. Our GALIGHT-based selection relies on the `photutils.detect_sources` function to identify multiple point sources in HSC images (X. Ding et al. 2022), which becomes increasingly inefficient when the two components differ strongly in brightness (L. Bradley et al. 2024). In practice, this sets a contrast limit of $\Delta i \lesssim 3$[as most of the candidates are distributed in panel (d) of Fig. 4], beyond which faint companions are not reliably deblended from the bright SDSS quasar. As a result, this restricts us to nearly equal-luminosity pairs, thus major mergers.

Taken together, these considerations highlight that our selection method and dual fraction estimates apply only to a restricted parameter space: separations of 0.6–4 arcsec, companion magnitudes of $i \lesssim 22.5$, and modest luminosity contrasts. Expanding beyond this regime will require higher resolution imaging, e.g. with *JWST* (J. Li, M.-Y. Zhuang & Y. Shen 2024; J. Li et al. 2025) and *Euclid* (L. Ulivi et al. 2025), and deeper spectroscopy to probe fainter and more unequal pairs (e.g. Y. Matsuoka et al. 2024; M. Perna et al. 2025, 2026). Multiwavelength approaches, such as with X-ray, will also be essential for confirming and recovering missed obscured dual AGNs (e.g. A. De Rosa et al. 2023).

6 CONCLUSIONS

We have carried out a spectroscopic follow-up program targeting 90 dual quasar candidates selected from *Subaru* HSC-SSP imaging of SDSS DR14 quasars. Our selection is based on 2D image decomposition and identifies PSF-like companions within 0.6–4 arcsec ($\lesssim$ 30 kpc) of an SDSS quasar. From the spectra obtained with NTT/EFOSC2, Gemini/GMOS-N, Keck/NIRES, and *Subaru*/FOCAS, we draw the following conclusions:

(i) We newly confirm six broad-line dual quasars and eleven offset quasars (quasar–galaxy pairs). Taken together with our previous work, our program has now identified 12 dual quasars and 14 offset quasars. The dual quasars span $1.5 < z < 3.3$, while most quasar–galaxy pairs are found at $z < 0.6$.

(ii) For the confirmed duals at $z > 1.5$, emission-line measurements yield BH masses of $M_{\rm BH} = 10^{8.5}$–10^{10} $M_\odot$ and bolometric luminosities of $L_{\rm bol} = 10^{45.5}$–$10^{47.5}$ erg s^{-1}. Their Eddington ratios are moderate ($\lambda_{\rm Edd} = 0.01$–0.4), indicating that while mergers can ignite both nuclei, simultaneous near-Eddington fuelling is not required.

(iii) At $z < 0.6$, our spectroscopic identifications are dominated by offset quasars, where the companion exhibits a point-like morphology but no broad emission lines. These systems likely host moderate-luminosity or obscured AGN, consistent with the downsizing trend in which Seyfert-like activity dominates at late cosmic times. The elevated fraction of offset quasars at low redshift highlights the low duty cycle of quasar activity in mergers.

(iv) Using the full SDSS DR14Q×HSC s20a_wide quasar sample, we estimate the dual fraction of SDSS quasars within 0.6–4 arcsec separation to be 0.2 per cent–1.2 per cent at $z < 0.8$, 0.08 per cent–0.24 per cent at $0.8 < z < 1.5$, and 0.06 per cent at $1.5 < z < 3.3$. The lower values only consider quasar-quasar pairs, and the upper values include quasar–galaxy pairs. These observed fractions are broadly consistent with recent optical searches, but remain below theoretical expectations, which generally predict an increasing dual fraction toward high redshift.

(v) The apparent decline in observed dual fractions with redshift is largely attributable to selection and observation limits. Our parent sample is anchored on luminous SDSS quasars, biasing against pairs of moderate-luminosity AGN. Companions fainter than *i*-band magnitude 22 or with contrasts of *i*-band magnitude $\gtrsim 3$ are rarely detected by SExtractor deblending, and candidates with separations below 2 arcsec are suppressed by both geometric probability and PSF blending. As a result, our survey is most sensitive to nearly equal-luminosity pairs with intermediate separations, and provides a lower bound on the true dual AGN fraction.

In summary, our spectroscopic campaign confirms that dual quasars exist across a wide redshift range but are intrinsically rare in optical surveys anchored on SDSS quasars. Their incidence is strongly shaped by selection biases, and most low-redshift mergers appear as quasar–galaxy pairs rather than dual broad-line systems. Our results have established the incidence and properties of luminous dual quasars in the SDSS + HSC era, but a complete census of dual AGN requires deeper and higher-resolution searches. Imaging and spectroscopy with *HST* and *JWST* will extend detections to smaller separations and higher contrasts, while X-ray and mid-IR observations are essential to reveal obscured nuclei. Next-generation wide-field surveys (e.g. Rubin/LSST and *Euclid)* combined with high-resolution follow-up will be critical to reconcile observations with theoretical predictions of SMBH pair growth across cosmic time.

ACKNOWLEDGEMENTS

ST and MB acknowledge funding from the Royal Society via a University Research Fellowship to MB and associated Research Fellows Enhancement Awards. Special thanks to the support astronomers at the NTT, Gemini, Keck, and *Subaru* telescopes and local ESO staffs who hosted the author's on-site visit to the La Silla observatory. This work cannot be done without their help. The authors sincerely thank the anonymous reviewer for helpful suggestions on this work.

The HSC collaboration includes the astronomical communities of Japan and Taiwan, and Princeton University. The HSC instrumentation and software were developed by the National Astronomical Observatory of Japan (NAOJ), the Kavli Institute for the Physics and Mathematics of the Universe (Kavli IPMU), the University of Tokyo, the High Energy Accelerator Research Organization (KEK), the Academia Sinica Institute for Astronomy and Astrophysics in Taiwan (ASIAA), and Princeton University. Funding was contributed by the FIRST program from the Japanese Cabinet Office, the Ministry of Education, Culture, Sports, Science and Technology (MEXT), the Japan Society for the Promotion of Science (JSPS), Japan Science and Technology Agency (JST), the Toray Science Foundation, NAOJ, Kavli IPMU, KEK, ASIAA, and Princeton University.

This paper makes use of software developed for Vera C. Rubin Observatory. We thank the Rubin Observatory for making their code available as free software at http://pipelines.lsst.io/.

This paper is based on data collected at the *Subaru* Telescope and retrieved from the HSC data archive system, which is operated by the *Subaru* Telescope and Astronomy Data Center (ADC) at NAOJ. Data analysis was in part carried out with the cooperation of Center for Computational Astrophysics (CfCA), NAOJ. We are honored and grateful for the opportunity of observing the Universe from Maunakea, which has the cultural, historical and natural significance in Hawaii.

DATA AVAILABILITY

The 'Discovery Panels' (Section 4) and reduced 1D spectrum before photometric rescaling of all the observed candidates are available as MNRAS online Supporting Information.

REFERENCES

Agazie G. et al., 2023, ApJ, 951, L50
Aihara H. et al., 2022, PASJ, 74, 247
Amaro-Seoane P. et al., 2017, preprint (arXiv:1702.00786)
Baldwin J. A., Phillips M. M., Terlevich R., 1981, PASP, 93, 5
Balmaverde B. et al., 2022, A&A, 662, A23
Begelman M. C., Blandford R. D., Rees M. J., 1980, Nature, 287, 307
Bertin E., 2013, Astrophysics Source Code Library, record ascl–1301
Bischetti M. et al., 2017, A&A, 598, A122
Boroson T. A., Green R. F., 1992, ApJS, 80, 109
Bosch J. et al., 2018, PASJ, 70, S5
Bradley L. et al., 2024, astropy/photutils: 2.0.2, Zenodo. Available at: https://doi.org/10.5281/zenodo.13989456
Buzzoni B. et al., 1984, ESO Messenger, 38, 9
Capelo P. R., Volonteri M., Dotti M., Bellovary J. M., Mayer L., Governato F., 2015, MNRAS, 447, 2123

Capelo P. R., Dotti M., Volonteri M., Mayer L., Bellovary J. M., Shen S., 2017, MNRAS, 469, 4437
Chen N. et al., 2023, MNRAS, 522, 1895
Chen Y.-C., Hwang H.-C., Shen Y., Liu X., Zakamska N. L., Yang Q., Li J. I., 2022, ApJ, 925, 162
Ciurlo A. et al., 2023, A&A, 671, L4
Coatman L., Hewett P. C., Banerji M., Richards G. T., 2016, MNRAS, 461, 647
Coatman L., Hewett P. C., Banerji M., Richards G. T., Hennawi J. F., Prochaska J. X., 2017, MNRAS, 465, 2120
Colpi M., Sesana A., 2017, An Overview of Gravitational Waves: Theory, Sources and Detection. World Scientific, Singapore, p. 43
Curti M., Cresci G., Mannucci F., Marconi A., Maiolino R., Esposito S., 2016, MNRAS, 465, 1384
De Rosa A. et al., 2023, MNRAS, 519, 5149
Di Matteo T., Springel V., Hernquist L., 2005, nature, 433, 604
Ding X. et al., 2020, ApJ, 888, 37
Ding X., Silverman J., Birrer S., Treu T., Tang S., Yang L., Bottrell C., 2022, Astrophysics Source Code Library, record ascl:2209.011
van Dokkum P., Brammer G., Baggen J. F., Keim M. A., Natarajan P., Pasha I., 2025, ApJ, 988, L6
Eftekharzadeh S., Myers A., Hennawi J., Djorgovski S., Richards G., Mahabal A., Graham M., 2017, MNRAS, 468, 77
Ellison S. L., Patton D. R., Mendel J. T., Scudder J. M., 2011, MNRAS, 418, 2043
Fanidakis N. et al., 2012, MNRAS, 419, 2797
Fernandes R. C., Stasińska G., Schlickmann M., Mateus A., Asari N. V., Schoenell W., Sodré L., Jr, collaboration S., 2010, MNRAS, 403, 1036
Fraix-Burnet D., Bouveyron C., Moultaka J., 2021, A&A, 649, A53
Guo H., Shen Y., Wang S., 2018, Astrophysics Source Code Library, record ascl:1809
Guo H., Liu X., Shen Y., Loeb A., Monroe T., Prochaska J. X., 2019, MNRAS, 482, 3288
Hamann F., Kanekar N., Prochaska J., Murphy M., Ellison S., Malec A., Milutinovic N., Ubachs W., 2011, MNRAS, 410, 1957
Hao L. et al., 2005, AJ, 129, 1783
Heckman T. M., Best P. N., 2014, ARA&A, 52, 589
Hennawi J. F. et al., 2006, AJ, 131, 1
Hennawi J. F. et al., 2010, ApJ, 719, 1672
Hickox R. C., Alexander D. M., 2018, ARA&A, 56, 625
Hook I., Jorgensen I., Allington-Smith J., Davies R., Metcalfe N., Murowinski R., Crampton D., 2004, PASP, 116, 425
Hopkins P. F., Quataert E., 2010, MNRAS, 407, 1529
Hopkins P. F., Hernquist L., Cox T. J., Di Matteo T., Robertson B., Springel V., 2006, ApJS, 163, 1
Huang S. et al., 2017, PASJ, 70, S6
Hwang H.-C., Shen Y., Zakamska N., Liu X., 2020, ApJ, 888, 73
Inada N. et al., 2008, AJ, 135, 496
Inada N. et al., 2012, AJ, 143, 119
Jackson N., Rampadarath H., Ofek E. O., Oguri M., Shin M.-S., 2012, MNRAS, 419, 2014
Jones M. L., Hickox R. C., Black C. S., Hainline K. N., DiPompeo M. A., Goulding A. D., 2016, ApJ, 826, 12
Kashikawa N. et al., 2002, PASJ, 54, 819
Kaspi S., Smith P. S., Netzer H., Maoz D., Jannuzi B. T., Giveon U., 2000, ApJ, 533, 631
Kawaguchi T., Yutani N., Wada K., 2020, ApJ, 890, 125
Kayo I., Oguri M., 2012, MNRAS, 424, 1363
Kelson D. D., 2003, PASP, 115, 688
Kewley L. J., Dopita M. A., 2002, ApJS, 142, 35
Landoni M., Falomo R., Treves A., Scarpa R., Farina E., 2016, MNRAS, 457, 267
Li J., Zhuang M.-Y., Shen Y., 2024, ApJ, 961, 19
Li J., Zhuang M.-Y., Shen Y., Volonteri M., Chen N., Di Matteo T., 2025, ApJ, 986, 101
Li M. et al., 2026, ApJ, 999, 40
Lyman R., Cherubini T., Businger S., 2020, MNRAS, 496, 4734
Mannucci F. et al., 2022, Nat. Astron., 6, 1185
Mannucci F. et al., 2023, A&A, 680, A53
Marian V. et al., 2019, ApJ, 882, 141
Marian V. et al., 2020, ApJ, 904, 79
Matsuoka Y. et al., 2024, ApJ, 965, L4
Molyneux S. et al., 2025, MNRAS, 540, 1163
More A. et al., 2016, MNRAS, 456, 1595
Myers A. D. et al., 2015, ApJS, 221, 27
Nakajima K., Ouchi M., 2014, MNRAS, 442, 900
Netzer H., 2015, ARA&A, 53, 365
Oke J., 1990, AJ, 99, 1621
Pagel B., Edmunds M., Blackwell D., Chun M., Smith G., 1979, MNRAS, 189, 95
Pâris I. et al., 2018, A&A, 613, A51
Perna M. et al., 2025, A&A, 696, A59
Perna M. et al., 2026, preprint (arXiv:2601.00960)
Prochaska J. X. et al. 2020, J. Open Source Softw., 5, 2308
Prochaska J. X. et al., 2023, pypeit/PypeIt: Version 1.12.2. Zenodo. Available at: https://doi.org/10.5281/zenodo.7779402
Rakshit S., Stalin C., Kotilainen J., 2020, ApJS, 249, 17
Ren W., Guo H., Shen Y., Silverman J. D., Burke C. J., Wang S., Wang J., 2024, ApJ, 974, 153
Ricci C., Trakhtenbrot B., 2023, Nat. Astron., 7, 1282
Richards G. T. et al., 2001, AJ, 121, 2308
Richards G. T. et al., 2002, AJ, 123, 2945
Richards G. T. et al., 2006, ApJS, 166, 470
Rodríguez-Baras M., Rosales-Ortega F., Díaz A., Sánchez S., Pasquali A., 2014, MNRAS, 442, 495
Rosas-Guevara Y. M., Bower R. G., McAlpine S., Bonoli S., Tissera P. B., 2019, MNRAS, 483, 2712
Runnoe J. C., Brotherton M. S., Shang Z., 2012, MNRAS, 422, 478
Saeedzadeh V., Babul A., Mukherjee S., Tremmel M., Quinn T. R., Mayer L., 2024, ApJ, 975, 265
Schreiber N. F. et al., 2018, ApJS, 238, 21
Schulze A. et al., 2017, ApJ, 848, 104
Schulze A. et al., 2018, ApJS, 239, 22
Scialpi M. et al., 2024, A&A, 690, A57
Shen Y. et al., 2011, ApJS, 194, 45
Shen Y. et al., 2019, ApJS, 241, 34
Shen Y. et al., 2021, Nat. Astron., 5, 569
Shen Y. et al., 2023, ApJ, 943, 38
Silverman J. et al., 2011, ApJ, 743, 2
Silverman J. D. et al., 2020, ApJ, 899, 154
Steinborn L. K., Dolag K., Comerford J. M., Hirschmann M., Remus R.-S., Teklu A. F., 2016, MNRAS, 458, 1013
Tang S. et al., 2021, ApJ, 922, 83
Tang S. et al., 2023, MNRAS, 521, 5272
Tang S. et al., 2025, MNRAS, 538, 3001
Treister E., Schawinski K., Urry C., Simmons B. D., 2012, ApJ, 758, L39
Ulivi L. et al., 2025, preprint (arXiv:2508.19494)
Van Wassenhove S., Volonteri M., Mayer L., Dotti M., Bellovary J., Callegari S., 2012, ApJ, 748, L7
Vestergaard M., 2003, ApJ, 599, 116
Vestergaard M., Peterson B. M., 2006, ApJ, 641, 689
Vestergaard M., Wilkes B. J., 2001, ApJS, 134, 1
Villarroel B., Nyholm A., Karlsson T., Comerón S., Korn A. J., Sollerman J., Zackrisson E., 2017, ApJ, 837, 110
Villforth C. et al., 2014, MNRAS, 439, 3342
Volonteri M., Pfister H., Beckmann R., Dotti M., Dubois Y., Massonneau W., Musoke G., Tremmel M., 2022, MNRAS, 514, 640
Wang Q. et al., 2026, ApJ, 997, 269
Wilson J. C. et al., 2004, in Moorwood A. F. M., Masanori I., Proc. SPIE, Vol. 5492, Ground-based Instrumentation for Astronomy, Mass Producing an Efficient NIR Spectrograph. SPIE, Glasgow, UK, p. 1295
Zhao Y., Li Y. A., Shangguan J., Zhuang M.-Y., Ho L. C., 2022, ApJ, 925, 70

SUPPORTING INFORMATION

Supplementary data are available at *MNRAS* online.

Tang2025_Table1.csv
reduced_1D_spec.zip
readme_of_supplementary_files.txt
PyQSOFit_results.zip
discovery_panels.zip
absorption_line_fitting_results.zip

Please note: Oxford University Press is not responsible for the content or functionality of any supporting materials supplied by the authors. Any queries (other than missing material) should be directed to the corresponding author for the article.

APPENDIX A: PHOTOMETRIC COMPARISON BETWEEN PSF AND CMODEL MAGNITUDES

As described in Section 2, we used GALIGHT to measure the PSF magnitudes of candidate sources through 2D image decomposition. In Fig. A1, we compare these measurements with the CModel magnitudes provided by the HSC pipeline (J. Bosch et al. 2018). The top row shows the five-band comparison for the SDSS quasars in each candidate pair, while the bottom row shows the same for the companion sources. Red dashed lines indicate the one-to-one relation, and points are colour-coded by the redshift of the SDSS quasar. On top left of each panel, the percentage indicates the fraction of sources with consistent magnitudes (agreement within ± 0.2 mag) between the two methods.

For the quasars, we find good overall agreement across all bands, with consistency fractions above 80 per cent. The small fraction of outliers are primarily at $z < 1$, where host galaxy light contributes significantly to the CModel fluxes, while our PSF magnitudes better isolate the unresolved nuclear component. Since the PSF magnitudes are used to rescale the spectra to correct for slit loss (see Section 3.2), this comparison validates our approach. Importantly, all of our confirmed dual quasars lie at $z > 1.5$, where host-galaxy contamination is minimal, so the choice between PSF and CModel magnitudes does not affect our measurements of emission lines or BH properties.

For the companion sources (bottom row), the agreement is substantially worse, with consistency fractions of only ∼63–67 per cent across the five bands. A notable 58 out of 883 companions are not recorded at all in the HSC pipeline catalogue, typically due to blending in pairs with <1 arcsec separations. This highlights the necessity of applying our own 2D image analysis techniques to select out dual candidates rather than relying exclusively on the catalogue (Section 2.1). Among the measured companions, many of the most discrepant cases are associated with high-redshift quasars ($z > 1.5$), suggesting that a significant fraction of these companions are foreground or background interlopers (i.e. projected pairs). We also note that the companions' *g*- and *r*-band magnitudes are systematically fainter relative to their matched quasars, suggesting a substantial population of contaminating stars (S. Tang et al. 2021). In forthcoming work, we plan to combine PSF–CModel consistency checks with more sophisticated color-based selections using the full five-band photometry, as an additional diagnostic to filter contaminants in future work.

APPENDIX B: 'DISCOVERY PANELS' OF DUAL AND OFFSET QUASARS

Here, we present the 'Discovery panels' of dual and offset quasars as described in Section 4. The format of the panels is similar to Fig. 3. Figs B1–B7 present the dual quasars, and Figs B8–B20 present the offset quasars. All these 'Discovery panels', including the other observed sources are available via the MNRAS online Supporting Information.

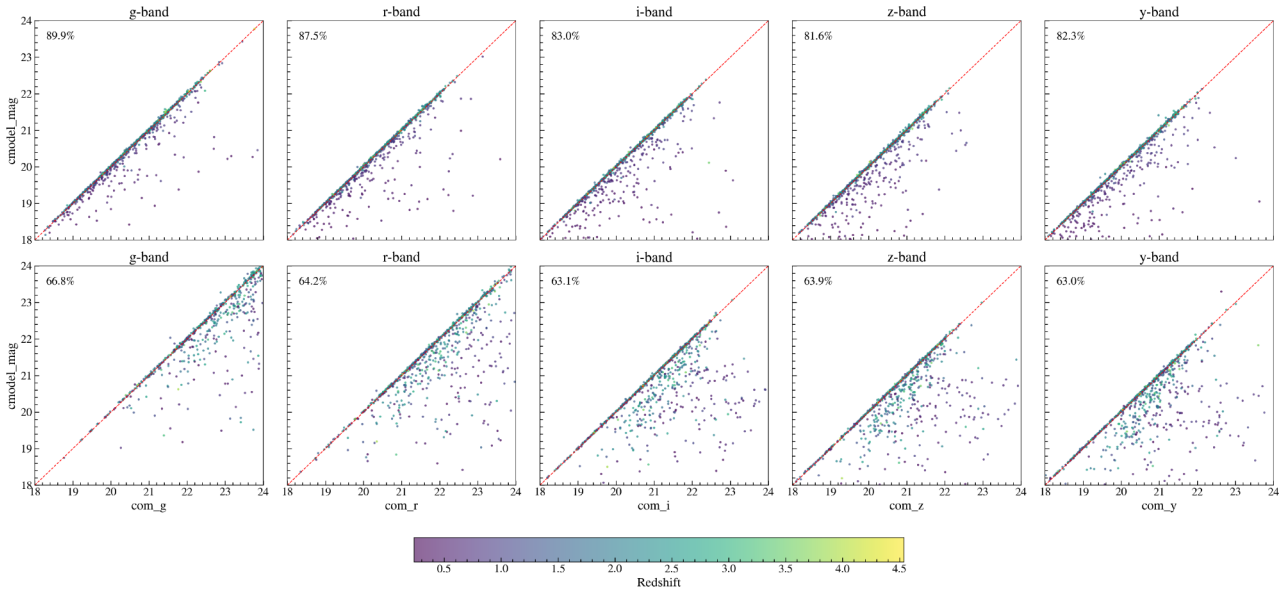

Figure A1. Comparison between GALIGHT-measured PSF magnitudes (*x*-axis) and HSC pipeline CModel magnitudes (*y*-axis). The top row shows SDSS quasars in each candidate pair; the bottom row shows the companion sources. Each panel corresponds to one HSC band (*g*, *r*, *i*, *z*, *y*), with the dashed line indicating the 1:1 relation. Points are colour-coded by the redshift of the SDSS quasar, and the percentage in the top left of each panel gives the fraction of sources with consistent measurements ($\Delta m < 0.2$ mag).

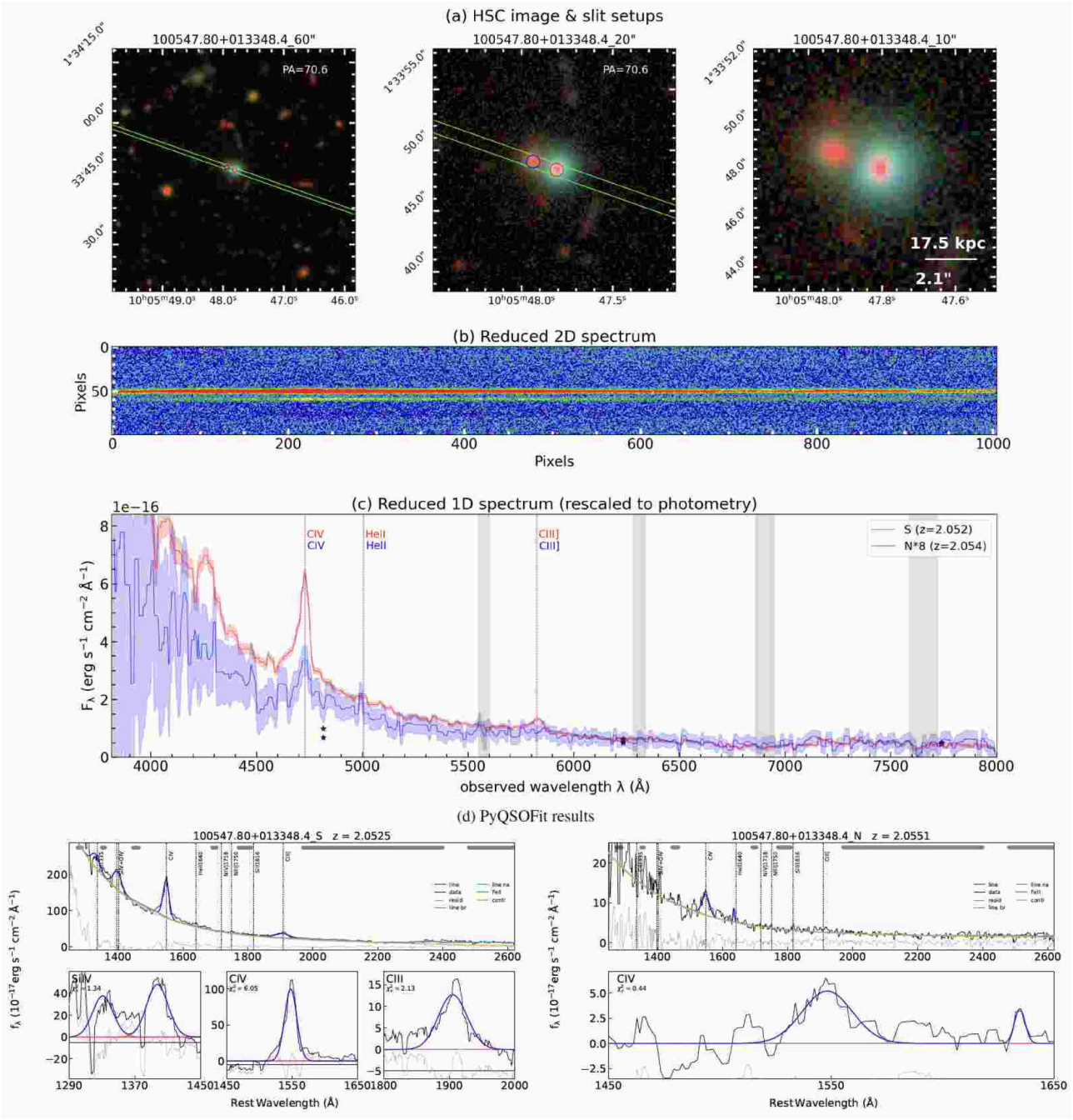

Figure B1. Discovery panel reporting the NTT/EFOSC2 spectrograph of SDSS J100547.80 + 013348.4. The bottom panels show the PyQSOFit results for both sources. This system is confirmed as a dual quasar (Section 4.1.2).

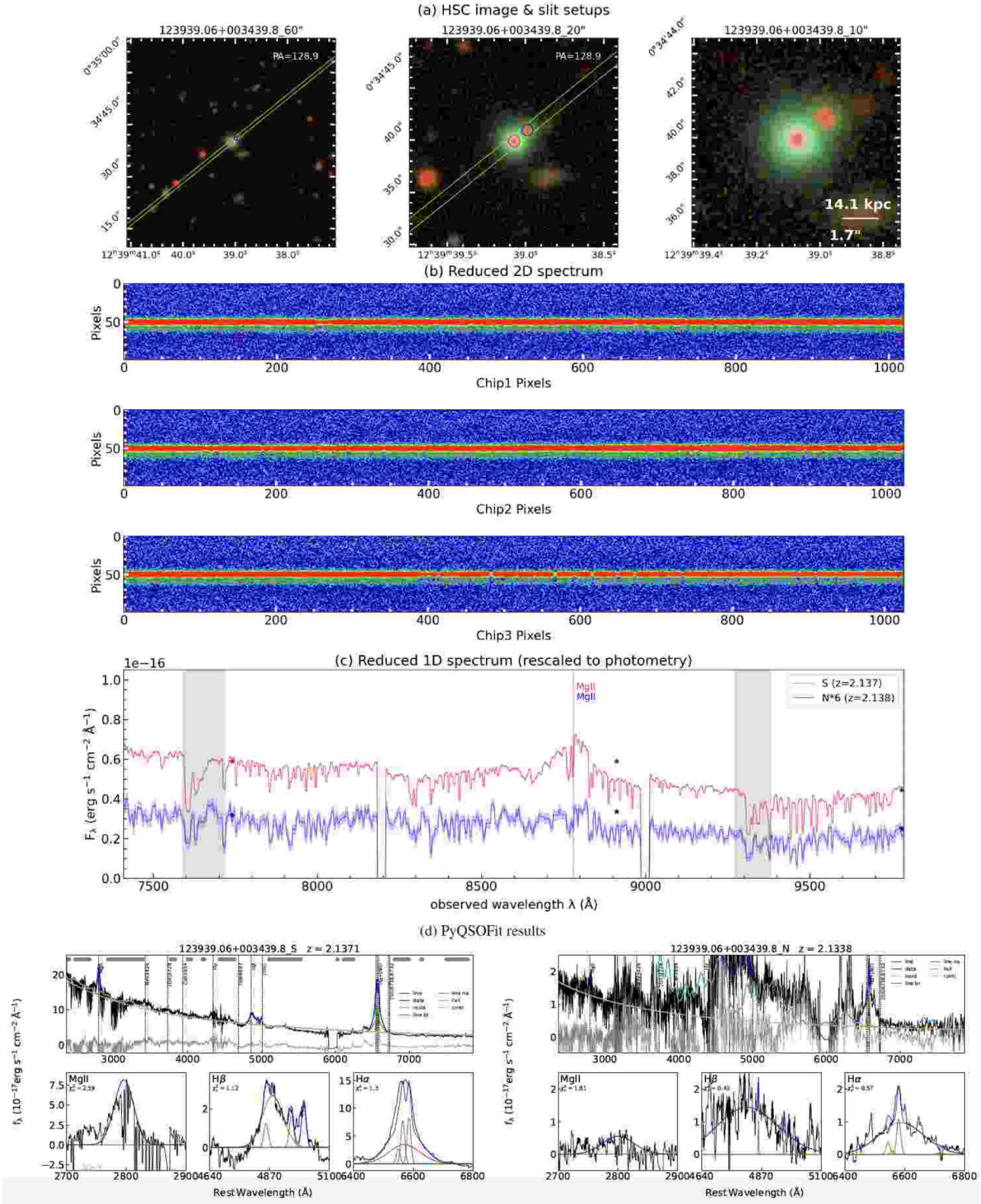

Figure B2. Discovery panel reporting the Gemini/GMOS spectrograph of SDSS J123939.06 + 003439.8. The bottom panels show the PyQSOFit results for both sources, performed on the combined spectrum including the Keck/NIRES part (Fig. B2). This system is confirmed as a dual quasar (Section 4.1.3).

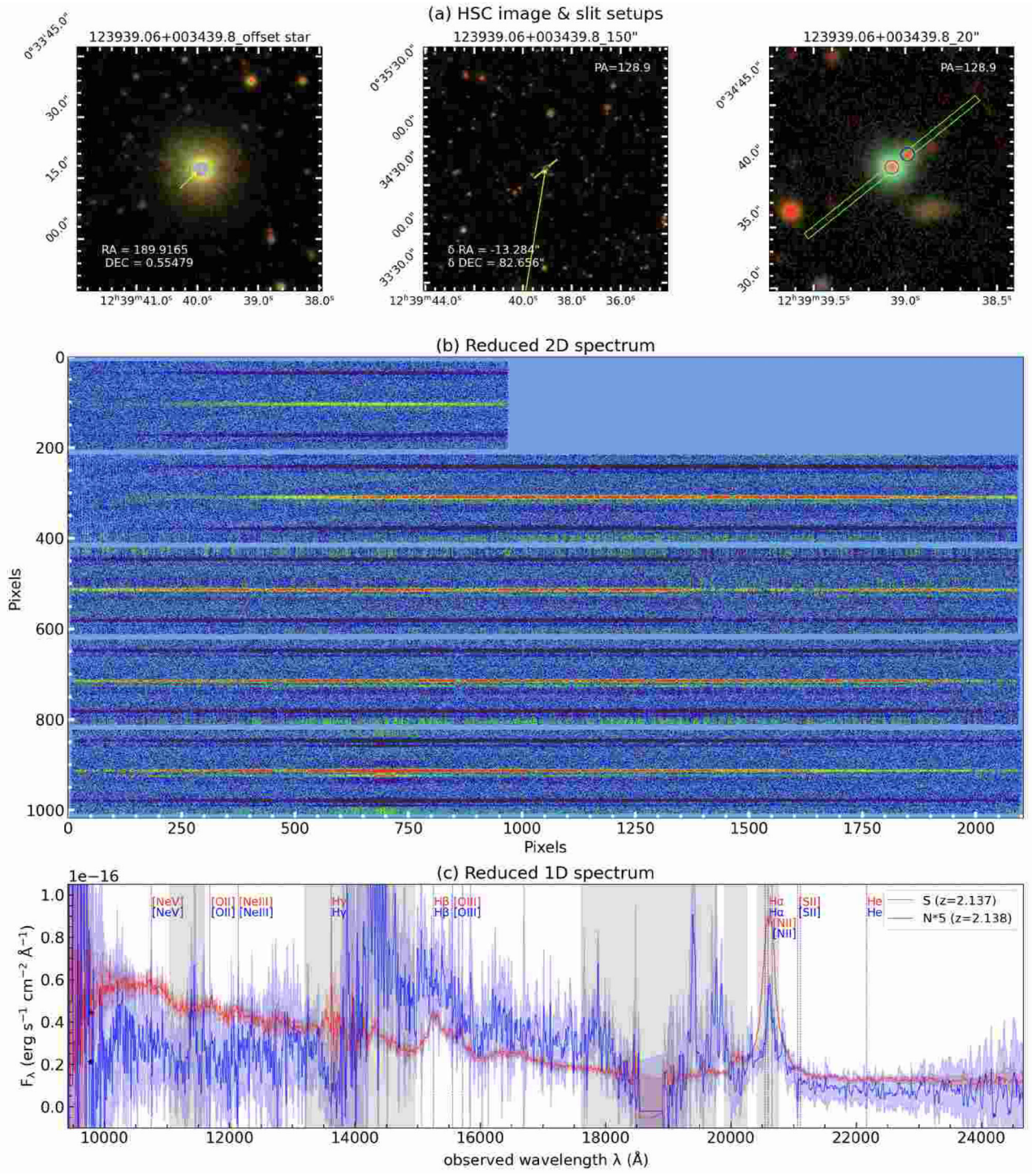

Figure B3. Discovery panel reporting the Keck/NIRES spectrograph of SDSS J123939.06 + 003439.8. This is the same object as in Fig. B2. For Keck/NIRES spectrograph, we need to find an offset star (left panel of a), then shift the slit to our objects (middle panel of a). The coordinate of the offset star and the offset distance are noted in these two panels.

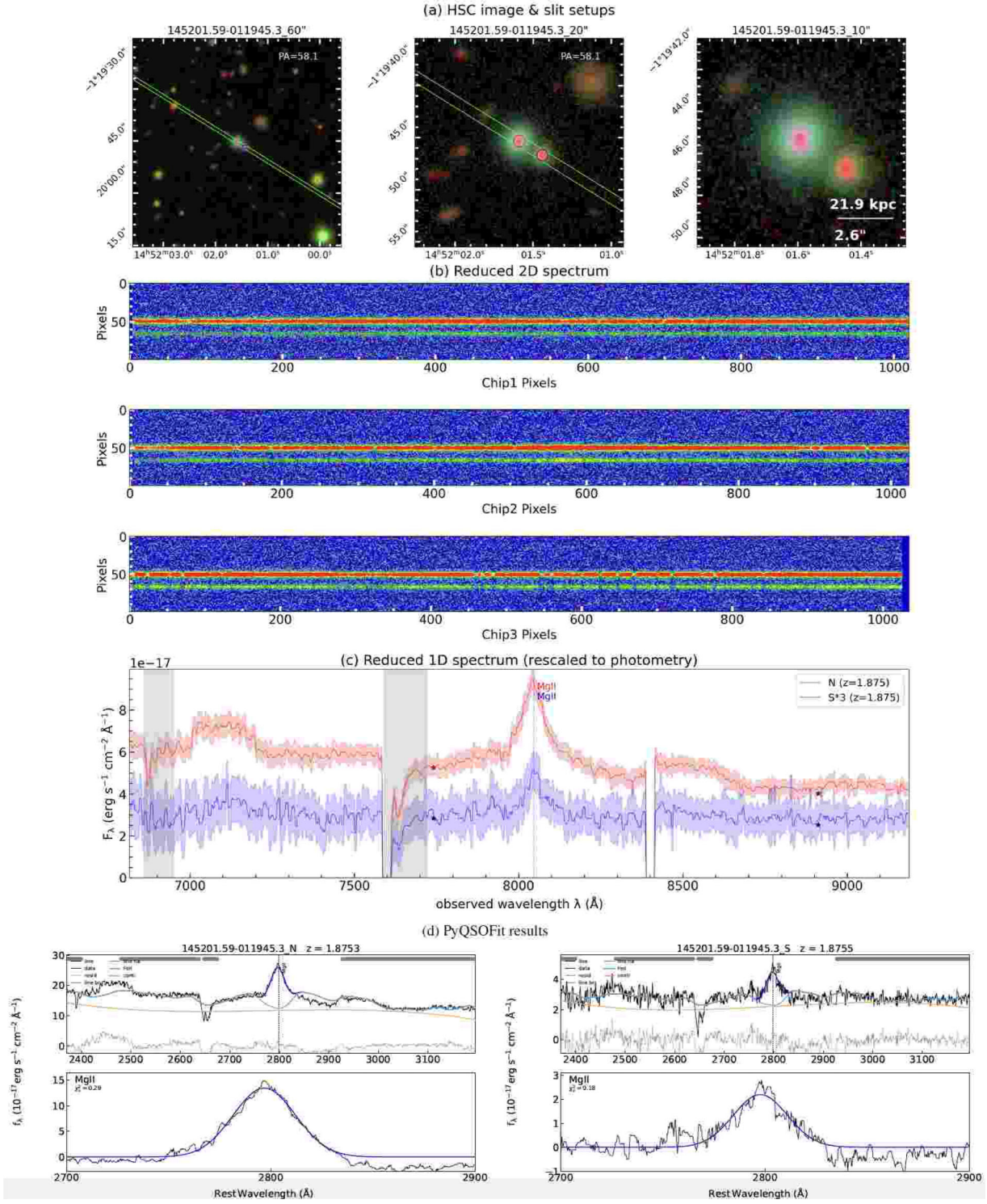

Figure B4. Discovery panel reporting the Gemini/GMOS spectrograph of SDSS J145201.59−011945.3. The bottom panels show the PyQSOFit results for both sources. This system is confirmed as a dual quasar (Section 4.1.4).

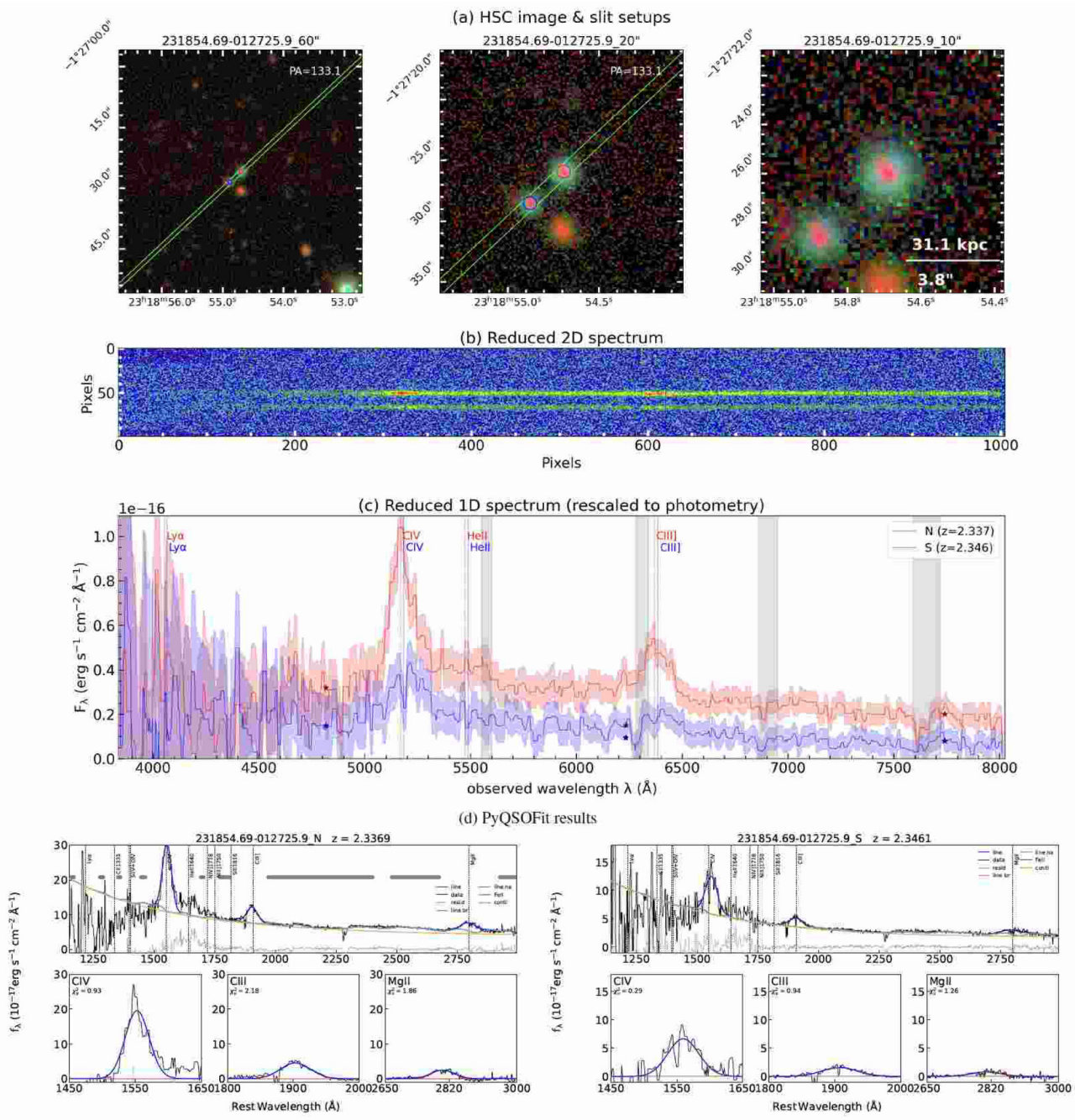

Figure B5. Discovery panel reporting the NTT/EFOSC2 spectrograph of SDSS J231854.69−012725.9. The bottom panels show the PyQSOFit results for both sources, performed on the combined spectrum including the *Subaru*/FOCAS part (Fig. B6). This system is confirmed as a dual quasar (Section 4.1.5).

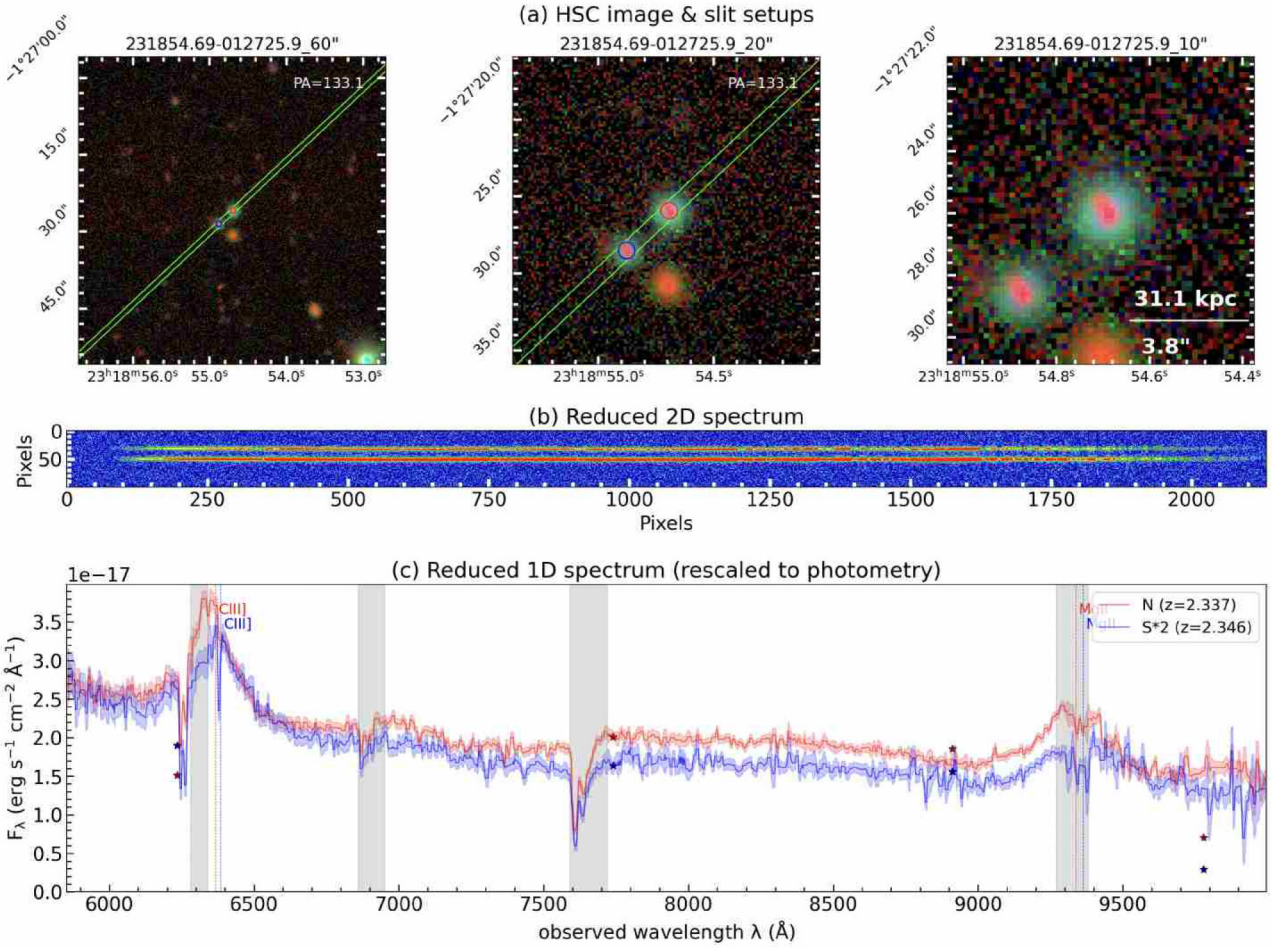

Figure B6. Discovery panel reporting the *Subaru*/FOCAS spectrograph of SDSS J231854.69−012725.9. This is the same source as in Fig. B5.

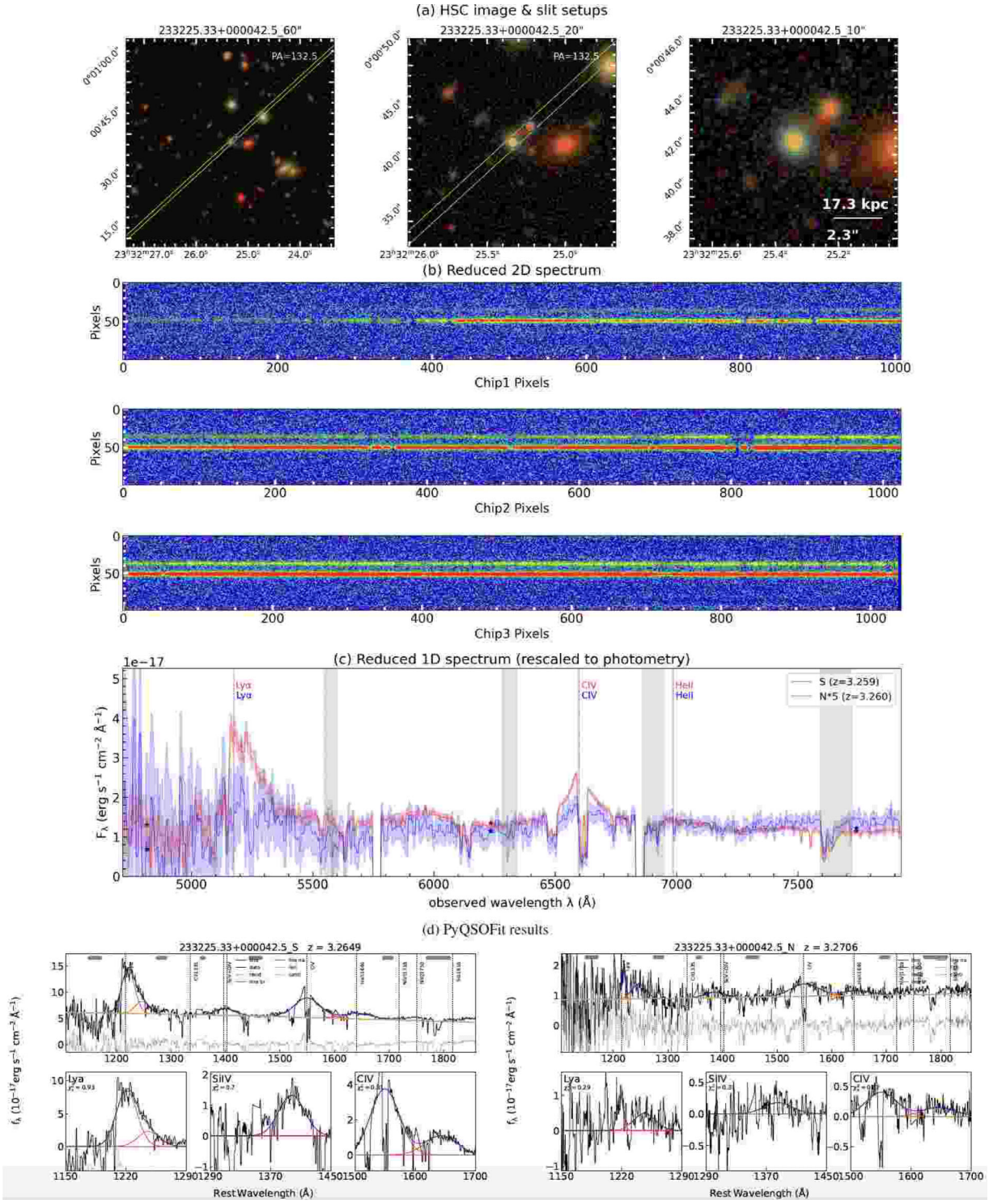

Figure B7. Discovery panel reporting the NTT/EFOSC2 spectrograph of SDSS J233225.33 + 000042.5. The bottom panels show the PyQSOFit results for both sources. This system is confirmed as a dual quasar (Section 4.1.6).

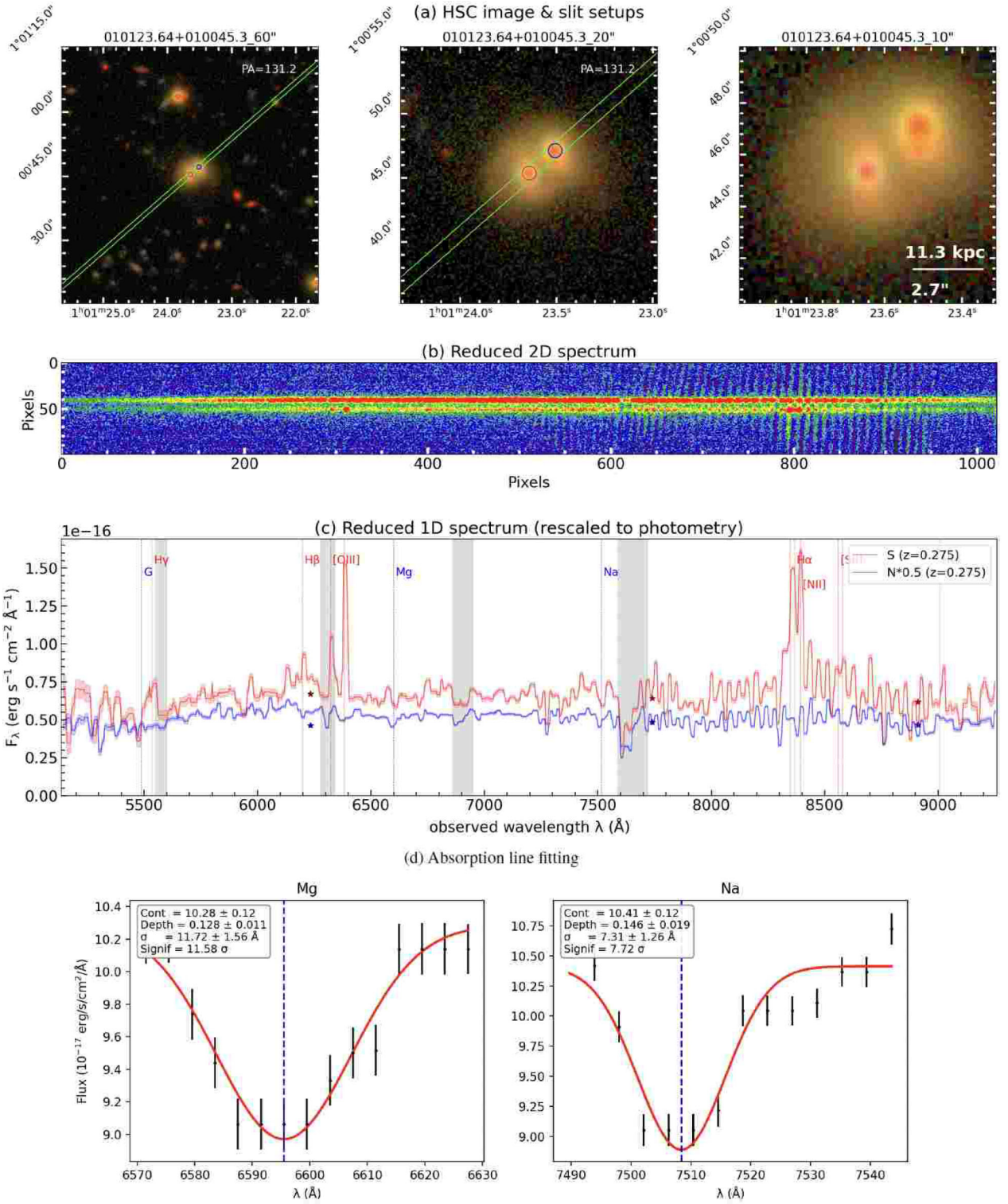

Figure B8. Discovery panel reporting the NTT/EFOSC2 spectrograph of SDSS J010123.64 + 010045.3. This system is confirmed as a quasar–QG pair (Section 4.2.1). The bottom two panels show the fitting of Mg and Na absorption lines of the companion's spectrum. For the absorption fitting plots in general, the window is centred at the expected position of the absorption lines at the redshift given in the 1D spectrum panel. The data are plotted as the black points with 1σ flux error. Note that the flux level might be different from what is plotted in panel (c) in some cases, this is because we rescaled the spectrum in panel (c) for visibility. The rescaling factor is noted in the labels of panel (c). The fitting is performed on the original spectrum before rescaling. We apply double Gaussian model to the Ca H&K and single Gaussian to the other lines with `scipy.opt.curve_fit`. The best-fitting models are plotted as the red curve. The line centres are marked with the vertical blue dashed line. The best-fitting parameters are noted on top left of each panel, which include: (1) the continuum level; (2) the depth of the absorption, defined as the distance of the peak from the continuum floor; (3) the width of the line, which is the σ of the Gaussian profile; and (4) significance of the line, defined as the depth divided by the uncertainty of the depth. The same format applies for the rest of the samples with absorption line fitting panels.

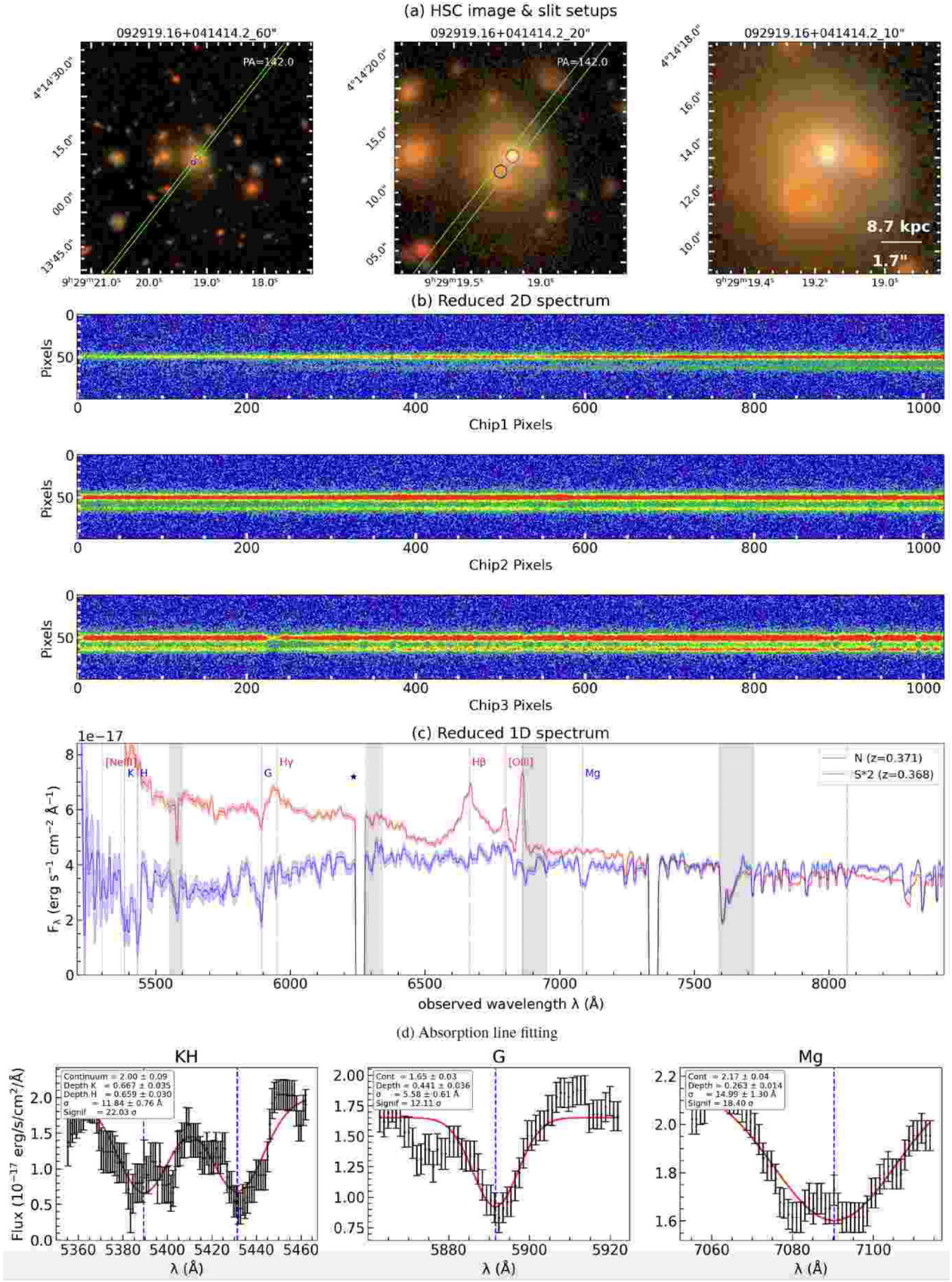

Figure B9. Discovery panel reporting the Gemini/GMOS spectrograph of SDSS J092919.16 + 041414.2, covering the quasar and the lower left companion. This system is confirmed as a quasar–QG–QG triple system (Section 4.2.2). The bottom panels show the fitting of the Ca H&K, *G* band, and Mg absorption lines of the companion's spectrum.

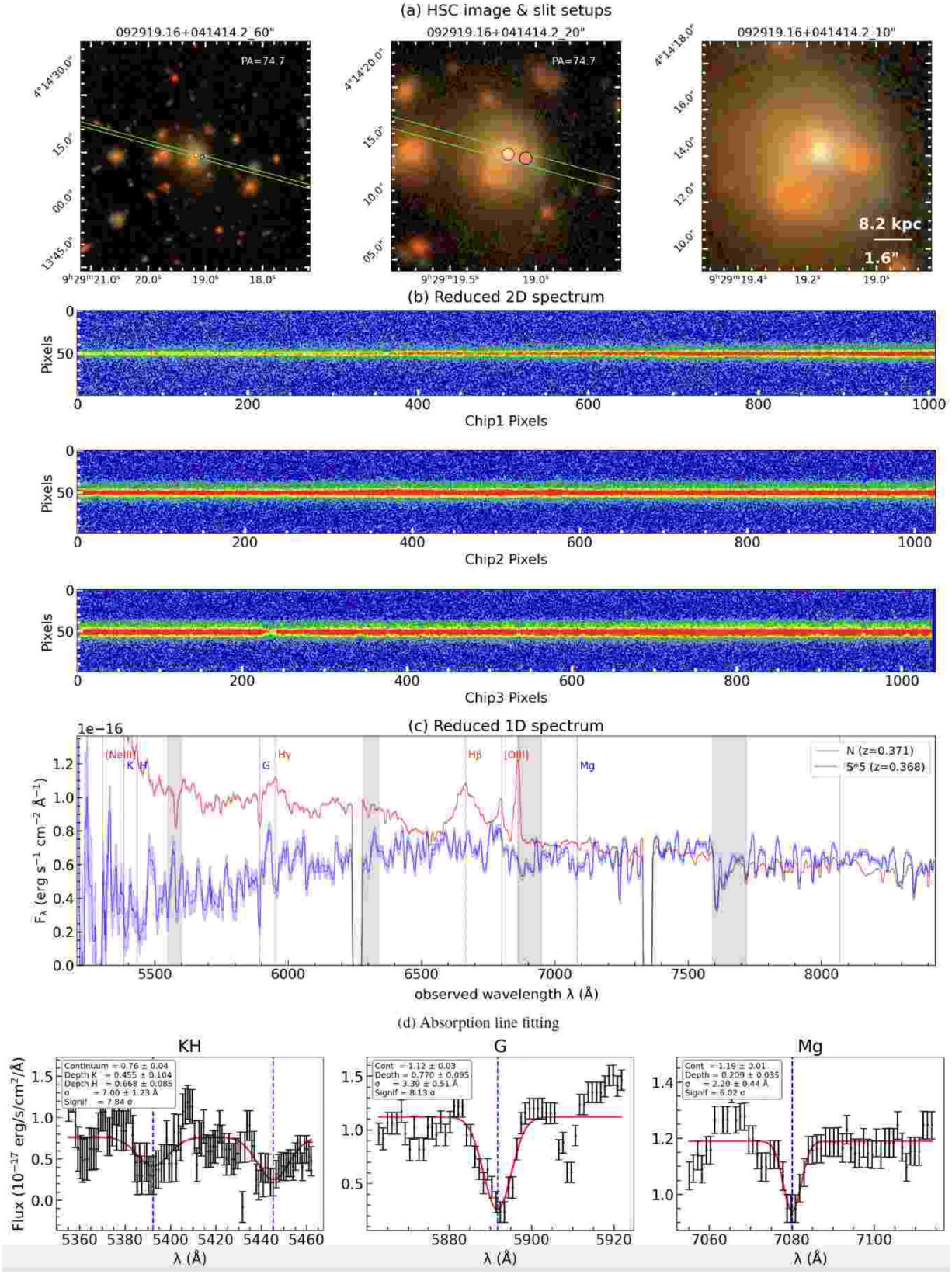

Figure B10. Discovery panel reporting the Gemini/GMOS spectrograph of SDSS J092919.16 + 041414.2, covering the quasar and the lower left companion. This is the same system as in Fig. B9, but covering different companions. We observed this system twice instead of once with the slit covering both of the companions for two reasons: (1) to better deblend the quasar emission from the companions with the method described in Section 2.3.1; and (2) to cover the 'arc' structure above the quasar. The bottom panels show the fitting of the Ca H&K, *G* band, and Mg absorption lines of the companion's spectrum.

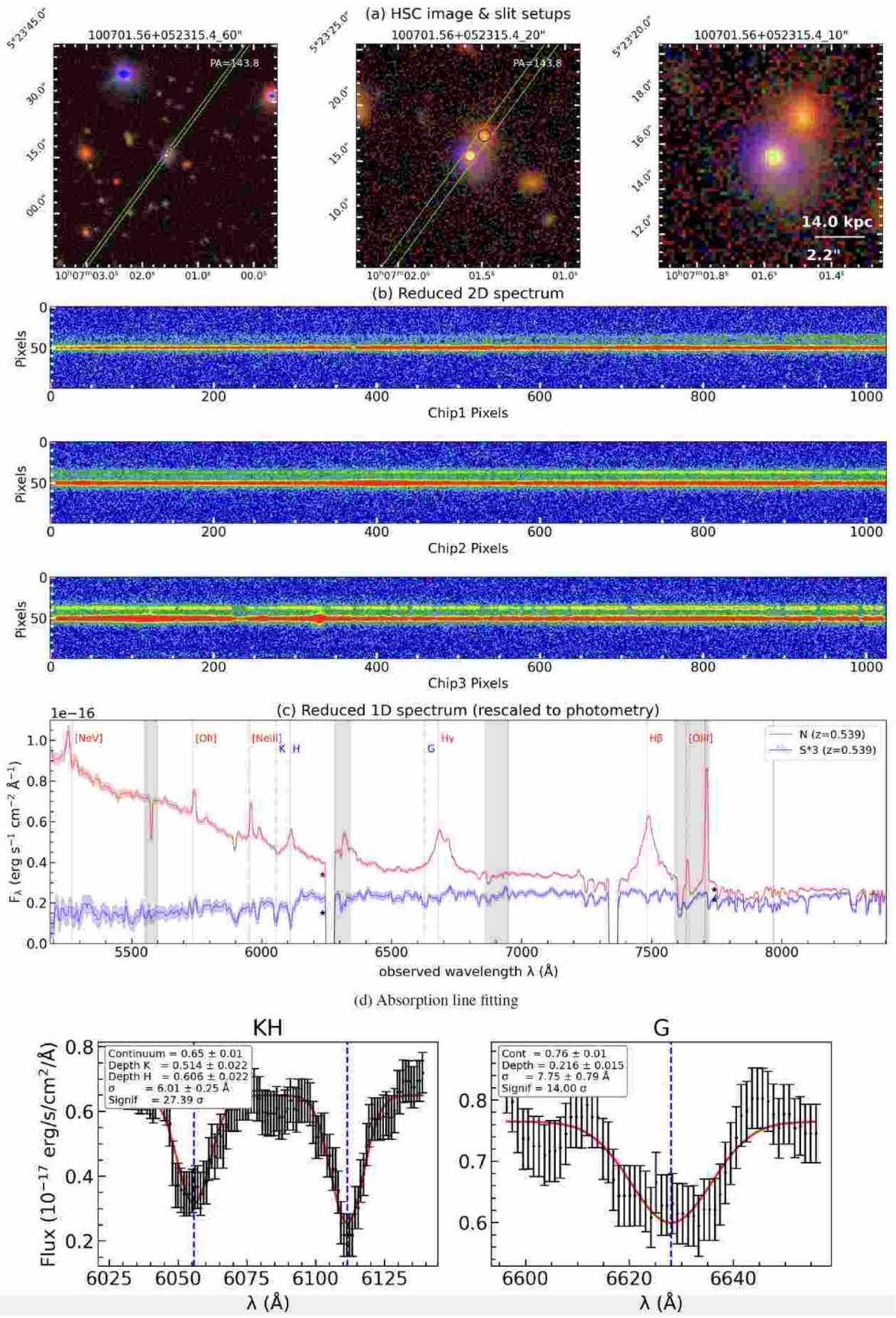

Figure B11. Discovery panel reporting the Gemini/GMOS spectrograph of SDSS J100701.56 + 052315.4. This system is confirmed as a quasar–QG pair (Section 4.2.3). The bottom panels show the fitting of the Ca H&K and *G*-band absorption lines of the companion's spectrum.

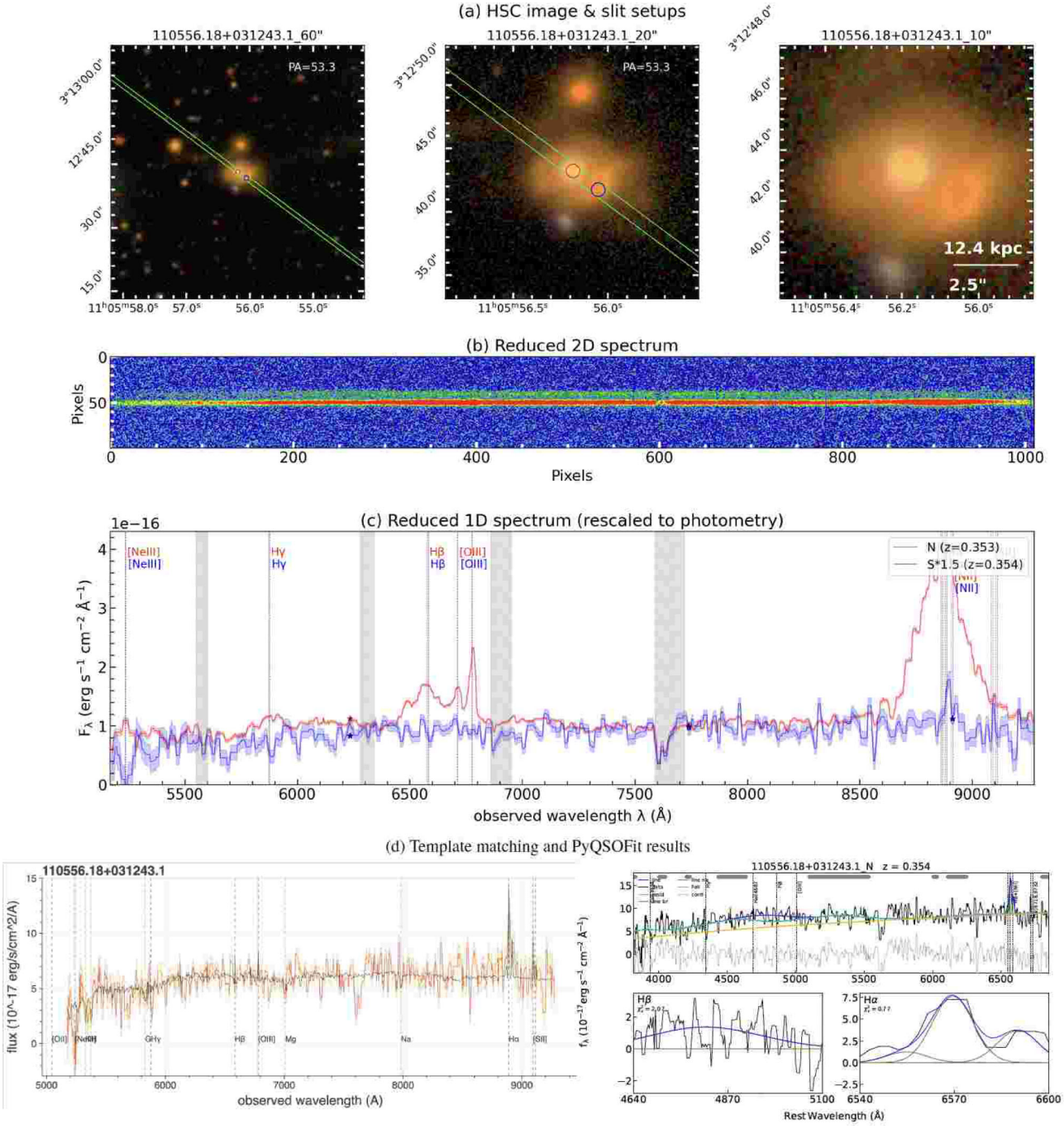

Figure B12. Discovery panel reporting the NTT/EFOSC2 spectrograph of SDSS J110556.18 + 031243.1. This system is confirmed as a quasar–SFG/QG pair (Section 4.2.4). The bottom-left panel shows the comparison between the spectrum of the companion (red curve) and an SDSS galaxy template (black curve) at $z = 0.354$. The bottom-right panel shows the PyQSOFit results of the companion's spectrum.

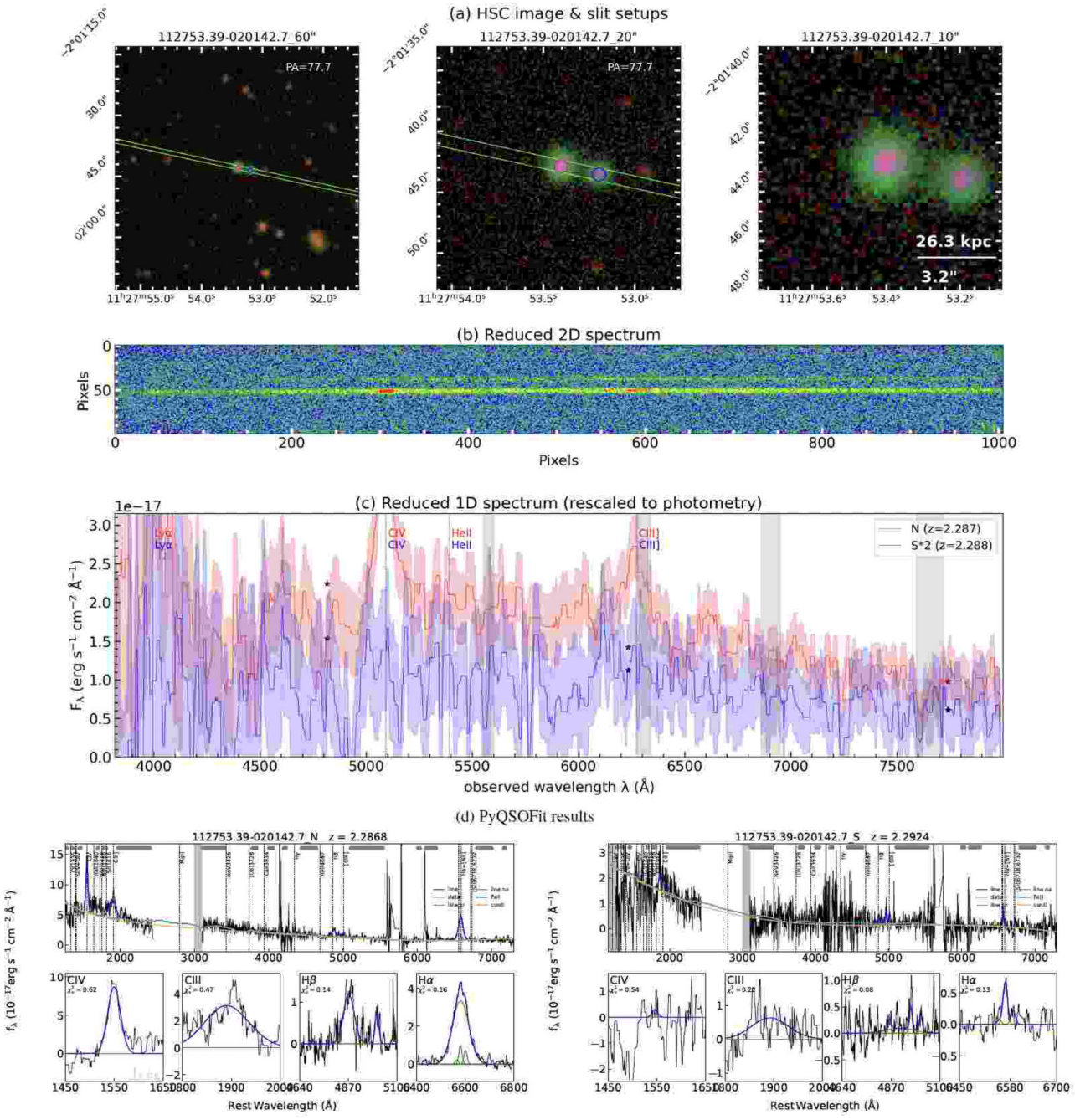

Figure B13. Discovery panel reporting the NTT/EFOSC2 spectrograph of SDSS J112753.39−020142.7. This system is confirmed as a quasar–SFG pair (Section 4.2.5). The bottom panels show the PyQSOFit results on the combined spectrum including the Keck/NIRES part (Fig. B14, of both the quasar and the companion).

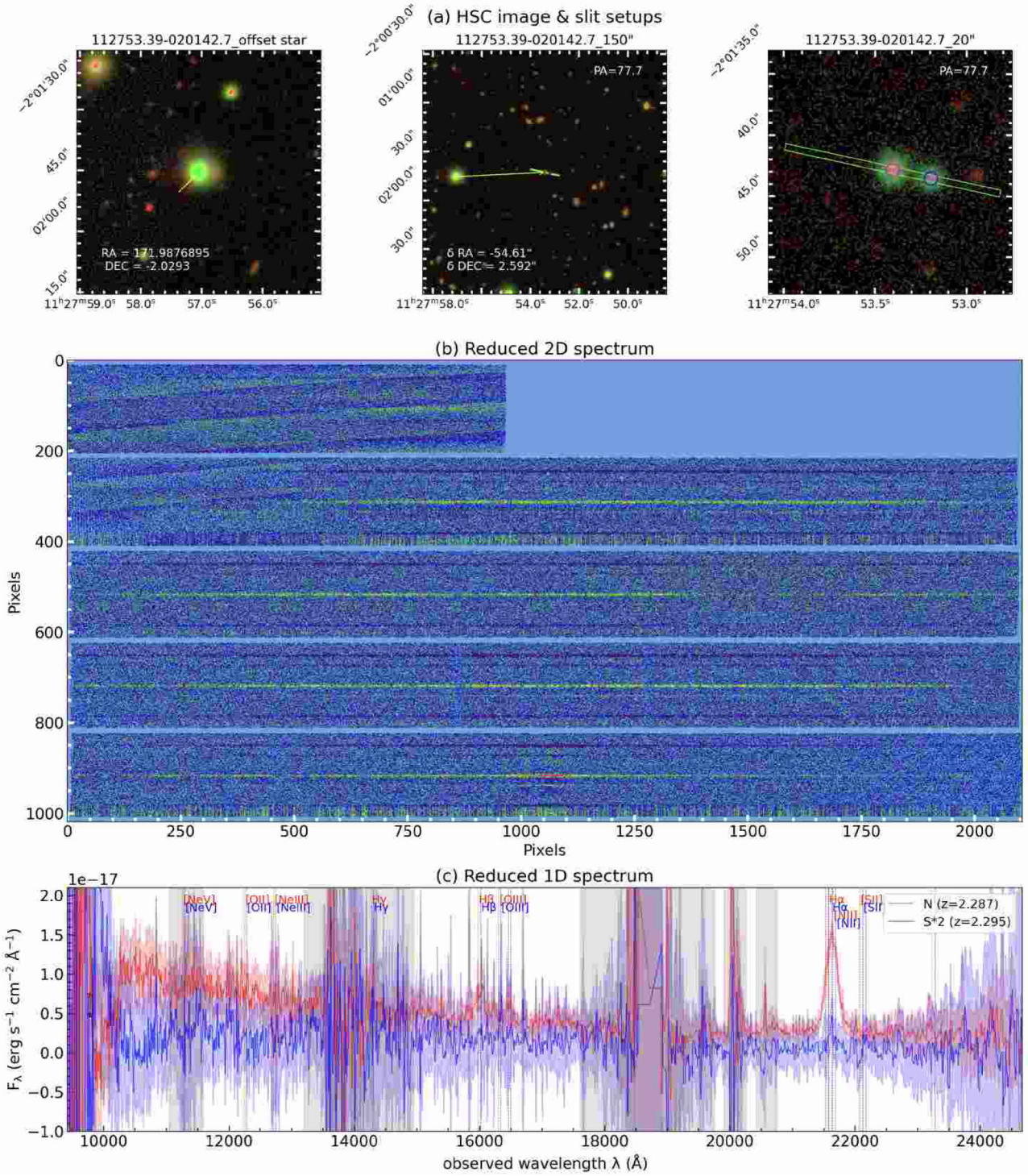

Figure B14. Discovery panel reporting the Keck/NIRES spectrograph of J112753.39−020142.7. This is the same system as in Fig. B13.

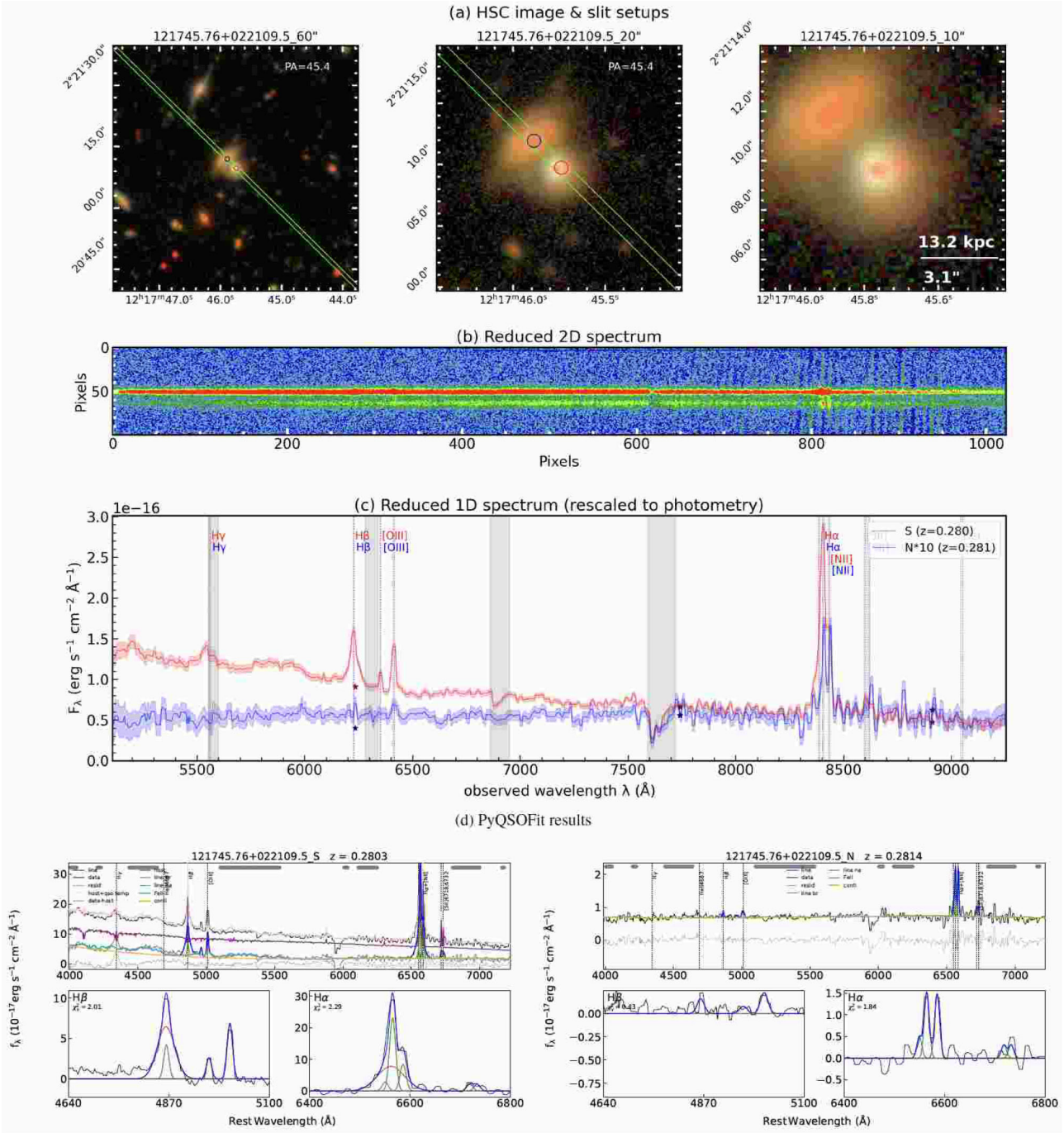

Figure B15. Discovery panel reporting the NTT/EFOSC2 spectrograph of SDSS J121745.76 + 022109.5. This system is confirmed as a quasar–SFG pair (Section 4.2.6). The bottom panels show the PyQSOFit results for both the quasar and the companion.

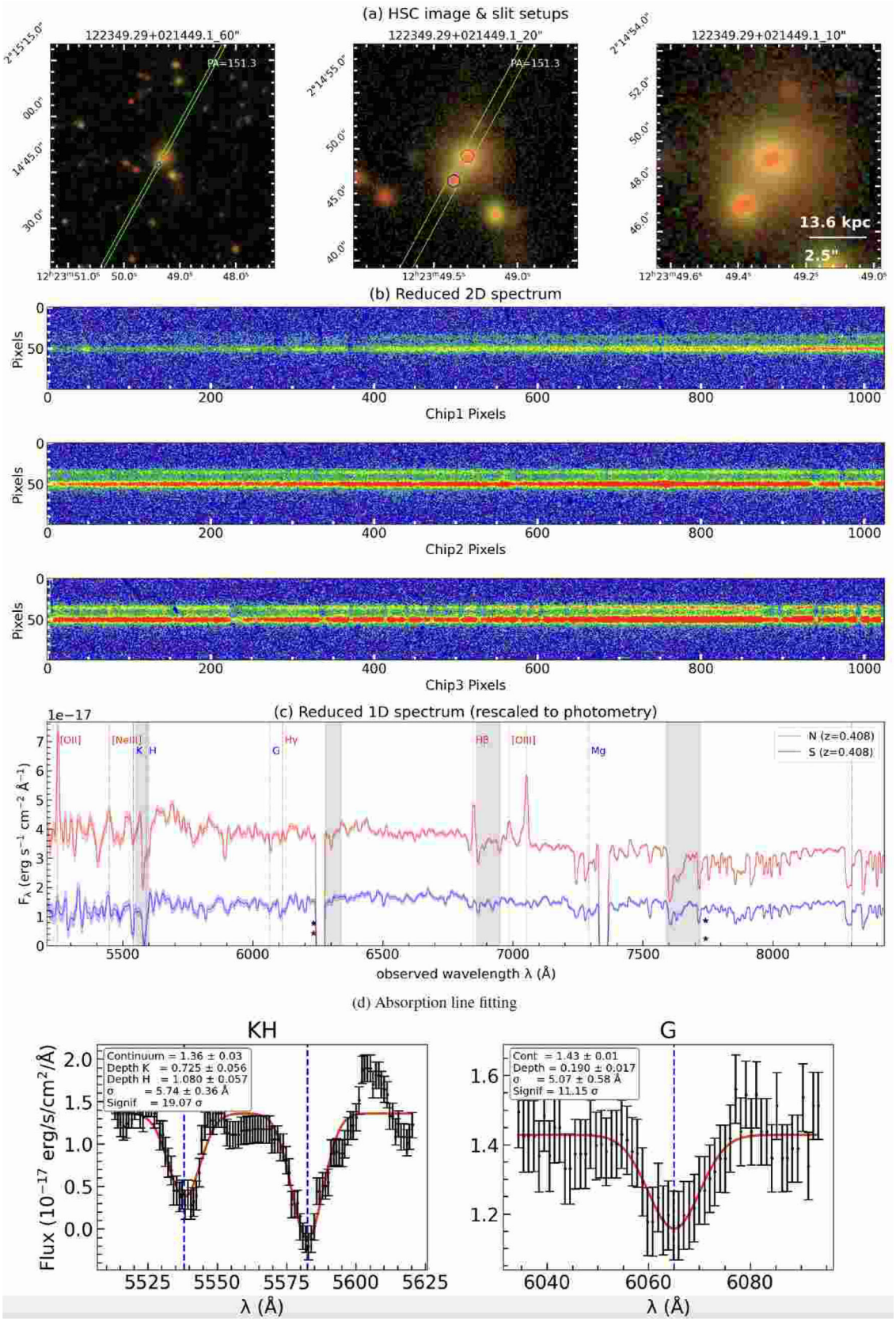

Figure B16. Discovery panel reporting the Gemini/GMOS spectrograph of SDSS J122349.29 + 021449.1. This system is confirmed as a quasar–QG pair (Section 4.2.7). The bottom panels show the fittings of the Ca H&K and *G*-band absorption lines of the companion's spectrum.

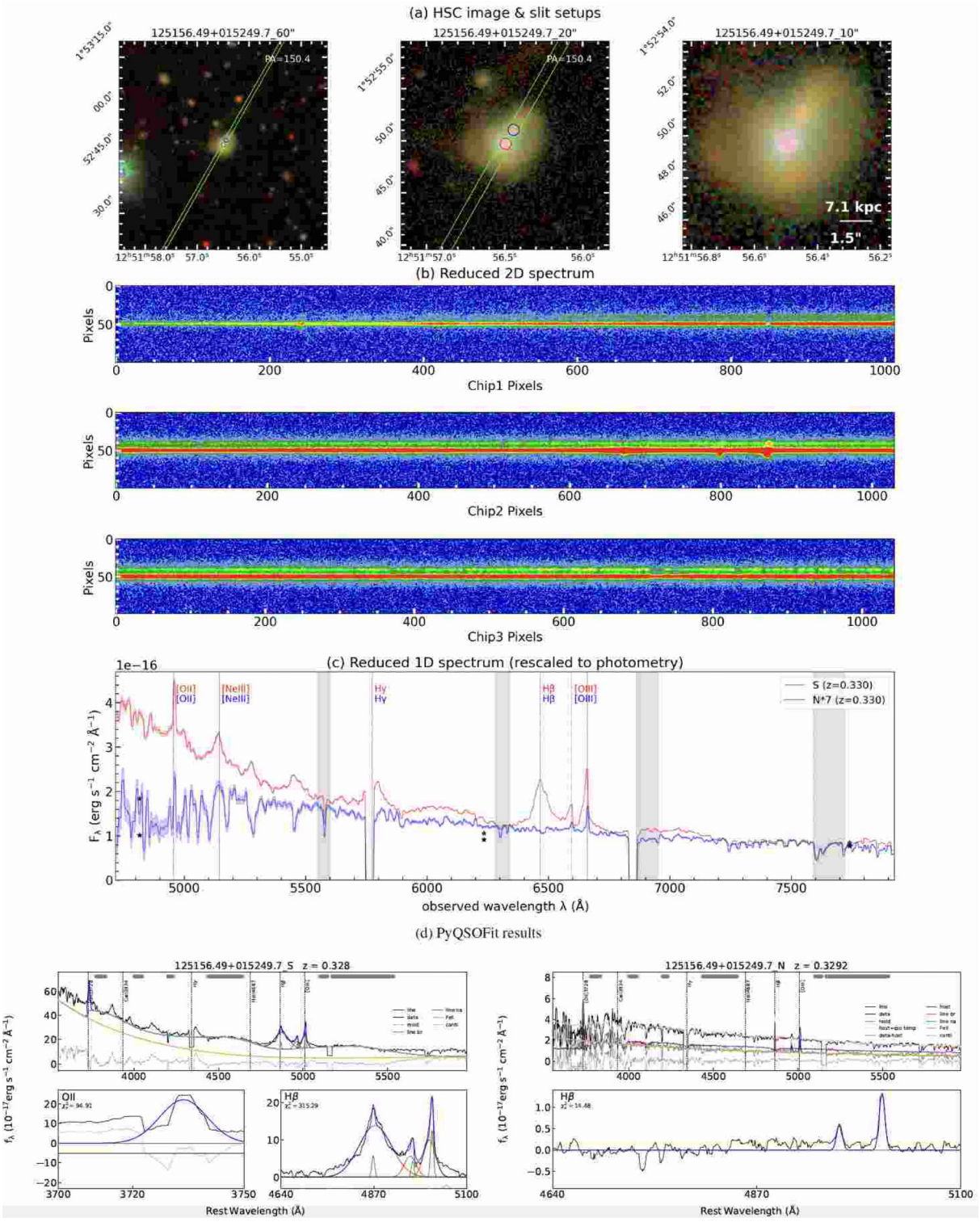

Figure B17. Discovery panel reporting the Gemini/GMOS spectrograph of SDSS J125156.49 + 015249.7. This system is confirmed as a quasar–SFG pair (Section 4.2.8). The bottom panels show the PyQSOFit results of both the quasar and the companion.

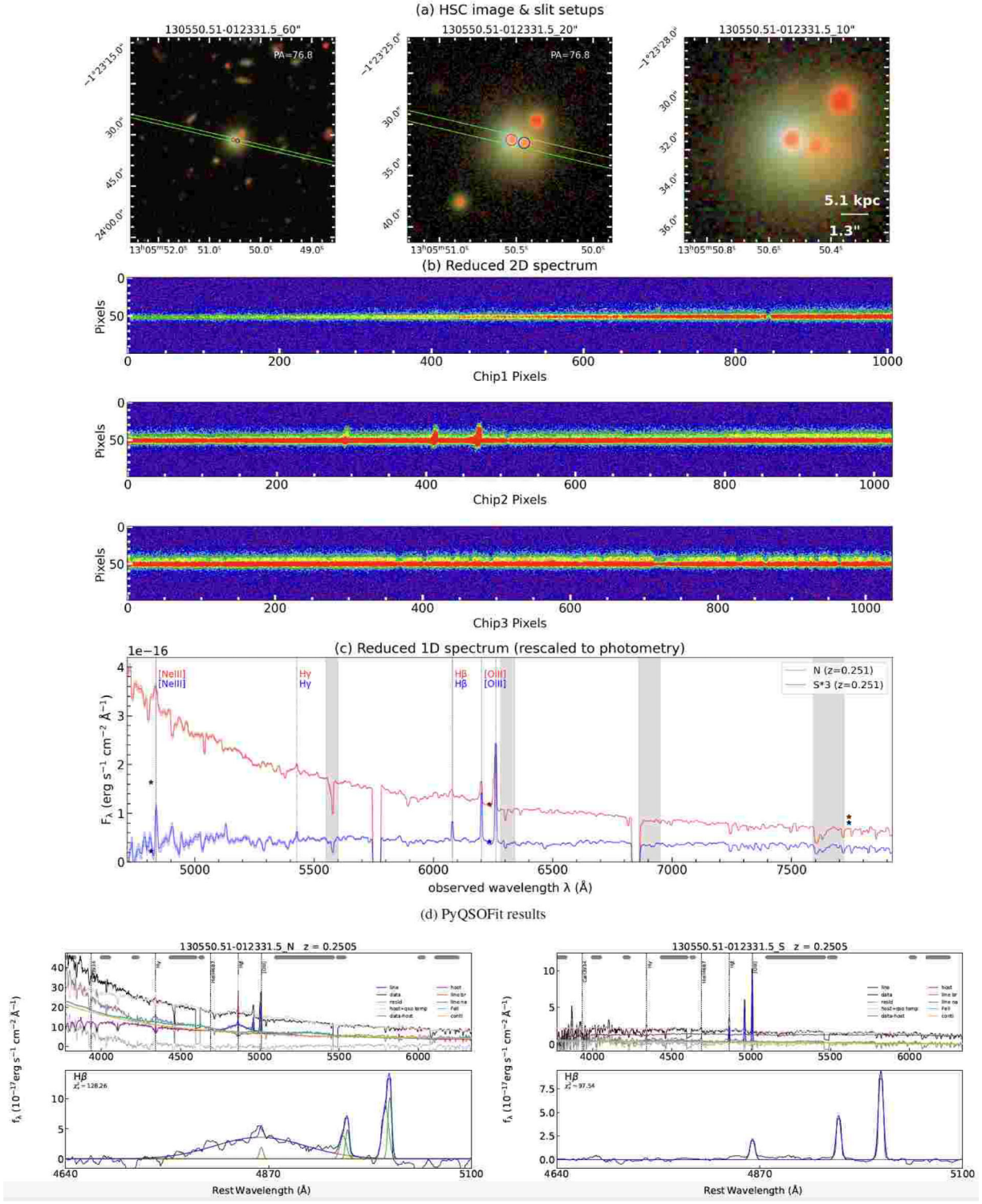

Figure B18. Discovery panel reporting the Gemini/GMOS spectrograph of SDSS J130550.51−012331.5. This system is confirmed as a quasar–SFG pair (Section 4.2.9). The bottom panels show the PyQSOFit results of both the quasar and the companion.

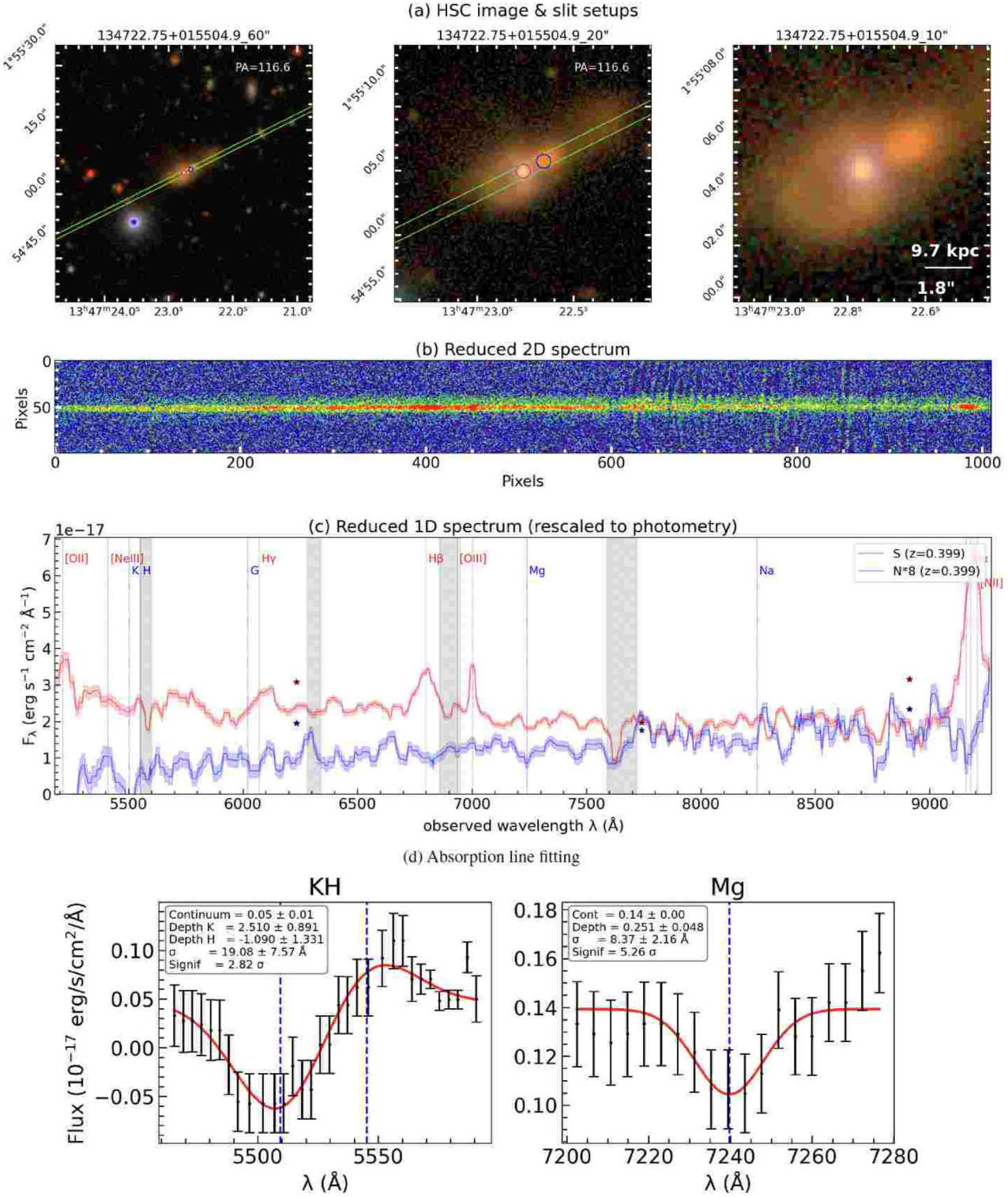

Figure B19. Discovery panel reporting the NTT/EFOSC2 spectrograph of SDSS J134722.75 + 015504.9. This system is considered as a tentative quasar–QG pair (Section 4.2.10), given that the companion spectrum is relatively faint and the absorption lines are not very significant. The bottom panels show the fitting of the Ca H&K and Mg absorption lines of the companion's spectrum.

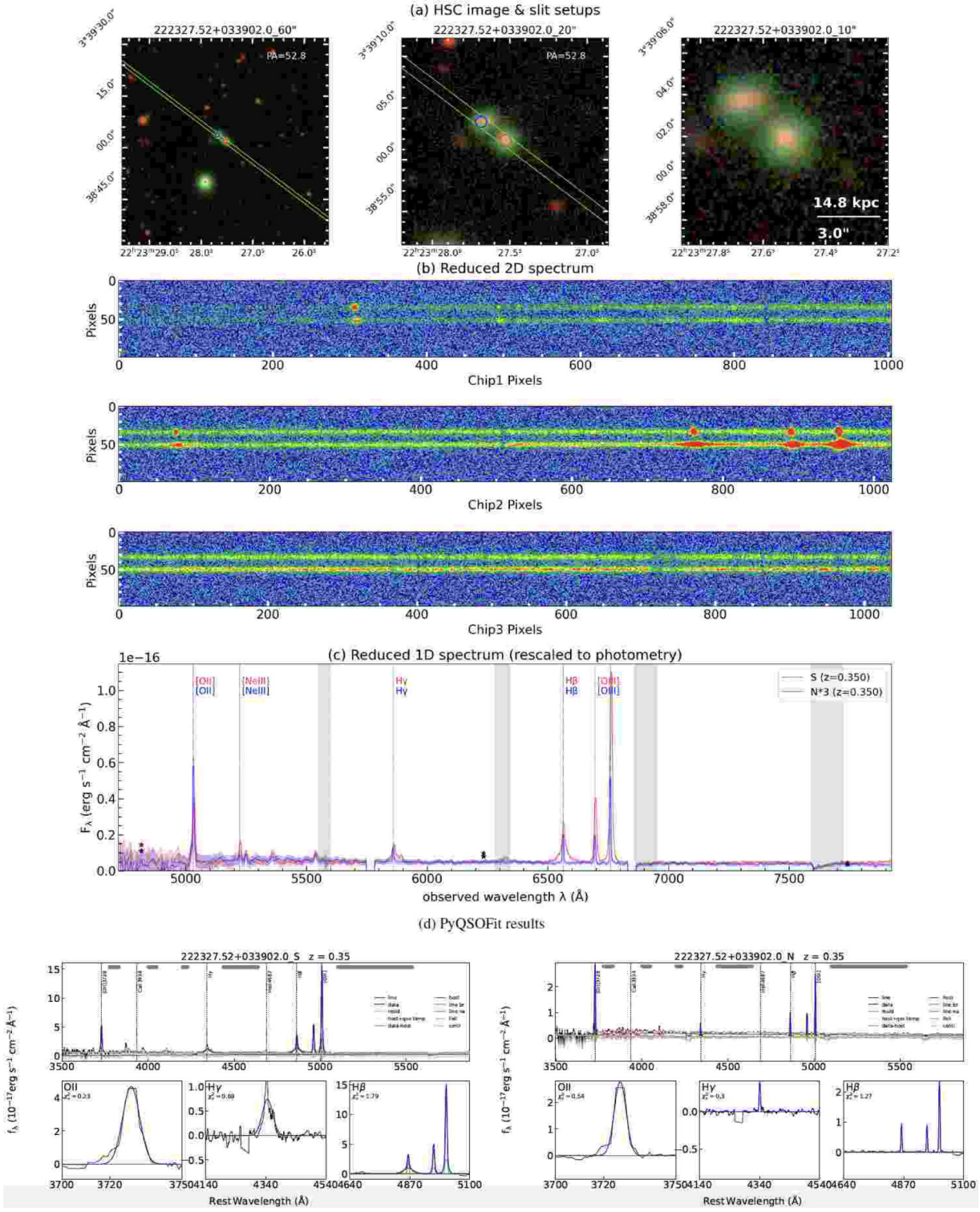

Figure B20. Discovery panel reporting the Gemini/GMOS spectrograph of SDSS J222327.52 + 033902.0. This system is confirmed as a quasar–SFG pair (Section 4.2.11). The bottom panels show the PyQSOFit results of both the quasar and the companion.

This paper has been typeset from a TEX/LATEX file prepared by the author.